Investigations on Crack Behavior in Lamellar and Brick-Mortar Alumina/Epoxy Composites

A Thesis Submitted

In Partial Fulfillment of the Requirements

for the Degree of

DOCTOR OF PHILOSOPHY

by

Sudhendu Nath Tiwari

(2018MEZ0016)



DEPARTMENT OF MECHANICAL ENGINEERING INDIAN INSTITUTE OF TECHNOLOGY ROPAR

June, 2025

Sudhendu Nath Tiwari: Investigations on Crack Behavior in Lamellar and Brick-Mortar Alumina/Epoxy Composites

Copyright © 2025, Indian Institute of Technology Ropar

All Rights Reserved

DEDICATED TO FAMILY AND FRIENDS

Declaration of Originality

I hereby declare that the work which is being presented in the thesis entitled "Investigations on Crack Behavior in Lamellar and Brick-Mortar Alumina/Epoxy Composites" has been solely authored by me. It presents the result of my own independent investigation/research conducted during the time period from January 2019 to June 2025 under the supervision of Prof. Prabhat K. Agnihotri, Professor in the Department of Mechanical Engineering, Indian Institute of Technology Ropar. To the best of my knowledge, it is an original work, both in terms of research content and narrative, and has not been submitted or accepted elsewhere, in part or in full, for the award of any degree, diploma, fellowship, associateship, or similar title of any university or institution. Further, due credit has been attributed to the relevant state-ofthe-art and collaborations (if any) with appropriate citations and acknowledgments, in line with established ethical norms and practices. I also declare that any idea/data/fact/source stated in my thesis has not been fabricated/ falsified/ misrepresented. All the principles of academic honesty and integrity have been followed. I fully understand that if the thesis is found to be unoriginal, fabricated, or plagiarized, the Institute reserves the right to withdraw the thesis from its archive and revoke the associated Degree conferred. Additionally, the Institute also reserves the right to appraise all concerned sections of society of the matter for their information and necessary action (if any). If accepted, I hereby consent to my thesis to be available online in the Institute's Open Access repository, inter-library loan, and the title & abstract to be made available to outside organizations.

Signature Sudhandur

Name: Sudhendu Nath Tiwari

Entry Number: 2018MEZ0016

Program: PhD

Department: Mechanical Engineering

Indian Institute of Technology Ropar

Rupnagar, Punjab 140001

Date: June 24, 2025

ACKNOWLEDGMENTS

At the very outset, I would like to offer my deepest reverence to God for his grace, the opportunities bestowed upon me, and the strength to navigate every challenge. There have been countless helping hands behind the successful completion of my PhD work. First and foremost, I express my heartfelt gratitude to my thesis supervisor **Prof. Prabhat K. Agnihotri**, Professor, Department of Mechanical Engineering, Indian Institute of Technology Ropar, for their invaluable guidance, encouragement, patience, and motivation throughout my research journey. Their insightful feedback and cooperation have been invaluable to my research and the completion of this thesis.

I offer my earnest thankfulness to **Prof. Sarit Kumar Das**, former Director, IIT Ropar and **Prof. Rajiv Ahuja**, Director, IIT Ropar for their strategic oversight and ensuring access to a wide range of facilities and equipment, during my research work at IIT Ropar. I extend my sincere thanks to **Dr. Ekta Singla**, and **Prof. Prabhat K. Agnihotri**, former HOD (Mechanical Engineering), **Prof. Navin Kumar**, HOD (Mechanical Engineering) for their continuous support throughout my PhD work. I am deeply thankful to the members of my dissertation committee, **Dr. Ekta Singla** (Chairperson), **Dr. Ravi Mohan Prasad**, **Dr. Naveen James** and **Dr. Sachin Kumar** for their time, effort, and their valuable suggestions during the semester evaluations. I am profoundly grateful and extend my best regards to all the professors for their pivotal role in establishing my knowledge during my PhD journey.

I sincerely thank my seniors Dr. Harpreet Singh Bedi, Dr. Jasdeep Bhinder, Dr. Viney Ghai, Dr. Ankit Baranawl, Dr. Ankit Chauhan, Dr. Vishal Agrawal, my lab mates Mr. Vinay Kumar, Mr. Shiva Bansal, Mr. Devnarayan Dhiwar, Mr. Prakash Kumar, and my friends Mr. Mainak Pal, Mr. Gopal Chandra Pal, Mr. Raushan Kumar, Dr. Neeraj Yadav, Dr. Anup Pathak as their steadfast support and camaraderie have continuously empowered me throughout this journey.

I am profoundly grateful to all the staff members of the Mechanical Engineering Department, IIT Ropar: Mr. Ram Kumar, Mr. Kaushal Kishor Jha, Mr. Jagmail Singh, Mr. Pankaj, Mr. Sukhwinder Singh, Mr. Hemant, and Mr. Rupinder Singh for helping me out in my research-related work. Further, I am highly indebted to all the staff members of central workshop, IIT Ropar: Mr. Rambir Singh, Mr. Randhir Singh, Mr.

Girdhari Lal, Mr. Yograj, Mr. Rajiv Kumar, Mr. Bhupinder, Mr. Jaskaran and Mr. Jaswinder Singh and wish to express my sincere thanks and regards for their help and support.

My deepest gratitude goes to my family for their constant love and support throughout my life. Thanks to my father **Mr. Surendra Nath Tiwari** and my mother **Mrs. Gayatri Devi** for their boundless love, countless sacrifices, and blessings. No words can fully capture the significance of their steadfast belief in me throughout this journey. I am grateful to my all brothers and sisters, for their constant support and encouragement.

"I wish to extend my heartfelt thanks to my wife, **Shikha Tiwari**, for her unwavering support, patience, and encouragement throughout this journey. Her love and belief in me have been my greatest source of strength, especially during the most challenging moments. Thank you for being my rock and my inspiration."

CERTIFICATE

This is to certify that the thesis entitled "Investigations on Crack Behavior in

Lamellar and Brick-Mortar Alumina/Epoxy Composites" submitted by Sudhendu

Nath Tiwari (2018MEZ0016) for the award of the degree of Doctor of Philosophy of

Indian Institute of Technology Ropar, is a record of bonafide research work carried out

under our guidance and supervision. To the best of my knowledge and belief, the work

presented in this thesis is original and has not been submitted, either in part or full, for

the award of any other degree, diploma, fellowship, associateship, or similar title of any

university or institution.

In our opinion, the thesis has reached the standard fulfilling the requirements of the

regulations relating to the degree.

aber to

Prof. Prabhat K. Agnihotri

Professor, Department of Mechanical Engineering

Indian Institute of Technology Ropar

Rupnagar, Punjab 140001

Date: 24-06-2025

vii

LAY SUMMARY

Materials with high strength and toughness are essential in fields like aerospace, automotive, and protective systems. As a result, extensive efforts have been made to create high-performance, nacre-like materials. Inspired from the outstanding mechanical behavior of the natural nacre, the present study aims to develop stronger and tougher artificial alumina/epoxy composites using freeze casting method. One of the key challenges while fabricating such composites is to control the orientation of the lamellae in the larger domain, which has straight forward application to build nacre-mimetic composites. To address this issue, experiments are performed by incorporating a suitable PDMS wedge in the conventional freeze casting method, known as bi-directional freeze casting.

Extensive experiments are carried out on the fabricated lamellar/brick-mortar alumina/epoxy composites to study the structure – property relationship and deformation characteristics. Although, theses composites are anisotropic, show high strength when loaded along the lamellae direction. The strength decreases for out of plane loading similar to that of conventional fiber composites. The key benefit of fabricating such structures is their exceptional damage tolerance due to rising J_R curve. This characteristic helps us to design structures for various applications, enhancing structural integrity and reliability.

Abstract

Due to the crucial need and importance of materials with high strength and toughness across numerous fields including aerospace, automobile, and protective systems such as sports and military armors, enormous efforts have been made to fabricate nacre-like high performance materials. Nacre (the inner layer of mollusc sea shell) has several structural features at different length scales. At mesoscale, the nacre looks like a structure with interlocked bricks due to the presence of dove-tail kind of features. At microscale, the micron-sized hard bricks are interlayered with few nano-meters thick soft phase to form a brick-mortar type structure. The hard bricks in the nacre have nano-asperities and pillars, that act as a frictional stop. The structural hierarchy present in the nacre generates multiple strengthening and toughening mechanisms that makes it highly strong and tough.

Inspired from the fascinating mechanical behavior of the natural nacre, several attempts have been made in the past to mimic the structural features to develop stronger and tougher artificial materials. But, it is still challenging to surpass the properties of the nacre in the artificial materials. Although, improvements have been made using multitudes of fabrication techniques, the bi-directional freeze casting method emerged as a promising route to fabricate artificial composites that mimics several structural features of the nacre. In the bi-directional freeze casting, the polydimethylsiloxane (PDMS) wedge (low thermal conductivity) placed in between cold copper plate and ceramic suspension plays an important role to modulate the microstructural features such as lamellae thickness and interlamellar spacing and orientation of the microstructure. In this context, there is lack of understanding that how temperature gradients across the suspension depend on the PDMS wedge angles? What will be the freezing front velocity in the bi-directional freeze casting? How temperature gradients and freezing front velocities influence the microstructure of the ceramic scaffold? The freeze casted ceramic scaffolds have directional pores/lamellar channels. Hence, fundamentally it is expected that the lamellar/brick-mortar composites made using ceramic scaffolds as preform, will show anisotropic behavior. Consequently, it becomes essential to determine the anisotropic behavior of such composites. Because the development of tough materials is directly linked to the fracture mechanics aspect, it becomes vital to characterize the crack behavior in newly developed anisotropic lamellar/brick-mortar composites. This work explores the fabrication and characterization of lamellar/brick-mortar composites to address the above-mentioned key issues.

To achieve the objectives, experiments are performed to fabricate nacre-like lamellar alumina/epoxy composites using freeze casting method. A PDMS wedge with varying wedge angles ($\theta = 0^{\circ}$, 5° , 10° , and 20°) is used to modulate the temperature gradients across the ceramic suspension. Consequently, it has been recorded that freezing velocity decreases with the increase in PDMS wedge angles. As a result, both the lamellae thickness and interlamellar spacing increase with the increase in PDMS wedge angle. Moreover, the density of scaffolds also varies along the freezing direction, with comparatively higher density at the bottom location (closer to the cold finger). It is found that the strength of the composites is strongly dependent on alumina lamellae thickness, density of the composites, and loading direction. The quasi-static and high strain rate compression testing reveals the anisotropy in the compressive mechanical properties of alumina/epoxy composites. It is shown that $\theta = 10^{\circ}$ is an optimum PDMS wedge angle to achieve highly aligned lamellar alumina/epoxy composites with higher strength and energy absorbing capacity. To reveals the anisotropic behavior in terms of strength anisotropy, the alumina/epoxy composites fabricated at $\theta = 10^{\circ}$ is subjected to the different direction of loading with respect to the freezing direction. Moreover, the mechanical responses of alumina scaffold and epoxy polymer phase are also recorded for comparison purpose. It is shown that infiltration of epoxy to the lamellar alumina scaffold substantially enhance its compressive strength. To quantify the anisotropic behavior, the calculated strength ratio (R) components suggests that the lamellar composites show strong strength anisotropy at varying strain rates.

To characterize the crack behavior in lamellar anisotropic composites, fracture experiments are performed to measure the J_R curves as a function of lamellae thickness and crack orientation. Experimental results reveal rising J_R curves irrespective of the lamellae thickness and crack orientation angles with higher J_{max} for thicker lamellae, and higher crack orientation angle. Moreover, it is found that the profile of the crack is tortuous, suggesting crack grows under mixed mode conditions. The mode-mixity K_{II}^k/K_I^k at the deflected crack tip is evaluated analytically. To experimentally characterize the anisotropy crack propagation, non-dimensional in parameter $\delta^* = \max\{|\delta^+|, |\delta^-|\}/\min\{|\delta^+|, |\delta^-|\}$ is proposed using crack mouth opening displacement (CMOD) measurements. The variables δ^+ , and δ^- represent CMOD on the either side of the current location of the crack tip. It is shown that δ^* follows the variation of K_{II}^k/K_I^k and thus can be used to predict the degree of mode-mixity during crack propagation in anisotropic lamellar composites. Extended finite element simulations

(XFEM) are carried out to compliment the experimental understanding of crack behaviour in lamellar composites. It is shown that the higher anisotropy makes the crack path more tortuous and thus increases the fracture toughness of lamellar composites having thicker alumina phase or higher crack orientation.

Further, the effect of change in microstructure form lamellar to brick-mortar on the strength and fracture toughness of alumina/epoxy composites is analysed using experiments and an analytical model based on shear lag theory. The experimental results show that both the strength and fracture initiation toughness is comparatively higher for brick-mortar composites in comparison to the lamellar composites. However, the critical toughness J_c is maximum for lamellar composites due to higher crack tortuosity. The shear lag analysis suggests that the relatively shorter bricks carry uniform shear stress in comparison to longer lamellae, and hence shows maximum resistance to fracture initiation (corresponds to maximum elastic strain energy density) for an optimum overlap length. It is envisaged that the findings of the present study will be a significant step towards the development of nacrelike lamellar/brick-mortar composites for structural applications.

Keywords: Alumina/epoxy composites, Bi-directional freeze casting, PDMS wedge angle, nacre-like lamellar/brick-mortar composites, lamellae thickness, J_R curve, Anisotropy, Mode-mixity

LIST OF PUBLICATIONS

• International Journals:

- S.N. Tiwari, P.K. Agnihotri, Effect of freezing conditions on the microstructure and compressive response of alumina/epoxy nacre-type composites, Mater. Today Commun. 37(2023) 107470.
 - https://doi.org/10.1016/j.mtcomm.2023.107470.
- S.N. Tiwari, V. Kumar, P.K. Agnihotri, Anisotropic response of bi-directionally ice-templated alumina/epoxy composites, Int. J. Appl. Ceram. Technol. 22 (2025) 15050. https://doi.org/10.1111/ijac.15050
- 3. **S.N. Tiwari**, P.K. Agnihotri, Characterizing crack behaviour in nacre-like alumina/epoxy lamellar composites: microstructure and crack tortuosity, **Compos. Sci. Technol.** 263 (2025) 111105.
 - https://doi.org/10.1016/j.compscitech.2025.111105

Conference

- 1. **Sudhendu N. Tiwari**, Prabhat K. Agnihotri, "Compressive response of nacre-like micro-layered alumina/epoxy composites" in the 1st **International Conference** on Advancement in Energy (UrjaSangam-2023) held during 18-20 December 2023 at MNNIT, Allahabad, Prayagraj, UP, India.
- Sudhendu N. Tiwari, Prabhat K. Agnihotri, "Anisotropic response of bidirectionally ice-templated Alumina/Epoxy composites" at 4th Global Ceramic Leadership Roundtable, Ceramics for Frontier Sectors: Emerging Advances and Prospects (CerAP2024), March 11-12, 2024, at Center for Space Science and Technology, IIT Roorkee, India.
- Sudhendu N. Tiwari, Prabhat K. Agnihotri, "Estimation of crack resistance curves and crack paths in ceramic-polymer composites with nacre-like lamellar and brickmortar structure" at 8th International Conference on Crack Paths (Rimini – Italy, Online, 10-12 Sept 2024).
- 4. **Sudhendu N. Tiwari**, Prabhat K. Agnihotri, "Crack resistance curves and crack paths in ceramic-polymer composites with nacre-like lamellar and brick-mortar

structure" at International Conference on Frontier in Ceramic Materials (ICFCM 2024), (IIT (BHU) Varanasi, India, 16-18 Dec 2024).

• Publications from Research Work other than Thesis:

1. **S.N. Tiwari**, P.K. Agnihotri, Effect of crumb rubber addition on the deformation and fracture behavior of ductile epoxy matrix. **J. Appl. Polym. Sci.** 140 (2023) 53255.

TABLE OF CONTENTS

DECI	LARATION	iv		
ACK	NOWLEDGEMENT	v		
CERT	FIFICATE	vii		
LAY	SUMMARY	viii		
ABST	TRACT	ix		
LIST	OF PUBLICATIONS	xii		
TABI	LE OF CONTENTS	xiv		
LIST	OF FIGURES	xvii		
LIST OF TABLES		xxii		
ABBREVIATIONS		xxiv		
NOTA	ATIONS	XXV		
CHA	PTER 1: Introduction	1		
1.1	Key issues and proposed solutions	2		
1.2	Literature survey	4		
1.3	Issues to be addressed	5		
1.4	Motivation and objective	6		
1.5	Organization of the Thesis	7		
1.6	References			
CHA	PTER 2: Materials and Methods	15		
2.1	Materials	15		
2.1.1	Alumina powder	15		
2.1.2	Additives	15		
2.1.3	Polymer	16		
2.2	Experimental Methods	16		
2.2.1	Preparation of alumina suspension	16		
2.2.2	Freeze casting apparatus	17		
2.2.3	Bi-directional freeze casting	17		
2.2.4	Processing of lamellar alumina scaffolds	19		
2.2.5	Fabrication of lamellar alumina/epoxy composites	19		

2.2.6	Fabrication of brick-mortar alumina/epoxy composites	20
2.3	Characterization techniques	21
2.3.1	Microstructural characterization	21
2.3.2	Density measurements	22
2.3.3	Mechanical characterization	22
2.3.3.1	Tensile tests	22
2.3.3.2	Quasi-static compression tests	23
2.3.3.3	High strain rate compression tests	23
2.3.3.4	Nano-indentation tests	26
2.3.3.5	Flexural tests	26
2.3.3.6	Fracture toughness tests	26
2.3.4	Finite element simulation	30
2.4	References	31
СНАР	TER 3: Effect of freezing conditions on the microstructure and compres	sive
respon	se of lamellar alumina/epoxy composites	35
3.1	Introduction	35
3.2	Results	37
3.2.1	Effect of PDMS wedge angle on the structural alignment	37
3.2.2	Microstructural characteristics	41
3.2.3	Density of sintered scaffolds and alumina/epoxy (cerepoxy) composites	44
3.2.4	Compressive response of cerepoxy composites at different strain rates	46
3.3	Discussion	52
3.4	Conclusions	54
3.5	References	55
CHAP	TER 4: Characterizing crack behavior in lamellar alumina/ep	oxy
compo	osites: microstructure and crack tortuosity	59
4.1	Introduction	59
4.2	Results	61
4.2.1	Microstructural characteristics	61
4.2.2	Tensile stress - strain curve	63
4.2.3	Nano-indentation result	64

4.2.4	Fracture toughness measurements	64
4.2.4.	Effect of lamellae thickness on J	65
4.2.4.2	2 Effect of crack orientation on J	66
4.2.4.3	3 Toughening mechanisms	67
4.2.4.4	4 Finite element analysis	72
4.3	Discussion	77
4.4	Conclusions	83
4.5	References	84
	PTER 5: Comparison of crack behavior in lamellar and na/epoxy composites Introduction	brick-mortar 89 89
5.2	Results	91
5.2.1	Microstructural features of lamellar and brick-mortar composites	91
5.2.2	Bending stress – strain curve behavior	92
5.2.3	Crack resistance curve behavior	93
5.3	Discussion	94
5.4	Conclusions	100
5.5	References	100
CHAPTER 6: Conclusions and Future Scope 10:		
6.1 Summary of the work		
6.2 Future scopes		

LIST OF FIGURES

1.1	(a) Image of red abalone shell (nacre) [6]. Schematic showing (b)	2	
	brick-mortar structure of the nacre, and (c) aragonite platelets		
	separated by soft organic layer.		
1.2	Processing steps of freeze casting method: preparation of alumina	3	
	suspension, freezing, sublimation, and sintering.		
1.3	Flow chart showing overview of the work done in this thesis.	7	
2.1	SEM micrograph of Al ₂ O ₃ powder (b) particle size distribution of		
	Al ₂ O ₃ powder	15	
2.2	Flow chart for the preparation of alumina suspension.		
2.3	1 1		
	apparatus and (d) data acquisition system and computer.	17	
2.4	Schematic of (a) experimental set-up employed for freeze casting.	18	
	Representation of (b) uni-directional and (c) bi-directional		
	temperature gradients after introducing PDMS wedge over copper		
	wedge attached to the cold Cu plate.		
2.5	Fabricated green samples with different types of PDMS-copper	19	
	wedge molds.		
2.6	Representative optical image of (a) green and (b) sintered sample of	19	
	alumina scaffold.		
2.7	Schematic showing the fabrication step for lamellar alumina/epoxy	20	
	composite.		
2.8	Schematic showing the fabrication steps used for the fabrication of	20	
	brick-mortar alumina/epoxy composite.		
2.9	(a) Sintered sample, representative SEM showing lamellae thickness	21	
	(t), and interlamellar spacing (λ) in sintered samples for 5° wedge		
	angle at (b) top and (c) bottom location.		
2.10	Schematic representing extraction of samples for compression testing	23	
	from the lamellar alumina/epoxy composite.		
2.11	Schematic of the SHPB setup and (b) incident wave pulse with and	24	
	without pulse shaper (c) representative stress-strain and strain rate-		
	strain curves.		

- 2.12 (a) Geometry of SENB sample, (b) SEM of representative SENB 27 sample, (c-d) SEM showing the two phases and (e-f) elemental composition in alumina/epoxy composite.
- 2.13 Schematic representation of SENB samples of lamellar 28 alumina/epoxy composites as a function of (a) wedge angle (θ). (b) crack orientation angle (α). (c) Representative F- ν curve with loading partial unloading cycle.
- **2.14** Schematic of finite element model (t40) with boundary conditions.
- 3.1 (a) *In-situ* temperature measurement during conventional and bidirectional freeze casting. Temperature as a function of time at positions x_1 and x_2 for (b) 0° , (c) 5° (d) 10° , (e) 20° , and (f) horizontal temperature gradient for 0° , 5° , 10° and 20° . Schematic of (g) unidirectional, (h) bi-directional freezing, and evolved representative microstructures for (i) uni-directional (0°), and (j) bi-directional freezing (10°).
- 3.2 Ice front profile in (a) uni-directional (0°), (b) bi-directional freezing (10°). Freezing front velocity obtained from the *in-situ* video recording (c) uni-directional temperature gradient (0°) (d) bi-directional temperature gradient (10°).
- 3.3 SEM micrographs of sintered scaffold as a function of wedge angle (a-a1) 0°-top (a2-a3) 0°-bottom (b-b1) 5°-top (b2-b3) 5°-bottom (c-c1) 10°-top (c2-c3) 10°-bottom (d-d1) 20°-top (d2-d3) 20°-bottom.
- 3.4 (a) Lamellae thickness (t), and (b) interlamellar spacing (λ) as a 44 function of position and wedge angle (θ).
- (a) 0° sintered scaffold (b) optical image showing the evolution of microstructure for 0° sintered scaffold in the freezing direction (c) experimental density of cerepoxy composites.
- 3.6 Compressive stress-strain response of lamellar cerepoxy composites 48 at the strain rate of 0.001 s⁻¹ (a-c) 0° (d-f) 5° (g-i) 10° (j-l) 20°.
- 3.7 (a) Modulus, and (b) strength of cerepoxy composites in x-, y-, andz-directions under quasi-static compression.
- 3.8 Optical images and SEM micrographs of failed sample (a-c) 0° -z (d-f) 0° -y (g-i) 0° -x (j-l) 10° -z (m-o) 10° -y (p-r) 10° -x.

31

- 3.9 (a') Optical image of the cross-sectional view of failed 0° sample 51 loaded in the z-direction. (b'-d') SEM micrographs of damage sites marked in Fig. (a').
- 3.10 Compressive true stress true strain curves of cerepoxy lamellar composites as a function of loading direction at high strain rate (a c) 0° samples (d f) 10° samples.
- 3.11 (a) Strain energy density of lamellar cerepoxy composites at 0.001 s⁻ 54 and >1000 s⁻¹, and (b) Comparison between lamellae thickness and strength (quasi-static) as a function of PDMS wedge angle.
- **4.1** Schematic of CMOD measurement in layered alumina/epoxy **61** composite during fracture tests.
- 4.2 (a) Schematic showing the bi-directional freeze casting method to fabricate lamellar alumina scaffold. (b) SEM image of alumina scaffold. (b-1) Schematic showing lamellae thickness (t), and interlamellar spacing (λ). (c) Variation of t, and λ as a function of PDMS wedge angle (θ). (d) SEM image of alumina/epoxy composite.
- 4.3 Micro X-ray computed tomographs (μ XCT) of alumina scaffold 63 fabricated with 10° PDMS wedge angle (a) 3-D image of the sample (16 × 12 × 6 mm³) and the corresponding 2-D images in (b) *x-y* plane (c) *x-z* plane (d) *y-z* plane.
- **4.4** (a) Tensile stress strain curve of (a) lamellar alumina/epoxy **63** composite, and (b) neat epoxy.
- **4.5** Indentation load displacement curves for neat epoxy.
- **4.6** F-v curves for (a) θ_0 (b) θ_5 (c) θ_1 0 and (d) θ_2 0 lamellar **66** alumina/epoxy composite samples from SENB testing. (e) $J \Delta a$ curves of lamellar alumina/epoxy composites fabricated with varying PDMS wedge angles (θ).
- 4.7 F-v curves of composite samples having crack orientation of (a) $\alpha 0$ 67 (b) $\alpha 30$ and (c) $\alpha 70$ in SENB fracture tests. (d) J Δa curves as a function of α .
- 4.8 SEM of untested θ_0 SENB sample. (b) Fractured SENB sample, 68 showing tortuous crack paths (b1) left fractured surface, and (b2) right fractured Surface (c-d) magnified view of left and right

64

- fractured surfaces near the crack tip respectively.
- 4.9 (a) SEM of untested θ_10 SENB sample (b) Fractured SENB sample,
 69 showing tortuous crack paths (b1) left fractured surface, and (b2) right fractured Surface (c-d) magnified view of left and right fractured surfaces near the crack tip respectively.
- 4.10 (a) SEM of untested θ_5 SENB sample (b) Fractured SENB sample, 70 showing tortuous crack paths (b1) left fractured surface, and (b2) right fractured Surface (c-d) magnified view of left and right fractured surfaces near the crack tip respectively.
- 4.11 (a) SEM of untested θ_20 SENB sample (b) Fractured SENB sample, 70 showing tortuous crack paths (b1) left fractured surface, and (b2) right fractured Surface (c-d) magnified view of left and right fractured surfaces near the crack tip respectively.
- 4.12 (a, e) SEM of untested α0 and α30 and (b, f) respective fractured 71 SENB sample, (b1, f1) left fractured surface, and (b2, f2) right fractured Surface (c1-c3 and d1-d3, g1-g3 and h1-h3) magnified view of left and right fractured surfaces near the crack tip for 0° and 30° crack oriented SENB sample respectively.
- 4.13 (a) SEM of untested α70 SENB sample (b) fractured SENB sample,
 (b1) left fractured surface, and (b2) right fractured Surface (c1-c3 and d1-d3) magnified view of left and right fractured surfaces near the crack tip respectively.
- 4.14 (a) Computational F v curves for varying lamellae thickness and maximum principal stress contour for (b) t20 (c) t40 (d) t80 numerical model.
- 4.15 (a) Computational F v curves for varying lamellae thickness at a constant alumina volume fraction of 50%. (b-e) shows the corresponding maximum principal stress contour and crack path. Crack tortuosity from these simulations is compared in (f).
- **4.16** (a) Comparison of experimental and computational F v curves for varying crack orientations. Maximum principal stress contours and crack path including kink angle (β) for (b-c) α 0 (d-e) α 30 (f-g) α 90.

- **4.17** (a) Optical images of SENB sample showing crack growth and (b) 77 evolution of CMOD (δ^- and δ^+) at the crack mouth with time (\hat{t}) in θ_- 10 sample during SENB test.
- **4.18** CMOD measurement as δ^- and δ^+ at the crack mouth with time for (a) **78** θ 0, (b) θ 5, (c) θ 20.
- **4.19** CMOD measurement as δ^- and δ^+ at the crack mouth with time for (a) **79** $\alpha 0$, (b) $\alpha 30$, (c) $\alpha 70$, and (d) $\alpha 90$.
- 4.20 (a) Mode mixity (K_{II}^k/K_I^k) as a function of wedge angle, (a-1) SEM image showing kink angle (β) for θ₀ sample as representative. (b) crack anisotropy (δ*- t̂) as a function of wedge angle. (c) Mode mixity (K_{II}^k/K_I^k), and (d) crack anisotropy (δ*- t̂) as a function of crack orientation angle.
- **4.21** Crack tortuosity as a function of (a) wedge angle and (b) crack orientation in lamellar composites.
- 5.1 (a a1) SEM micrographs of lamellar alumina/epoxy composites (b 91b1) SEM micrographs of brick-mortar alumina/epoxy composite.
- 5.2 (a) Representative SEM micrograph of 1450-BMC showing the definition of microstructural features (b) average thickness of alumina phase (t) and epoxy phase (λ) in lamellar and brick-mortar composites.
- 5.3 (a) Bending stress strain curves of lamellar and brick-mortar93 composites. (b) The ultimate flexure strength of 1450-L, 1450-BMC, and 1600-BMC composite samples.
- 5.4 (a) Typical *F-v* curves of lamellar and brick-mortar SENB composite 94 samples. (a-1) SEM of representative SENB sample (b) *J* Δa curve of 1450-L, 1450-BMC, and 1600-BMC composite samples, indicating validity of the data points following the ASTM standards [40].
- 5.5 Comparison of (a) crack initiation toughness (K_{IC}) (b) fracture 95 toughness (J_c) for 1450-L, 1450-BMC, and 1600-BMC composites.
 SEM of Fractured SENB specimens showing crack path in (c) lamellar, and (d) brick-mortar composites.

- 5.6 (a) Schematic representing the structure of brick-mortar composites 97 (b) 2D unit cell used for continuum analysis, and (c) two bricks connected with polymer phase with overlap length L_0 .
- 5.7 Distribution of normalised (a) axial tensile stress (b) shear stress as a 98 function of overlap length under linear elastic condition.
- 5.8 Schematic of the crack path in (a) brick-mortar (b) lamellar 99 composites (c d) SEM micrograph showing fractured surface of brick-mortar composite.

LIST OF TABLES

2.1	Wave speed and transit time for 0° and 10° samples for different	
	direction of loading	
2.2	Material parameters used in the numerical simulations of the	30
	alumina/epoxy lamellar composites.	
3.1	Average temperature at locations x_1 , x_2 , and horizontal temperature	41
	gradient.	
3.2	Density of sintered alumina scaffolds and cerepoxy composites.	45
3.3	Theoretical density of cerepoxy composites.	46
3.4	Experimental density of cerepoxy composites.	46
4.1	Mode I stress intensity factors (K_I) of different types of samples.	78
5.1	Comparison of mechanical properties of lamellar/brick-mortar	100
	composites with the data in other literatures.	

ABBREVIATIONS

PDMS Polydimethylsiloxane

Cerepoxy alumina/epoxy

VARTM vacuum-assisted resin transfer molding

SEM Scanning electron microscopy
SHPB Split Hopkinson Pressure Bar

CMOD Crack mouth opening displacement

XFEM Extended finite element method

μ**XCT** Micro X-ray computed tomographs

SENB Single edge notched beam

TSLs Traction-separation constitutive laws

MAXPS Maximum principal stress criteria

NOTATIONS

a	Crack length	$v_{\rm z}$	Freezing velocity
C	Wave velocity	V	Volume fraction
C_{T}	Crack tortuosity	α	Crack orientation angle
E	Young's modulus	β	kink angle of the crack
G	Modulus of rigidity	δ^*	Non-dimensional parameter
J	J integral	based	l on CMOD
$K_{\rm I}$	Mode I stress intensity factor	θ	Wedge angle
$K_{\rm II}$	Mode II stress intensity factor	ho	Density
L	Length of the lamellae/brick	ϕ	Porosity
L_0	Overlap length	λ of epo	Interlamellar spacing/thickness oxy phase
$r_{ m p}$	Plastic zone size	ε	Strain
R	Strength ratio	Ė	Strain rate
t	Lamellae thickness	σ	Stress
T	Temperature	τ	Shear stress
î	time	γ	Shear strain
U_{ϵ}	Strain energy density		
$v_{\rm s}$	Striker velocity		

CHAPTER 1: Introduction

Design and fabrication of advanced materials with high strength and toughness are desirable in many applications such as load-bearing structures, space, automobiles, and protective systems [1–3]. However, the design and fabricating a structure with improved strength and toughness simultaneously is a challenging problem. As the key two structural properties *i.e.*, strength and toughness, tend to be mutually exclusive, the strong materials are typically brittle, while tough materials are often weak [4]. Interestingly, natural composites such as nacreous part of the sea shell, and bones have simultaneous superior strength and toughness [1–3,5,6], that make them truly damage-tolerant structures [7–9]. Although, these natural composites are comprised of weak constituents (hard minerals and soft polymer) in terms of their mechanical properties, the resulting structures show significantly better properties that is beyond the predictions of rule of mixtures [1]. Such outstanding potential is realised due to their hierarchical structure over multiple length scales. Essentially, nacre is a kind of layered composites that consists of 95 vol% hexagonal aragonite platelets (0.2-0.5 µm thick with approximate diameter of 5-8 μm), bonded by a thin layer of viscoelastic polymer (10 -50 nm) as shown in the Fig. 1.1 (a – c). Such nacreous structures show more than 1000 times higher fracture toughness than its major constituent aragonite [1,5]. In case of natural nacre, various investigations have been done in to reveals its structure-properties relation [2–5]. The hard phase (aragonite) in nacre provides strength, while the soft phase (organic phase) accommodate inelastic/viscoelastic deformation, thereby conferring toughness [1-3]. These investigations reveal various toughening mechanisms i.e. crack deflections at the interface, crack arresting within the thin organic layer, frictional sliding between the mineral platelets, mineral bridges, platelet interlocking due to dove-tail feature, plastic deformation of soft polymer, crack tortuosity, and platelet pull-out [1,2]. As a result, toughening in the nacre shows rising R-curve behavior [1–5].

Based on these insights, efforts have been made to fabricate nacre-like materials using varying synthesis routes in literature [10]. The basic idea is to fabricate a scaffold of hard phase (ceramic) and then impregnate it with softer material (epoxy, Polydimethylsiloxane (PDMS) etc.) to manufacture layered composite having alternating hard and soft layers [11–20]. The scaffold is filled with sacrificial material and then pressed to convert the lamellas into bricks. The brick structured scaffold is then impregnated with softer material to obtain

nacre-like brick mortar structure [11,12]. Even though the resulting microstructure look like brick-mortar, the resulting material does not show the desired combination of strength and toughness. It is primarily attributed to lack of multiple length scale, relatively higher volume fraction of softer phase and some other structural features that are difficult to achieve in artificial nacre. Therefore, designing suitable processing routes and understanding the mechanics of crack propagation in layered anisotropic materials is the primary aim of this thesis.

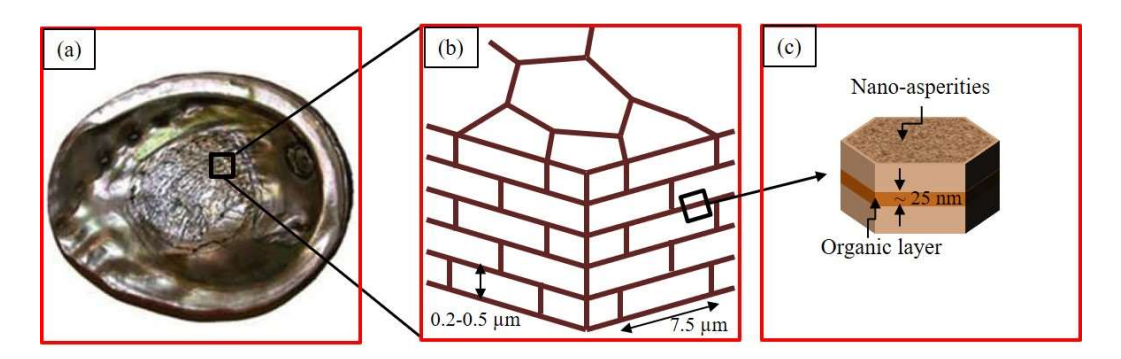


Fig. 1.1 (a) Image of red abalone shell (nacre) [6]. Schematic showing (b) brick-mortar structure of the nacre, and (c) aragonite platelets separated by soft organic layer.

1.1 Key issues and proposed solutions

The fabrication of nacre-like architecture is key to simultaneously realize the high strength and toughness in artificial composites. However, it depends on our ability to mimic microstructure of nacre in artificial man-made materials. It is challenging to control various features such as well-arranged brick/mortar structure, brick thickness and spacing, and other structural features present at the micro- and nano scale regimes in artificial nacre. The presence of such complex features in the nacre induces various toughening mechanisms, which results in very high toughness amplification than its major constituents [1-3,6,21]. So, incorporating some or all such toughening mechanisms of the nacre in artificial composites becomes essential for the similar kind of toughness amplification. Several attempts have been made in the past using varying synthesis techniques to fabricate nacrelike artificial structures [10]. The layer-by-layer assembly and vacuum assisted filtration methods yield lamellar composite films only [22,23]. Magnetically assisted slip casting and freeze casting methods are used to fabricate macroscale hierarchical structures [11,12,14,24,25]. The later approach is advantageous due to its simplicity, control of processing parameters, environment friendliness, and more importantly to mimic several structural features akin to the structure of nacre at multiple length scale [17,26,27].

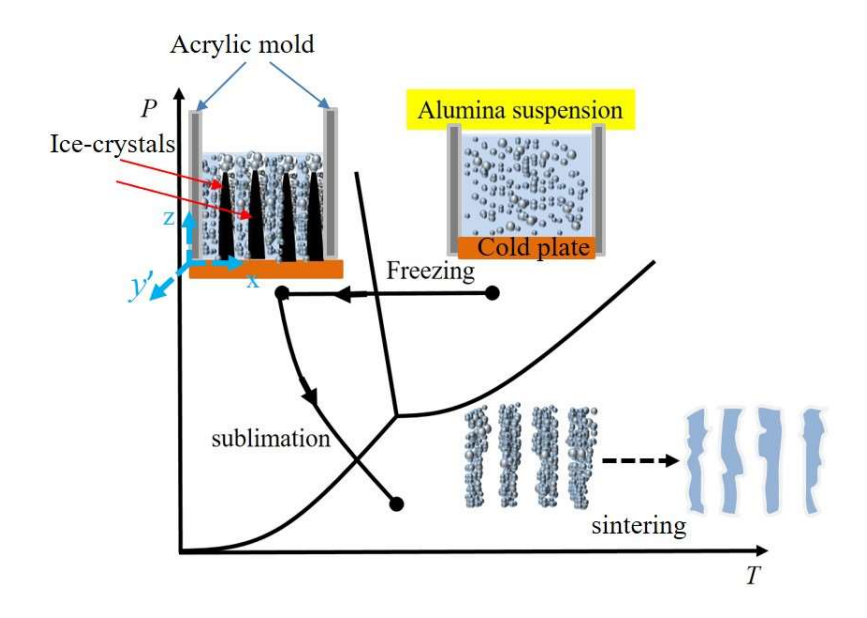


Fig. 1.2 Processing steps of freeze casting method: preparation of alumina suspension, freezing, sublimation, and sintering.

The freeze casting technique (also known as ice-templating) has four processing steps namely preparation of ceramic suspension, freezing of suspension, sublimation of solvent phase, and sintering of the green body as shown in Fig. 1.2. The structure obtained after the freeze casting process is porous, lamellar, and with lamellar channels between the ceramic walls. Particularly, when directional freeze casting (uni-directional freeze casting) is performed using a temperature gradient, lamellar macroporous structures are obtained whose several structural features resembles with the nacre at multiple length scale [11,12]. However, the microstructures obtained from uni-directional freeze casting method, differ from the long-range aligned structures found in the natural nacre [28]. Only lamellar macroporous structure in multiple domain with short-range alignment of ceramic walls can be obtained using uni-directional freeze casting. Since then attempts have been made to control the orientation of the ice crystal during freezing process. Particularly, a method of patterned cold finger [12], and freezing under flow [29] have been successfully applied to control the orientations of the ice crystals, but it resulted in a limited extent of alignment in the order of few 'mm' only. H. Bai et al. [30] first reported the use of additional temperature gradient along the cold surface in uni-directional freezing process. This is achieved by incorporating a PDMS (polydimethylsiloxane) wedge between the cold surface and ceramic suspension. A PDMS wedge between the cold surface and ceramic suspension induces two

temperature gradients across the suspension. Due to low thermal conductivity of the PDMS wedge, nucleation of ice crystals starts at the thinnest part of the PDMS wedge and grow preferentially in both the horizontal as well as vertical directions under the influence of dual temperature gradients. This results in the freezing of solvent in long-range lamellar pattern and yields long-range lamellar structure up to the cm scale [28,30,31]. Thus, bi-directional freeze casting is preferred to fabricate lamellar ceramic scaffolds in this work. Some key articles showing the progress in fabrication and mechanics of lamellar and nacre type materials are summarized in the next section. The more detailed survey of literature is included in respective Chapters of the thesis.

1.2 Literature survey

As mentioned earlier, nacre-inspired artificial composites have been fabricated with lamellar and brick-mortar type composite structures [11,12,25,32]. Due to their microstructure, the structural response of such composites is anisotropic [30,33]. It has been found that the strength of the nacre-like artificial composites is higher along the ceramic walls and decreases when the load is applied perpendicular to the ceramic walls [33]. Munch et al. [11] was the first to fabricate high performance alumina/PMMA lamellar and brick-mortar composites with fracture toughness (J_c) of up to 8 kJ-m⁻² and strength in the range of 200 MPa. They also reported that lamellar and brick-mortar structure with strong interface have higher strength as well as toughness. A similar processing strategy using bidirectional freezing method is applied to reproduce brick-mortar composites for different ceramic and polymer phase, reaching maximum strength and toughness (work of fracture) of ~100 MPa, 2 kJ-m⁻² respectively for hydroxyapatite/PMMA [25], ~175 MPa, 1 - 2 kJm⁻² respectively for zirconia/ dental resin [32]. The fabrication of nacre-like brick-mortar composites using different processing strategies and materials combination is reported in [10,17]. Depending upon the processing strategies, materials combinations, and range of control over the microstructure, the strength and toughness of brick-mortar structure ranges from 20 - 660 MPa, and 3 - 17 MPa-m^{0.5} respectively [17]. Grossman et al. [16] have fabricated a brick-mortar structure incorporated with mineral bridges at the nano-scale and a relatively complaint layer at the meso scale. This study reveals that deformation energy dissipated in the compliant layer must be higher than the elastic energy stored in nacre-like layer for the higher toughness. Recently, it has been also investigated that nacre-like hierarchical composites can be effectively toughened through the design of polymer phase

that is more capable of dissipating energy through the formation of plastic zone ahead of the crack tip [34].

In addition to the experimental observations, many models based on the representative volume element (RVE) have been developed to investigate the mechanical performance of the natural nacre [35–40]. These models utilise the periodic unit cell to investigate the role of overlap length between the bricks [37,38], dove-tail angle of the bricks [39], aspect ratio of the bricks [40], and failure sequences on the strength, stiffness, and toughness of the composites [35]. Based on these studies several conclusions have been drawn related to the desirable microstructure for optimum strength and toughness. F. Barthelat study [38] reveals that the brick-mortar microstructure is only advantageous for high volume fraction of bricks content, and the strength of brick should be at least 5 times than the strength of interfaces. A 2D tension-shear-chain (TSC) model developed by Yi Yan et al. [41] reveals that symmetrically staggered nacreous structure is the best to supress the adverse effect of microstructural randomness. However, non-linear shear lag analysis on nacreous structure reveals that under certain combination of elastic-plastic properties and sizes, brick-mortar structure may become insensitive to the distribution of overlapping length [37]. The above models assume perfect unit cell which is far different from the real microstructure. The discrete element method (DEM) accounts the random variation of brick sizes, which explains the discrepancy observed in the toughness values of brick-mortar structure obtained assuming perfect unit cell model [42]. Apart from RVE analysis, few numerical simulations are also performed to characterize the crack behaviour (crack propagation and onset of crack deflection) in nacre-like alumina composites [43,44]. Vilchez et al. [43] developed a mixed mode fracture model to quantify the local toughness at the deflected crack tip in nacre-like alumina composites. Recently, a phase-field fracture model is proposed to understand the influence of oblique angle i.e. the angle between loading and platelet directions, on the strength and fracture behaviour of nacre-type composites [45].

1.3 Issues to be addressed

The literature survey shows that processing routes have been and are being developed to fabricate nacre-like lamellar and brick-mortar structures [10,28]. Moreover, the reported studies reveal various strengthening mechanisms in nacre like materials. The crack behaviour seems to be very complex in these materials. A combination of multiple toughening mechanism improves the fracture toughness in these composites. However, apart from other issues, two major points that are of particular interest are (i) the long-range

aligned lamellar structure using bi-directional freeze casting in the literatures is still limited up to cm scale only, and (ii) how to characterize the mode mixity during crack propagation in lamellar anisotropic materials.

Thus, there is need to determine suitable freezing conditions as well as processing parameters in bi-directional freeze casting method to obtain long-range order in lamellar composites. Moreover, the lamellar composites show anisotropy in the mechanical properties. Therefore, it is necessary to establish structure – property relationship as a function of microstructure. In addition, cracks do not grow in self-similar manner due to the structure as well as material anisotropy in lamellar composites. Thus, there is a need to develop tools to characterize the crack behaviour and mode mixity at the onset of crack initiation and crack propagation in lamellar and nacre type composites. Addressing some of these challenges is the primary contribution of the present thesis.

1.4 Motivation and objective

Even though the bi-directional freeze casting technique is used to obtain nacre-like microstructure, there is a lack of understanding of how process parameters like temperature gradients, and freezing front velocity influence the microstructure of porous scaffolds. What is the anisotropy present in the composites which is made by infiltrating polymer phase into the freeze casted ceramic scaffold? Due to the presence of material as well as structural anisotropy, what will be the crack behavior in fabricated composites? What are the underlying mechanisms that drives the crack initiation and propagation? Establishing a method using fracture mechanics approach to quantify the mode-mixity at the crack tip as a function of structural/material anisotropy in nacre-like layered/brick-mortar composites becomes important. Based on these insights, the objective of the present thesis are as follows:

- 1. To determine the optimum wedge angle in bi-directional freeze casting to fabricate highly aligned lamellar alumina scaffold.
- 2. To understand structure-property relation of lamellar alumina/epoxy composites under compressive loading at various strain rates.
- 3. Characterization of crack behavior in lamellar alumina/epoxy composites using experiment/ XFEM approach.
- 4. Comparison of crack behavior in lamellar and brick-mortar alumina/epoxy composites.

1.5 Organization of the thesis

Fig. 1.3 shows the step-wise work performed in this thesis with the help of flow chart. The research work performed in the present thesis is organized into seven Chapters. A chapterwise breakup of the proposed thesis work is as follows:

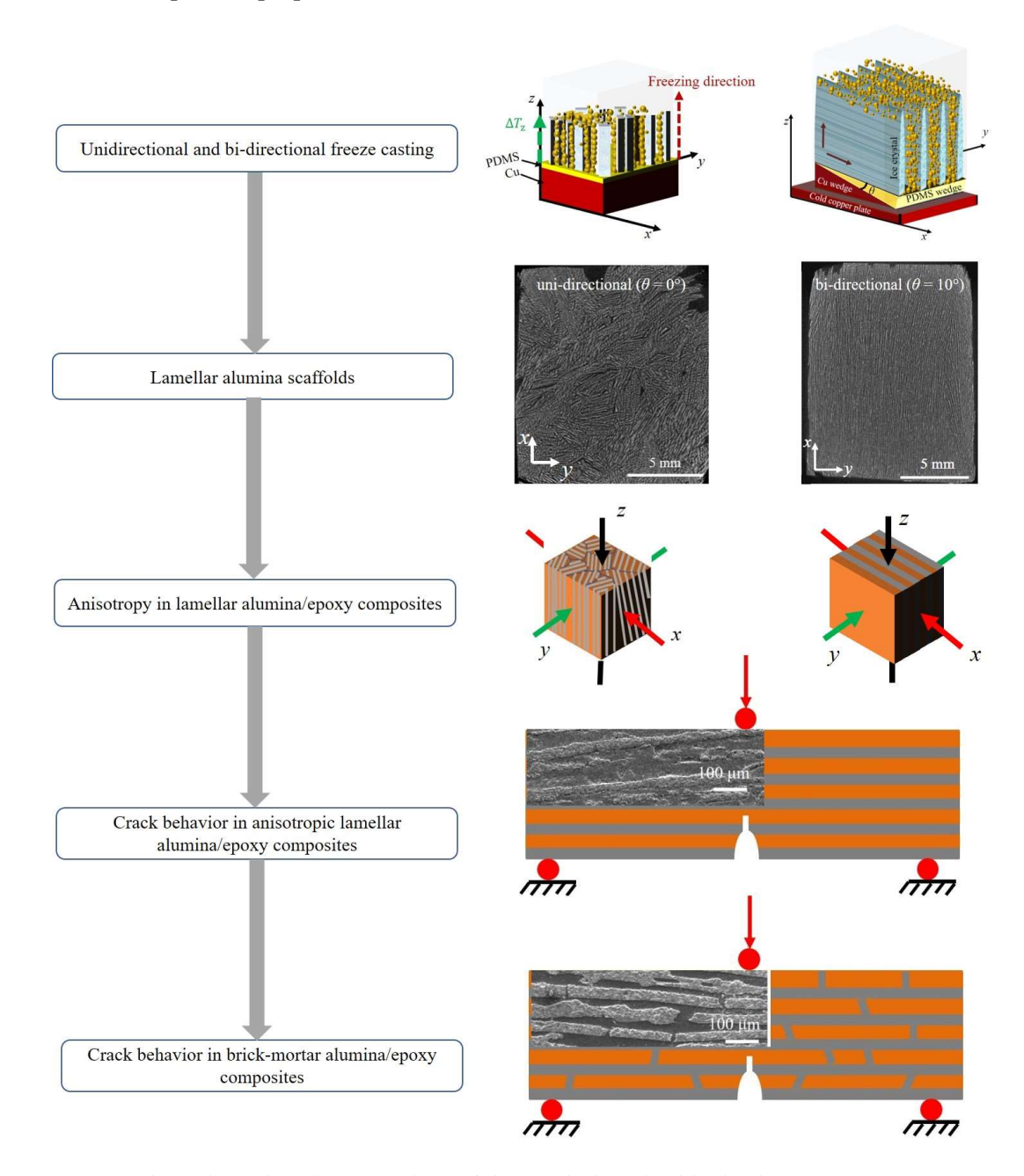


Fig. 1.3 Flow chart showing overview of the work done in this thesis.

Chapter 1 Introduction

Chapter 1 introduces the field of nacre-inspired artificial composites, its fabrication strategies, and structure-mechanical properties relationship. Subsequently, the structure-property relation of nacreous part of the sea shell is discussed which often display unique combination of strength and toughness simultaneously. It is still challenging to mimic exactly the structure of nacre artificially. Therefore, the progress towards the development of nacre-like structure and its mechanical properties are explored next. Out of several fabrication strategies, it is found that freeze casting method is the best technique to mimic the structural features of nacre. However, this method still lacks to produce long-range aligned structure akin to the structure of nacre. This sets the motive and objectives of the present study to design and fabricate the nacre-like structures with improved mechanical properties.

Chapter 2 Materials and methods

Chapter 2 includes the materials utilized, fabrication methods, and characterization techniques used in the present study.

Chapter 3 Effect of freezing conditions on the microstructure and compressive response of lamellar alumina/epoxy composites

This Chapter discusses how a low thermal conductive PDMS wedge between the copper wedge and alumina suspension modifies the freezing conditions from uni-directional to bi-directional across the alumina suspension. Consequently, it influences the microstructure of the lamellar alumina scaffolds. The mechanical behavior of lamellar alumina/epoxy composites is investigated through compression testing along different orientations relative to the freezing direction at various strain rates.

Chapter 4 Characterizing crack behavior in lamellar alumina/epoxy composites: microstructure and crack tortuosity

Chapter 4 investigates the crack behavior in lamellar alumina/epoxy composites as a function of lamellae thickness and crack orientation. The experimental fracture analysis is supplemented by XFEM models and supported through analytical crack formulation models. An experimentally tractable parameter is proposed to quantify the mode mixity during crack growth in lamellar composites.

Chapter 5 Comparison of crack behavior in lamellar and brick-mortar alumina/epoxy composites

Chapter 5 explores the comparison of crack behavior in lamellar/brick-mortar alumina/epoxy composites. The lamellar alumina scaffolds manufactured in *Chapters 3*, and 4 are infiltrated with sacrificial wax, followed by uniaxial pressing at 40 MPa, and 80 °C to get brick-like alumina scaffolds. After re-sintering of brick-like alumina scaffolds, epoxy is infiltrated to get brick-mortar alumina/epoxy composites. Both flexure and fracture tests are performed to evaluate the strength and fracture toughness of the lamellar/brick-mortar alumina/epoxy composites. Based on the microstructural features (*i.e.* lamellae thickness, polymer thickness, and brick overlap length) in lamellar/brick-mortar composites, an analytical model using shear lag theory is put forward to complement the experimental findings in this Chapter.

Chapter 6 Conclusions and future scope

The research findings of the present study are comprehensively outlined in this Chapter. Potential future directions for this research are also explored.

1.6 References

- [1] U.G.K. Wegst, H. Bai, E. Saiz, A.P. Tomsia, R.O. Ritchie, Bioinspired structural materials, Nat. Mater. 14 (2015) 23–36. https://doi.org/10.1038/nmat4089.
- [2] M.A. Meyers, P.Y. Chen, A.Y.M. Lin, Y. Seki, Biological materials: Structure and mechanical properties, Prog. Mater. Sci. 53 (2008) 1–206. https://doi.org/10.1016/j.pmatsci.2007.05.002.
- [3] A.R. Studart, Towards high-performance bioinspired composites, Adv. Mater. 24 (2012) 5024–5044. https://doi.org/10.1002/adma.201201471.
- [4] R.O. Ritchie, The conflicts between strength and toughness, Nat. Mater. 10 (2011) 817–822. https://doi.org/10.1038/nmat3115.
- [5] F. Barthelat, H.D. Espinosa, An experimental investigation of deformation and fracture of nacre-mother of pearl, Exp. Mech. 47 (2007) 311–324. https://doi.org/10.1007/s11340-007-9040-1.
- [6] H.D. Espinosa, J.E. Rim, F. Barthelat, M.J. Buehler, Merger of structure and material in nacre and bone - Perspectives on de novo biomimetic materials, Prog. Mater. Sci. 54 (2009) 1059–1100. https://doi.org/10.1016/j.pmatsci.2009.05.001.
- [7] H. Gao, B. Ji, I.L. Jäger, E. Arzt, P. Fratzl, Materials become insensitive to flaws at nanoscale: Lessons from nature, Proc. Natl. Acad. Sci. U. S. A. 100 (2003) 5597–5600. https://doi.org/10.1073/pnas.0631609100.
- [8] P. Fratzl, R. Weinkamer, Nature's hierarchical materials, Prog. Mater. Sci. 52 (2007)

- 1263–1334. https://doi.org/10.1016/j.pmatsci.2007.06.001.
- [9] R.O. Ritchie, In pursuit of damage tolerance in engineering and biological materials, MRS Bull. 39 (2014) 880–890. https://doi.org/10.1557/mrs.2014.197.
- [10] I. Corni, T.J. Harvey, J.A. Wharton, K.R. Stokes, F.C. Walsh, R.J.K. Wood, A review of experimental techniques to produce a nacre-like structure, Bioinspiration and Biomimetics 7 (2012). https://doi.org/10.1088/1748-3182/7/3/031001.
- [11] E. Munch, M.E. Launey, D.H. Alsem, E. Saiz, A.P. Tomsia, R.O. Ritchie, Tough, bio-inspired hybrid materials, Science (80-.). 322 (2008) 1516–1520. https://doi.org/10.1126/science.1164865.
- [12] M.E. Launey, E. Munch, D.H. Alsem, H.B. Barth, E. Saiz, A.P. Tomsia, R.O. Ritchie, Designing highly toughened hybrid composites through nature-inspired hierarchical complexity, Acta Mater. 57 (2009) 2919–2932. https://doi.org/10.1016/j.actamat.2009.03.003.
- [13] P. Podsiadlo, A.K. Kaushik, E.M. Arruda, A.M. Waas, B.S. Shim, J. Xu, H. Nandivada, B.G. Pumplin, J. Lahann, A. Ramamoorthy, N.A. Kotov, Ultrastrong and stiff layered polymer nanocomposites, Science (80-.). 318 (2007) 80–83. https://doi.org/10.1126/science.1143176.
- [14] S. Askarinejad, N. Rahbar, Mechanics of bioinspired lamellar structured ceramic/polymer composites: Experiments and models, Int. J. Plast. 107 (2018) 122–149. https://doi.org/10.1016/j.ijplas.2018.04.001.
- [15] T.P. Niebel, F. Bouville, D. Kokkinis, A.R. Studart, Role of the polymer phase in the mechanics of nacre-like composites, J. Mech. Phys. Solids 96 (2016) 133–146. https://doi.org/10.1016/j.jmps.2016.06.011.
- [16] M. Grossman, F. Bouville, F. Erni, K. Masania, R. Libanori, A.R. Studart, Mineral Nano-Interconnectivity Stiffens and Toughens Nacre-like Composite Materials, Adv. Mater. 29 (2017). https://doi.org/10.1002/adma.201605039.
- [17] F. Bouville, Strong and tough nacre-like aluminas: Process-structure-performance relationships and position within the nacre-inspired composite landscape, J. Mater. Res. 35 (2020) 1076–1094. https://doi.org/10.1557/jmr.2019.418.
- [18] J. Liu, R. Bai, Z. Lei, C. Xu, Q. Ye, W. Martens, P.K. Yarlagadda, C. Yan, Experimental and numerical investigation of the toughening mechanisms in bioinspired composites prepared by freeze casting, Compos. Sci. Technol. 182 (2019) 107768. https://doi.org/10.1016/j.compscitech.2019.107768.
- [19] Y. Wang, Q. Liu, Z.F. Lan, B. Zhang, H.Q. Zhang, J.W. Liu, F. Ye, Strong and tough

- bioinspired nacre-like B4C/Al functionally graded materials with eliminated abrupt interfaces, Compos. Commun. 25 (2021) 100741. https://doi.org/10.1016/j.coco.2021.100741.
- [20] E. Poloni, F. Bouville, C.H. Dreimol, T.P. Niebel, T. Weber, A.R. Biedermann, A.M. Hirt, A.R. Studart, Tough metal-ceramic composites with multifunctional nacre-like architecture, Sci. Rep. 11 (2021) 1–12. https://doi.org/10.1038/s41598-021-81068-z.
- [21] F. Barthelat, R. Rabiei, Toughness amplification in natural composites, J. Mech. Phys. Solids 59 (2011) 829–840. https://doi.org/10.1016/j.jmps.2011.01.001.
- [22] J.J. Richardson, M. Björnmalm, F. Caruso, Technology-driven layer-by-layer assembly of nanofilms, Science (80-.). 348 (2015). https://doi.org/10.1126/science.aaa2491.
- [23] Z. Xu, J. Bykova, M. Baniasadi, S. Moreno, Z. Zhou, N. Das, S. Bandi, Y. Xi, D. Qian, R.H. Baughman, M. Minary-Jolandan, Bioinspired Multifunctional Ceramic Platelet-Reinforced Piezoelectric Polymer Composite, Adv. Eng. Mater. 19 (2017) 1–10. https://doi.org/10.1002/adem.201600570.
- [24] H. Le Ferrand, F. Bouville, T.P. Niebel, A.R. Studart, Magnetically assisted slip casting of bioinspired heterogeneous composites, Nat. Mater. 14 (2015) 1172–1179. https://doi.org/10.1038/nmat4419.
- [25] H. Bai, F. Walsh, B. Gludovatz, B. Delattre, C. Huang, Y. Chen, A.P. Tomsia, R.O. Ritchie, Bioinspired Hydroxyapatite/Poly(methyl methacrylate) Composite with a Nacre-Mimetic Architecture by a Bidirectional Freezing Method, Adv. Mater. 28 (2016) 50–56. https://doi.org/10.1002/ADMA.201504313.
- [26] S. Deville, E. Saiz, R.K. Nalla, A.P. Tomsia, Freezing as a path to build complex composites, Science (80-.). 311 (2006) 515–518. https://doi.org/10.1126/science.1120937.
- [27] S. Deville, E. Saiz, A.P. Tomsia, Ice-templated porous alumina structures, Acta Mater. 55 (2007) 1965–1974. https://doi.org/10.1016/j.actamat.2006.11.003.
- [28] W. Gao, M. Wang, H. Bai, A review of multifunctional nacre-mimetic materials based on bidirectional freeze casting, J. Mech. Behav. Biomed. Mater. 109 (2020) 103820. https://doi.org/10.1016/j.jmbbm.2020.103820.
- [29] F. Bouville, E. Portuguez, Y. Chang, G.L. Messing, A.J. Stevenson, E. Maire, L. Courtois, S. Deville, Templated grain growth in macroporous materials, J. Am. Ceram. Soc. 97 (2014) 1736–1742. https://doi.org/10.1111/jace.12976.
- [30] H. Bai, Y. Chen, B. Delattre, A.P. Tomsia, R.O. Ritchie, Bioinspired large-scale

- aligned porous materials assembled with dual temperature gradients, Sci. Adv. 1 (2015) 1–9. https://doi.org/10.1126/sciadv.1500849.
- [31] S. Algharaibeh, A.J. Ireland, B. Su, Bi-directional freeze casting of porous alumina ceramics: A study of the effects of different processing parameters on microstructure, J. Eur. Ceram. Soc. 39 (2019) 514–521. https://doi.org/10.1016/j.jeurceramsoc.2018.09.030.
- [32] G. Tan, J. Zhang, L. Zheng, D. Jiao, Z. Liu, Z. Zhang, R.O. Ritchie, Nature-Inspired Nacre-Like Composites Combining Human Tooth-Matching Elasticity and Hardness with Exceptional Damage Tolerance, Adv. Mater. 31 (2019) 1–9. https://doi.org/10.1002/adma.201904603.
- [33] S. Akurati, J. Marin, B. Gundrati, D. Ghosh, Assessing the role of loading direction on the uniaxial compressive response of multilayered ice-templated alumina-epoxy composites, Materialia 14 (2020) 100895. https://doi.org/10.1016/j.mtla.2020.100895.
- [34] T. Magrini, A. Senol, R. Style, F. Bouville, A.R. Studart, Fracture of hierarchical multi-layered bioinspired composites, J. Mech. Phys. Solids 159 (2022). https://doi.org/10.1016/j.jmps.2021.104750.
- [35] M.R. Begley, N.R. Philips, B.G. Compton, D. V. Wilbrink, R.O. Ritchie, M. Utz, Micromechanical models to guide the development of synthetic "brick and mortar" composites, J. Mech. Phys. Solids 60 (2012) 1545–1560. https://doi.org/10.1016/j.jmps.2012.03.002.
- [36] F. Barthelat, M. Mirkhalaf, The quest for stiff, strong and tough hybrid materials: An exhaustive exploration, J. R. Soc. Interface 10 (2013). https://doi.org/10.1098/rsif.2013.0711.
- [37] Y. Ni, Z. Song, H. Jiang, S.H. Yu, L. He, Optimization design of strong and tough nacreous nanocomposites through tuning characteristic lengths, J. Mech. Phys. Solids 81 (2015) 41–57. https://doi.org/10.1016/j.jmps.2015.04.013.
- [38] F. Barthelat, Designing nacre-like materials for simultaneous stiffness, strength and toughness: Optimum materials, composition, microstructure and size, J. Mech. Phys. Solids 73 (2014) 22–37. https://doi.org/10.1016/j.jmps.2014.08.008.
- [39] A. Ghazlan, T.D. Ngo, P. Tran, Influence of interfacial geometry on the energy absorption capacity and load sharing mechanisms of nacreous composite shells, Compos. Struct. 132 (2015) 299–309. https://doi.org/10.1016/j.compstruct.2015.05.045.

- [40] J.E. Rim, P. Zavattieri, A. Juster, H.D. Espinosa, Dimensional analysis and parametric studies for designing artificial nacre, J. Mech. Behav. Biomed. Mater. 4 (2011) 190–211. https://doi.org/10.1016/j.jmbbm.2010.11.006.
- [41] Y. Yan, Z.L. Zhao, X.Q. Feng, H. Gao, Nacre's brick—mortar structure suppresses the adverse effect of microstructural randomness, J. Mech. Phys. Solids 159 (2022) 104769. https://doi.org/10.1016/j.jmps.2021.104769.
- [42] N. Abid, M. Mirkhalaf, F. Barthelat, Discrete-element modeling of nacre-like materials: Effects of random microstructures on strain localization and mechanical performance, J. Mech. Phys. Solids 112 (2018) 385–402. https://doi.org/10.1016/j.jmps.2017.11.003.
- [43] V. Vilchez, P.I.B.G.B. Pelissari, V.C. Pandolfelli, F. Bouville, Mixed-mode fracture model to quantify local toughness in nacre-like alumina, J. Eur. Ceram. Soc. 43 (2023) 4472–4481. https://doi.org/10.1016/j.jeurceramsoc.2023.03.044.
- [44] T. Duminy, R. Henry, J. Adrien, A. Doitrand, T. Duminy, R. Henry, J. Adrien, A. Doitrand, S.M. Anisotropic, Anisotropic fracture in nacre-like alumina To cite this version: HAL Id: hal-03885621, (2023).
- [45] K. Kang, Y. Chen, J. Hou, Y. Liu, Fracture behaviors of nacre-like composites via phase-field fracture modeling, Eng. Fract. Mech. 296 (2024) 109837. https://doi.org/10.1016/j.engfracmech.2023.109837.

CHAPTER 2: Materials and Methods

This Chapter provides the details of materials, fabrication strategies and characterization tools used to understand the structure – property relationships in lamellar and brick-mortar alumina/epoxy composites.

2.1 Materials

2.1.1 Alumina powder

The micrograph of alumina (Al_2O_3) powder (density, 3.96 g-cm⁻³) (CT3000SG, Almatis GmbH, Germany) used in this study is shown in Fig. 2.1 (a). Dynamic light scattering (DLS) technique is used to find the average particle size of the alumina powder. Fig. 2.1 (b) shows the particle size distribution with an average particle size of 0.5 μ m.

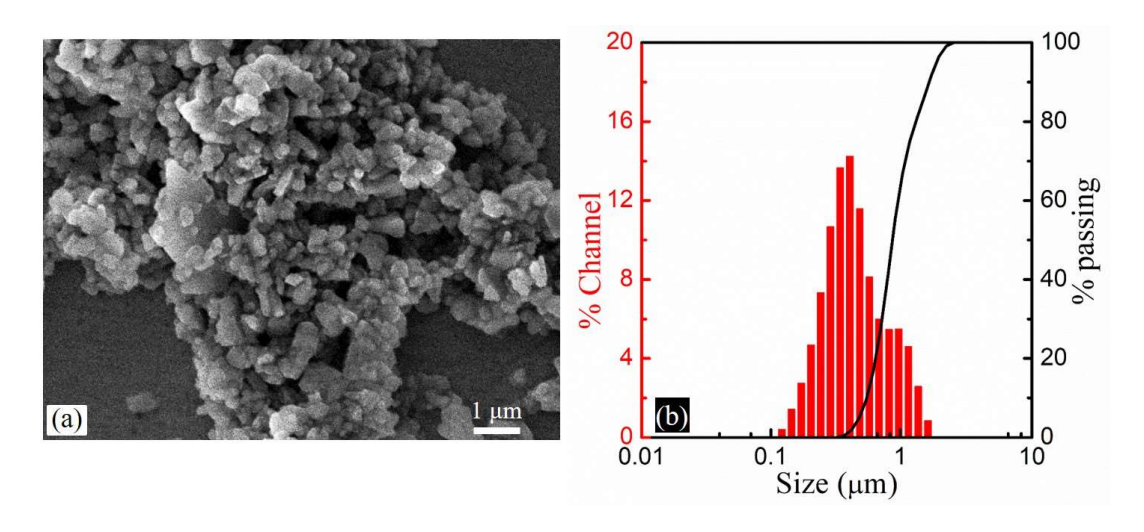


Fig. 2.1 (a) SEM micrograph of Al₂O₃ powder (b) particle size distribution of Al₂O₃ powder.

2.1.2 Additives

Dolapix CE64 (Zschimmer & Schwarz) is used as dispersant for making Al₂O₃ suspension. This dispersant is an anionic surfactant with an average molecular weight of 320 g/mol. Poly vinyl alcohol (PVA) is used as a binder to increase the green strength of the alumina scaffolds, it helps to shape ice crystals into a lamellar microstructure [1]. A de-bubblizer agent (1-Octanol, Sigma-Aldrich) is also used to prevent the formation of air bubbles within the alumina suspension.

2.1.3 Polymer

Trans ER-099 epoxy (Bisphenol-A type, epoxy equivalent weight: 182 - 192 g Eq.⁻¹) and trans EH-150 (modified cycloaliphatic, accelerated polyamine, 91 - 96 g Eq.⁻¹) hardener are used as a secondary phase in the lamellar and brick-mortar alumina/epoxy composites.

2.2 Experimental Methods

2.2.1 Preparation of alumina suspension

The alumina suspension is prepared at 20 vol% of alumina powder in deionized (DI) water with sintering additives Titania (NRL India, 1 wt% of alumina powder, 30-50 nm), dispersant Dolapix CE64 (Zschimmer & Schwarz, 0.6 wt% of alumina powder), and an organic binder (polyvinyl alcohol, 2 wt% of alumina powder). The organic binder (PVA)

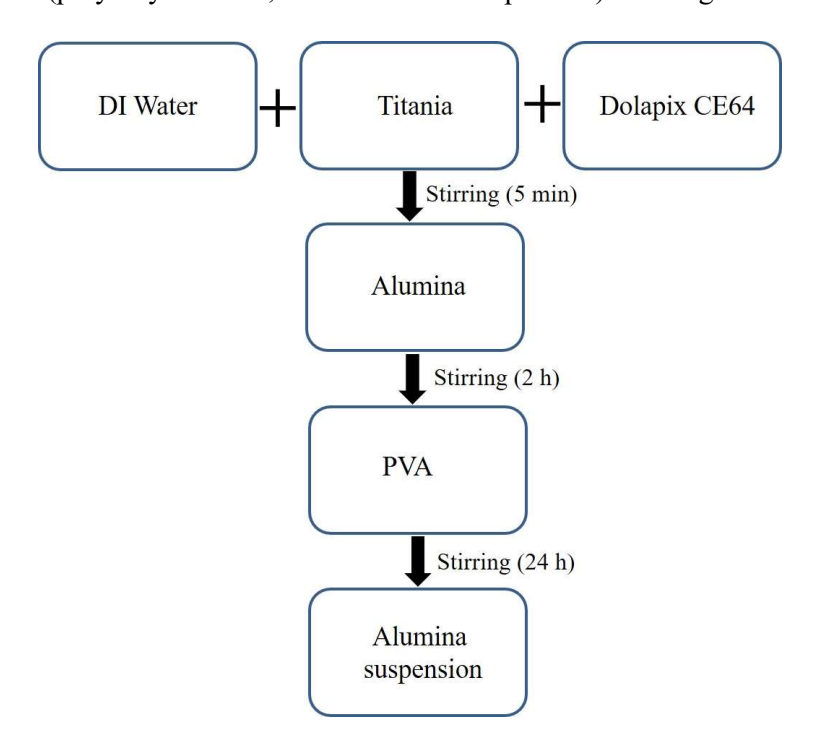


Fig. 2.2 Flow chart for the preparation of alumina suspension.

increases the viscosity of the slurry [2]. This slows down the gravitational sedimentation of heavier alumina particles during the casting process. The dispersant improves particle dispersion by providing electrostatic or steric stabilization, which prevents particle agglomeration and helps to maintain a homogeneous suspension over time [3]. The flow chart shown in Fig. 2.2 illustrates the processing steps of making alumina suspension. The mixture of DI water, titania, and dolapix Ce64 is magnetically stirred for 5 min before adding alumina powder. After 2 h of magnetic stirring, an organic binder polyvinyl alcohol (Sigma-Aldrich, 2 wt% of alumina powder) is added and the slurry is stirred again for 24 h

at 600 rpm to obtain a well-dispersed alumina colloidal solution. A de-bubblizer agent 1-octanol (Sigma-Aldrich, 0.1 vol% of alumina powder) is added to the colloidal solution to remove the air bubbles.

2.2.2 Freeze casting apparatus

The *in-house* developed freeze casting setup used in this study is shown in Fig. 2.3. The liquid nitrogen source shown in Fig. 2.3 (a) is connected to the freezing apparatus (Fig. 2.3 (c)) to maintain a constant sub-zero temperature of the cold copper plate. For bi-directional freeze casting, a mold with a copper/PDMS wedge system [4], as shown in Fig. 2.3 (b), containing the ceramic slurry is placed on the cold copper plate. A temperature data logger (20-channel multiplexer, Keysight) integrated with a computer as shown in Fig. 2.3 (d) is used to record the temperature history across the PDMS surface-slurry interface with K-type thermocouples during the freezing process.

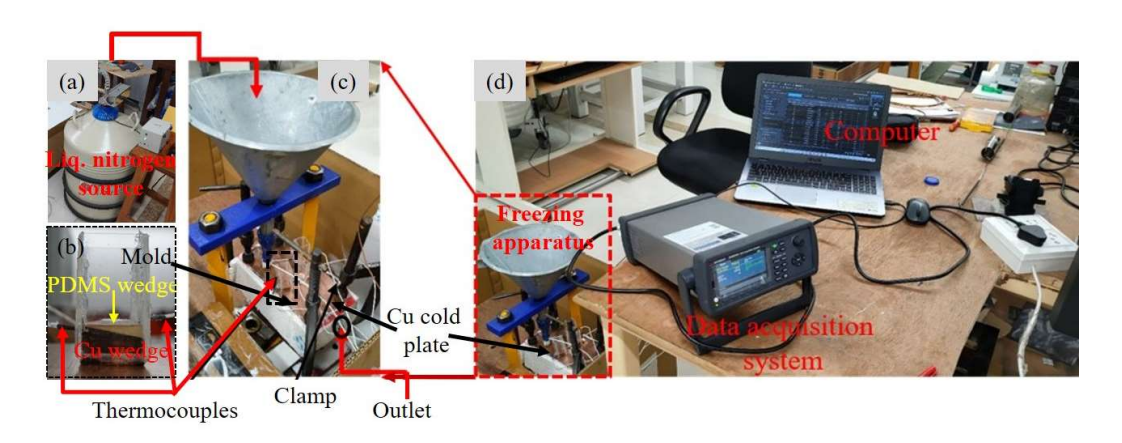


Fig. 2.3 (a) Liquid nitrogen (b) copper/PDMS wedge mold (c) freezing apparatus and (d) data acquisition system and computer.

2.2.3 Bi-directional freeze casting

The alumina slurry is poured into square cross-section mold (20 mm \times 20 mm, 40 mm height) with different PDMS wedge angles (θ) to start the freezing process. To prepare the molds, copper blocks of the size 20 mm \times 20 mm \times 10 mm are used to make wedges with 0°, 5°, 10°, and 20° wedge angles as shown in the Fig. 2.4 (b - c). Here, 0° stands for a flat 1 mm thick PDMS sheet on the top of the copper plate. The schematic of the freezing setup used for ice-templating is shown in Fig. 2.4 (a). In this setup, the temperature of the cold finger (copper cold plate) is maintained by controlling the flow of liquid nitrogen. The freezing of slurry is carried out under constant temperature boundary conditions i.e. mold

filled with slurry is placed over the cold copper plate after it attains a constant temperature of -30 ± 2 °C, while the top of the mold is exposed to the atmospheric conditions (25 °C). The view of bottom portion of the mold placed over cold copper plate of 0° and θ copper/PDMS wedge is shown in Fig. 2.4 (b) and 2.4 (c) respectively. During the freezing process, slurry in 0° PDMS mold will experience a vertical temperature gradient (ΔT_z) only (Fig. 2.4 (b)), and hence nucleation and growth of ice crystals occur preferentially in the zdirection. In the case of molds with non-zero wedge (θ) , ice crystals grow under the influence of dual temperature gradients ΔT_z and ΔT_x (see Fig. 2.4 (c)). It is to be noted here that due to non-zero ΔT_x , ΔT_z will be varying along the x-axis of the mold. Moreover, ΔT_x across the PDMS wedge will increase with the increasing θ . Therefore, a temperature data logger (20-channel multiplexer, Keysight) is integrated with a computer system to record temperature measurements across the PDMS surface-slurry interface (see mold filled with slurry connected with thermocouples in Fig. 2.4 (a)) with K-type thermocouples during the freezing process. In addition, video of the freezing process is recorded (Sony dsc-rx10m4) to analyse the nature of the freezing front and to determine the freezing front velocities in uni-directional (0 $^{\circ}$) and bi-directional freezing (10 $^{\circ}$) cases. The temperature measurements across the PDMS surface-slurry interface, nature of freezing front, and freezing velocities are presented in Section 3.2.1 of Chapter 3.

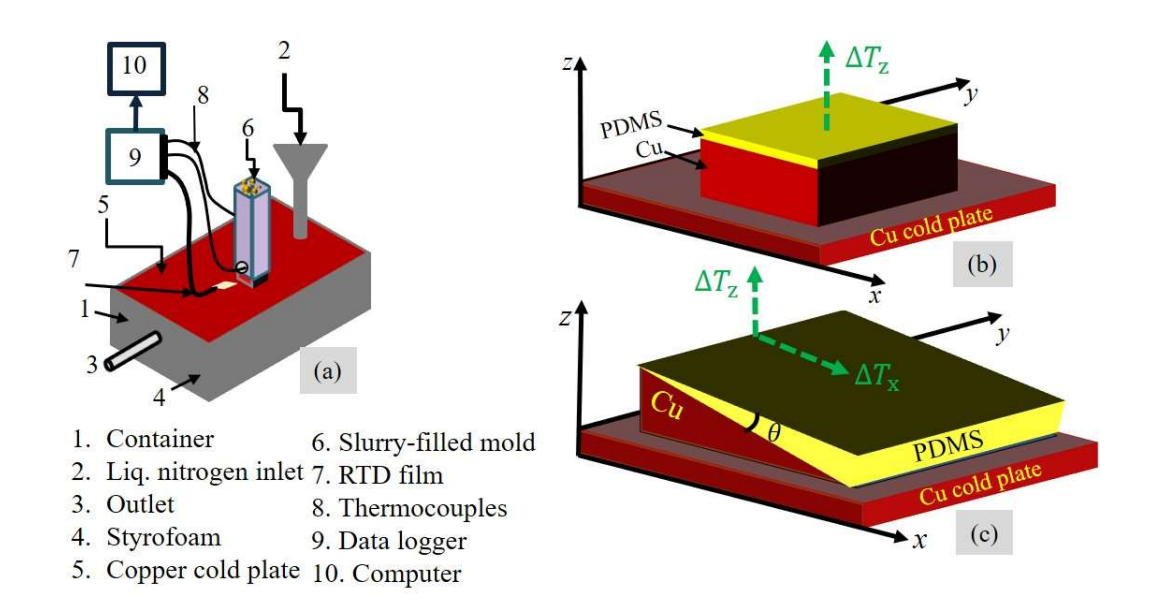


Fig. 2.4 Schematic of (a) experimental set-up employed for freeze casting. Representation of (b) uni-directional and (c) bi-directional temperature gradients after introducing PDMS wedge over copper wedge attached to the cold Cu plate.

2.2.4 Processing of lamellar alumina scaffolds

The frozen samples are freeze-dried for more than 36 h at -55 °C and 0.01 mbar pressure inside a freeze dryer (Alpha 1-2 LDplus, Martin Christ, Germany) to remove the ice phase. The freeze-dried green samples have dimensions of 20 mm \times 20 mm \times 35 mm as shown in Fig. 2.5. These samples are sintered with two temperature cycles. In the first cycle, samples are heated up to 450 °C for 2 h at the heating rate of 2 °C/min to remove the organic binder and additives. The second cycle (10 °C/min up to 1450 °C for 2 h) increases the density and strength of green samples. The sintered samples show a linear shrinkage of approximately 10 % across the width and height of the sample as shown in Fig. 2.6.

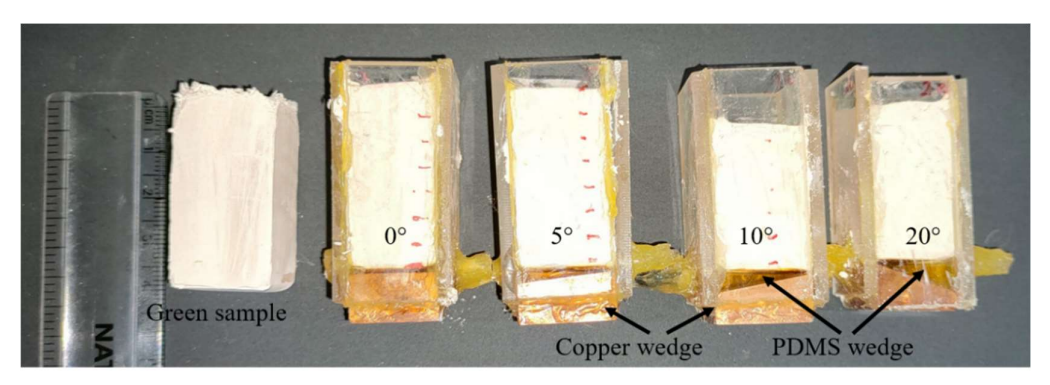


Fig. 2.5 Fabricated green samples with different types of PDMS-copper wedge molds.

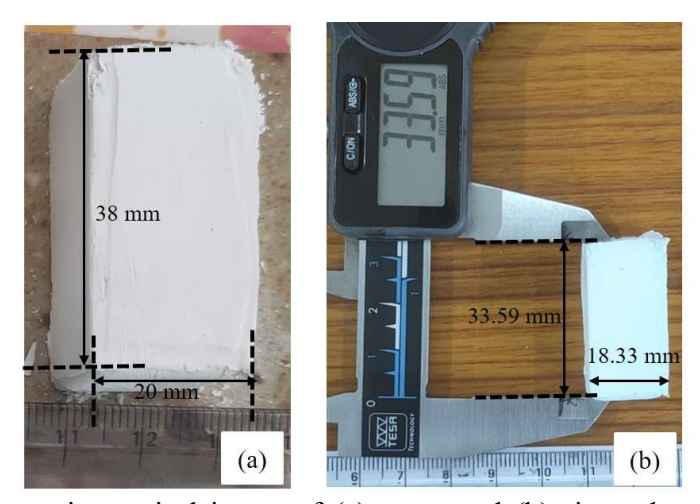


Fig. 2.6 Representative optical image of (a) green and (b) sintered sample of alumina scaffold.

2.2.5 Fabrication of lamellar alumina/epoxy composites

The sintered lamellar alumina scaffolds fabricated as a function of PDMS wedge angles are infiltrated with epoxy resin using the VARTM process at the vacuum pressure of 0.1 MPa to fabricate lamellar alumina/epoxy (cerepoxy) composites as shown in the Fig. 2.7. Trans

ER-099 epoxy (Bisphenol-A type, epoxy equivalent weight from 182-192 g Eq.⁻¹) and trans EH-150 (modified cycloaliphatic, accelerated polyamine, 91-96 g Eq.⁻¹) hardener procured from TCPL, India are used in the stoichiometric composition of 2:1. The infiltrated scaffolds are cured at room temperature for 24 h followed by the post-curing at 80 °C for 4 h.

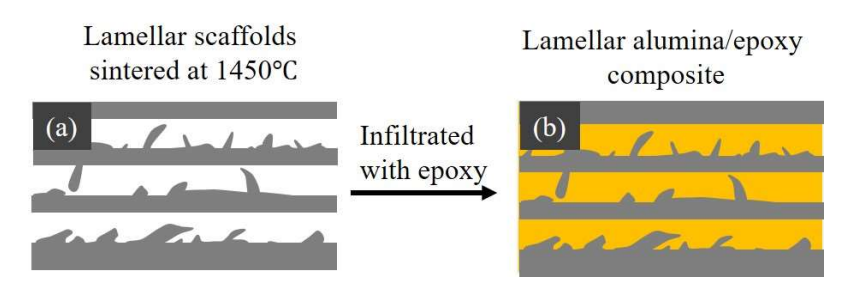


Fig. 2.7 Schematic showing the fabrication step for lamellar alumina/epoxy composite.

2.2.6 Fabrication of brick-mortar alumina/epoxy composites

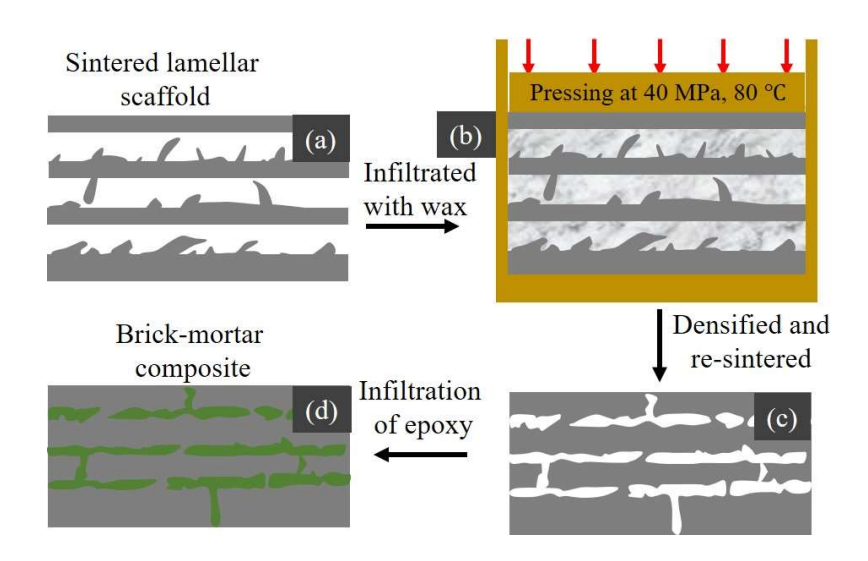


Fig. 2.8 Schematic showing the fabrication steps used for the fabrication of brick-mortar alumina/epoxy composite.

To convert the long lamellar ceramic walls into smaller bricks, lamellar alumina scaffolds are infiltrated with wax and then pressed under the pressure of 40 MPa at 80 °C (above the melting point of wax) as shown in the Fig. 2.8 (a-b). The melted wax during pressing provides dual function *i.e.* it promotes the densifications of the scaffold and helps to hold the bricks together after cooling. The densified scaffolds are fired at 500°C for 2 hr to burn out the residual wax, and then re-sintered at two different temperatures separately i.e.

1450°C and 1600°C to make two different kinds of brick-like alumina scaffolds (Fig. 2.8 (c)). The nacre-mimetic composites with brick-mortar structures are fabricated by infiltrating the brick-like alumina scaffolds with epoxy (Fig. 2.8 (d)). Depending upon the sintering temperature and the structure of the scaffolds, the sample nomenclatures are taken as 1450-L, 1450-BMC, and 1600-BMC for lamellar and brick-mortar composites. All types of fabricated composites are post-cured at 80°C for 4 h before testing.

2.3 Characterization techniques

2.3.1 Microstructural characterization

The microstructural characterization of lamellar alumina scaffolds, lamellar alumina/epoxy composites, and brick-mortar alumina/epoxy composites is performed on SEM (**JEOL 6610 LV, Japan**), and FESEM (**JSM-7610FPlus**).

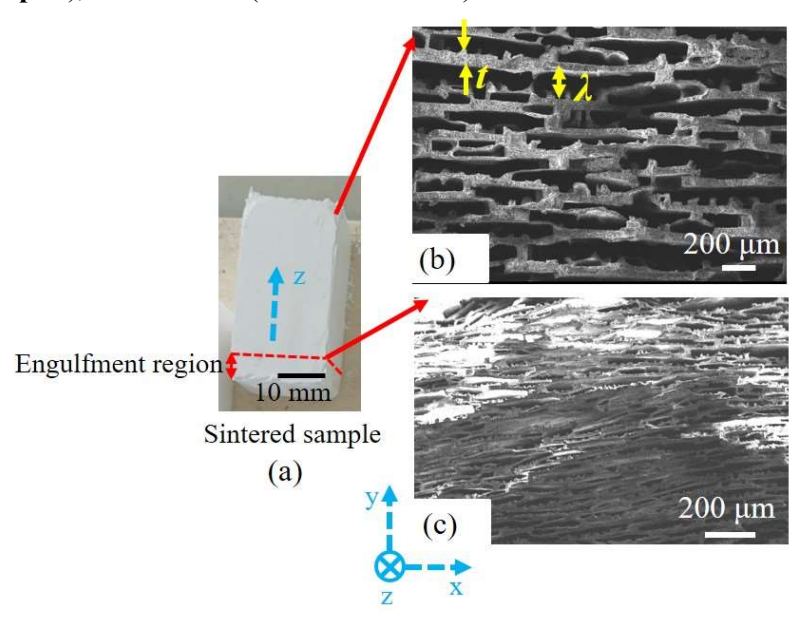


Fig. 2.9 (a) Sintered sample, representative SEM showing lamellae thickness (t), and interlamellar spacing (λ) in sintered samples for 5° wedge angle at (b) top and (c) bottom location.

The structural features i.e. lamellae thickness (t), and interlamellar spacing (λ) of lamellar sintered scaffolds are obtained from the SEM micrographs using ImageJ software. The expected engulfment region (4 to 5 mm region at the bottom freezing end) from each sample is excluded in the microstructural analysis [5]. A representative Fig. 2.9 shows the definition of lamellae thickness, interlamellar spacing, and engulfment region. The average value of these features with standard deviation as a function of position and wedge angle

is shown in the Section 3.2.2 of Chapter 3. At least 100 measurements are taken to calculate the average parameter as a function of PDMS wedge angles.

Micro X-ray computed tomography (μ XCT) is also employed to visualize the 3D lamellar structure of alumina scaffold fabricated with 10° PDMS wedge angle. The result of μ XCT is presented in the result Section 4.2.1 of Chapter 4.

The ceramic lamellae thickness (t), thickness of polymer phase (λ) , length of the brick (L), and overlap length (L_0) in brick-mortar alumina/epoxy composites are determined from the SEM micrographs using ImageJ software. At least 200 to 300 measurements are taken over multiple SEM micrographs to calculate the average microstructural parameters and associated standard deviations. The results of these microstructural parameters for brick-mortar alumina/epoxy composites are shown in the result Section 5.2.1 of Chapter 5.

2.3.2 Density measurements

The density of the sintered scaffold (ρ_s) is obtained from the ratio of measured mass to the volume. The relative density (ρ_r) is defined as $\rho_s / \rho_{\text{alumina}}$, where ρ_{alumina} is the bulk density (3.90 g-cm⁻³, taken from the datasheet provided by the supplier) of alumina. The porosity $(\varphi \%)$ of the sample is estimated through the relation $(1 - \rho_r) \times 100$. The theoretical density of lamellar alumina/epoxy composites is calculated using the rule of mixture approach and the experimental density is measured using Archimedes buoyancy principle.

2.3.3 Mechanical characterization

2.3.3.1 Tensile tests

Tensile tests on the dog bone shaped coupons are performed to record the elastic modulus, and strength of lamellar alumina/epoxy composites. The samples dimensions of the test coupons include 26 mm length (z-direction) × 3 mm thickness, (y-direction) × 5-6 mm width (x-direction). At least 3 samples are tested for each PDMS wedge angle. The testing is performed on Zwick/ Roell Z010 with 1 kN load cell at a strain rate of 0.001 s⁻¹. All samples are loaded along the lamellae direction (z-axis shown in Fig. 4.4 (a)). These specimens composed of approximately more than 150 alternate layers of alumina and epoxy across the thickness. It ensures the mechanical properties are independent of the size of the specimen [6]. All the specimens are well grounded using abrasive papers of grit sizes 1000 and 2000 before the tests. Commercial strain gauges (120 Ohms) are mounted on the samples to record the strain signals (Keysight DAQ970A) and used to find the E. Tensile tests are also performed on neat epoxy samples following the ASTM D638 [7] standard to

determine its strength. Neat epoxy samples are prepared in pre-designed mould with epoxy resin and amine hardener in the ratio of 2:1 respectively. The tensile test results of lamellar alumina/epoxy composites, and neat epoxy samples are shown in the Fig. 4.4 of Chapter 4.

2.3.3.2 Quasi-static compression tests

Quasi-static compression testing on lamellar alumina/epoxy composites is performed on Zwick/ Roell Z010 following the ASTM D695-15 standard at a strain rate of 0.001 s⁻¹ [8].

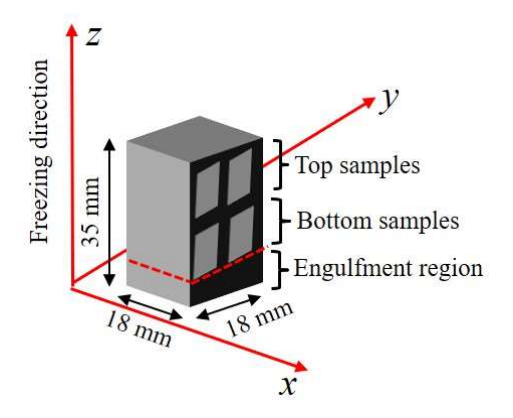


Fig. 2.10 Schematic representing extraction of samples for compression testing from the lamellar alumina/epoxy composite.

The samples with dimensions (5 mm × 5mm × 10 mm) are cut from both bottom and top locations along the x-, y- and z- directions using a low-speed diamond cutter. The expected engulfment region (4 to 5 mm region at the bottom freezing end) from the alumina/epoxy composites is excluded while extracting the samples [5]. All the specimens are well grounded using abrasive papers of grit sizes 600, 1000, and 2000 before the tests. The finishing operations are performed to ensure that samples are free from scratches and marks. The sample nomenclature for compression testing is assigned based on the PDMS wedge angle used to fabricate i.e. 0° , 5° , 10° , and 20° samples. The scheme for compression testing of cerepoxy composites is taken as – wedge angle (θ) - position of the sample (Top/Bottom: bottom denotes the side of sample closer to cold finger) - loading axis (x, y, and z). Here, the loading axis is in accordance with the coordinate frame shown in Fig. 2.10. The results of quasi-static compression tests are discussed in the Chapter 3.

2.3.3.3 High strain rate compression tests

High strain rate testing is carried out with Split Hopkinson Pressure Bar (SHPB) setup. The main components of the setup (shown in Fig. 2.11 (a)) are the striker bar, incident bar,

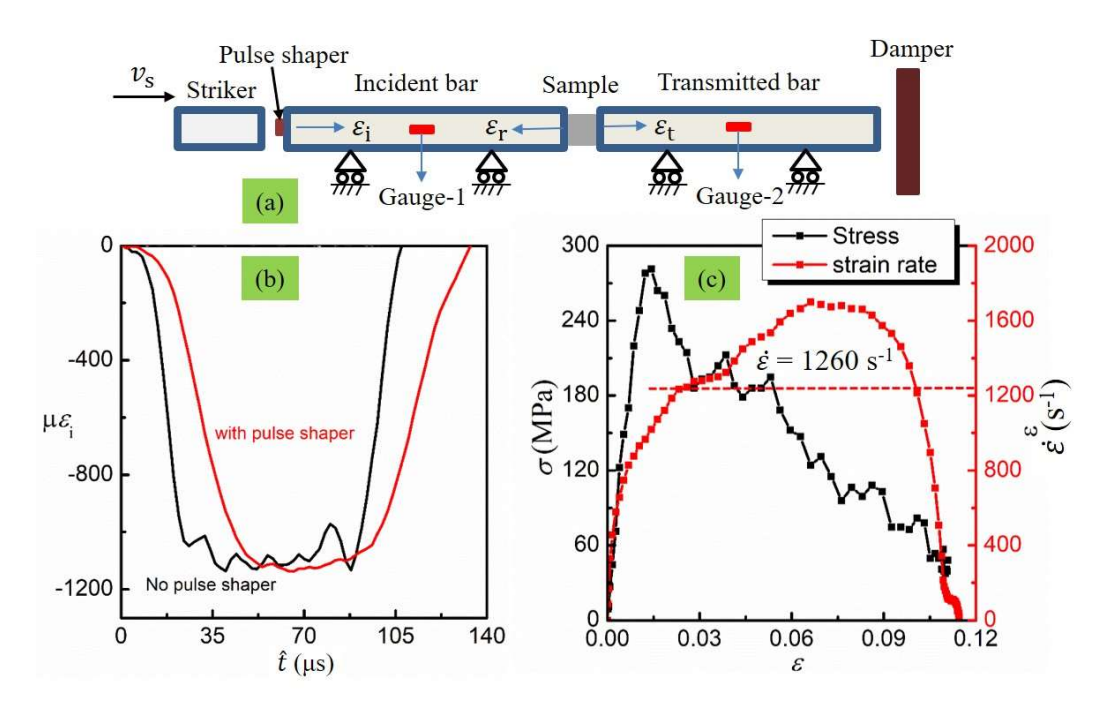


Fig. 2.11 (a) Schematic of the SHPB setup and (b) incident wave pulse with and without pulse shaper (c) representative stress-strain and strain rate-strain curves.

transmitted bar, and damper (supporting stand). The striker (25.3 mm diameter, 190 mm length) and bars (25.3 mm diameter, 1300 mm length) are made of maraging steel (E = 177GPa, $\rho = 8.07$ g-cm⁻³). The sample's dimension (10 mm x 10 mm x 5 mm) is chosen to meet the equilibrium condition and to avoid the effect of radial inertia [9]. Based upon the quasi-static results, only lamellar composite samples of 0° and 10° wedge angles from the top and bottom locations are tested. High strain rate testing of alumina scaffolds is not performed due to difficulty associated with sample preparation and precise cutting, as these scaffolds are porous and fragile. Before performing the tests, the SHPB setup is calibrated to ensure the accuracy of high strain rate tests [10]. In SHPB, the striker at fixed velocity (v_s) impacts the incident bar, which generates a compressive wave pulse (ε_i) in both the striker and incident bar. The wave pulse in the incident bar travels along its length and loads the sample in compression. During loading of the sample, a part of the wave pulse is reflected back (ε_t) , and the remaining part is transmitted (ε_t) through the sample. Fig. 2.11 (b) shows that the wave pulse is trapezoidal with a very steep rise time (24 µs) and wave dispersion when no pulse shaper is used. For high strain rate testing of ceramic materials, a general requirement of 3 to 5 wave transits within the specimen is desirable to achieve equilibrium in the sample without macroscopic failure [11]. A rubber pulse shaper (3 mm square sheet with 1 mm thickness) is used to increase the rise time and minimize wave

dispersion. Pulse shaping improves the rise time (54 μ s) and minimizes the wave dispersion as shown in Fig. 2.11 (b).

The wave speed in the sample (C_{sample}) for the z, y, and x direction of loading is calculated using Eq. (2.1) and shown in Table 2.1. The wave transit time t_s (length of the sample divided by the wave velocity in the sample) in the sample is also included in Table 2.1.

$$C_{\text{sample}} = \sqrt{\frac{E_{\text{sample}}}{\rho_{\text{sample}}}}$$
 (2.1)

Where E_{sample} is the average elastic modulus and ρ_{sample} is the average density of the cerepoxy sample (see result Section 3.2.3 and 3.2.4 of Chapter 3). From Table 2.1, the single transit time (time required for the wave to travel from one face of the sample to the other face) is in the range of 3.23 to 8.45 μ s in z-, y-, and x-directions. The rise time of 54 μ s of the loading pulse (from Fig. 2.11 (b)) ensures several wave transits within the sample prior to the macroscopic failure.

Table 2.1 Wave speed and transit time for 0° and 10° samples for different direction of loading.

Sample type	Wave speed, C_s (m/s)	Transit time, t_s (µs)
0°-z	1300.5	3.84
0° - y	591.7	8.45
0° - x	901.8	5.54
10° - z	1544.9	3.23
10° - y	599.7	8.33
10° - x	829	6.03

The strain gauges mounted at the mid-length of the incident and transmitted bars record the incident and transmitted wave pulse. The stress-strain response of the samples is obtained by the three-wave method [12] using Eq. (2.2 - 2.4).

Strain rate in the sample
$$\dot{\varepsilon}(\hat{t}) = 2\frac{C_0}{L_s} \varepsilon_r(\hat{t})$$
 (2.2)

Strain in the sample
$$\varepsilon(\hat{t}) = 2\frac{C_0}{L_s} \int_0^{\hat{t}} \varepsilon_r(\hat{t}) dt$$
 (2.3)

Stress in the sample
$$\sigma(\hat{t}) = \frac{A_{\text{bar}}}{A_{\text{sample}}} E \varepsilon_{\text{t}}(\hat{t})$$
 (2.4)

Where C_0 is the wave velocity in the maraging steel bars, L_s is the length of the sample, A_{bar} is the cross-sectional area of the incident/transmitted bar, \hat{t} is the time, and A_{sample} is the

cross-sectional area of the sample. Fig. 2.11 (c) shows the representative stress-strain and strain rate-strain curves for 0° sample loaded along the z-direction. Here, it is evident that the strain rate is not constant during the loading of the samples. Therefore, the average strain rate ($\dot{\varepsilon}_{av}$) calculated from Eq. (2.5) is used to get the stress and strain in Eq. (2.3 – 2.4) [13].

Average strain rate
$$\dot{\varepsilon}_{av.} = \frac{\int_{0}^{\varepsilon_{max}} \dot{\varepsilon}(\varepsilon) d\varepsilon}{\varepsilon_{max}}$$
 (2.5)

2.3.3.4 Nano-indentation test

The elastic modulus of epoxy phase is determined by nano-indentation testing (TI 950, Hysitron, USA) using Berkovich indenter (half angle = 65.35°). The tests are performed in the load control mode using loading and unloading rates of $100 \, \mu N/s$ with a maximum applied load of $1000 \, \mu N$ and a holding time of $20 \, s$. The nano-indentation results for epoxy phase are presented in the Section 4.2.3 of Chapter 4.

2.3.3.5 Flexural tests

Flexure tests are performed in three-point bend configuration on a universal testing machine (Zwick Roell Z010) following the standard ASTM C1161- 13 [14] As per the standard, the geometry of the samples for both lamellar and brick-mortar composites is taken as rectangular bars of size $25 \text{ mm} \times 2 \text{ mm} \times 1.5 \text{ mm}$. All samples are tested in displacement control mode at a crosshead speed of 0.2 mm/min. At least four samples per configuration are tested to measure the average strength of the composites. The strength of the composites is evaluated using Eq. (2.6).

$$\sigma_{\text{flexural}} = \frac{3F_{\text{max}}L}{2Bw^2} \tag{2.6}$$

Where, σ_{flexural} represents the flexural strength, F_{max} is the breaking force, L is the support span length, B is the specimen width, and w is the thickness of the specimen. The results of flexure tests for lamellar and brick-mortar alumina/epoxy composites are shown in the Section 5.2.2 of Chapter 5.

2.3.3.6 Fracture toughness tests

The fracture toughness tests are performed on single edge notched beam (SENB) samples using three-point bending configuration. The geometry of the samples shown in Fig. 2.12 (a) is chosen according to the ASTM E1820 standard [15]. A notch is created with diamond

abrasive cutter of 0.4 mm thickness. The notch root is sharpened by repeatedly passing a sharp razor blade to create pre-crack. The average length of notch is 1 mm with the total crack length ranges from 1.2 to 1.5 mm. The notch and pre-crack are marked in the SEM image in Fig. 2.12 (b). EDS analysis is performed to identify the epoxy and alumina phases in the sample (Fig. 2.12 (c-d)) and the respective elemental compositions are included in Fig. 2.12 (e-f). The SENB samples are tested in displacement control mode at a crosshead speed of 1 μ m/sec. In line with ASTM standard requirements and reported studies [15,16], partial unloading (10% of the current force) is allowed after every 15 μ m of load-line displacement during fracture tests. The load (F) - load-line displacement (ν) is recorded for further analysis. The elastic unloading compliance is estimated from the partial unloading curves as shown in the Fig. 2.13 (c) [15,16].

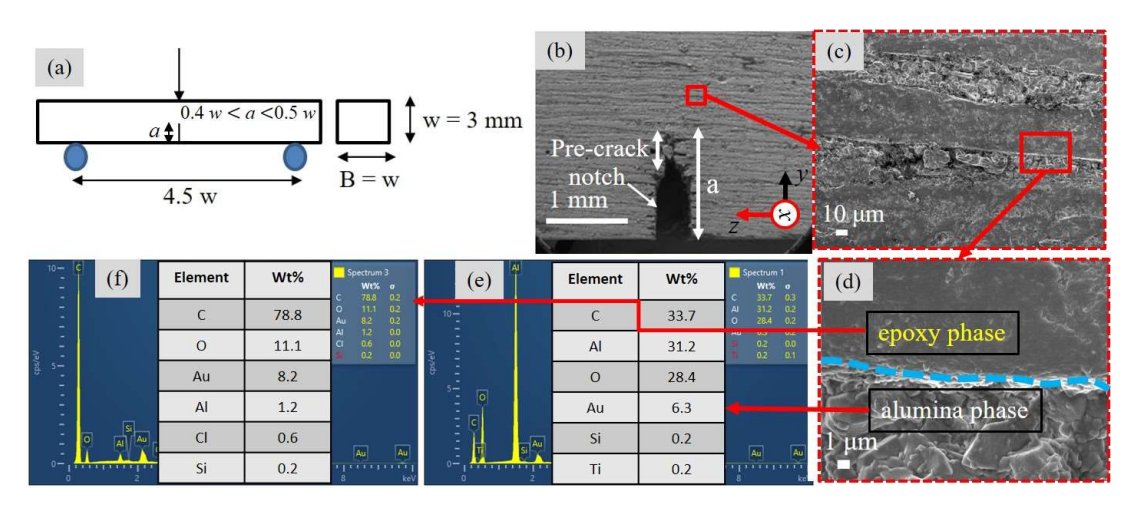


Fig. 2.12 (a) Geometry of SENB sample, (b) SEM of representative SENB sample, (c-d) SEM showing the two phases and (e-f) elemental composition in alumina/epoxy composite.

Two sets of testing are carried out to record the fracture behaviour of lamellar alumina/epoxy composites presented in Chapter 4. The first set include the effect of microstructural variation *i.e.* variation of lamellae thickness and spacing as a function of PDMS wedge angles ($\theta = 0^{\circ}$, 5° , 10° , and 20°) (Fig. 2.13 (a)). The corresponding sample nomenclature is designated as $\theta_{-}0$, $\theta_{-}5$, $\theta_{-}10$, and $\theta_{-}20$ for 0° , 5° , 10° , and 20° PDMS wedge angles respectively. For this case, the pre-crack is perpendicular to the lamellae. In the second set, crack orientation α is varied ($\alpha = 0^{\circ}$, 30° , 70° , and 90°) with respect to the lamellae for $\theta_{-}10$ samples only as shown in the Fig. 2.13 (b). The sample nomenclature in this case is taken as $\alpha 0$, $\alpha 30$, $\alpha 70$, and $\alpha 90$ based on crack orientation with respect to alumina lamellae. While the first set characterizes the effect of material microstructure and

heterogeneity, the second set of testing quantifies the role of anisotropy on the crack behaviour in lamellar alumina/epoxy composites. For each case, a minimum of 4 to 6 samples are tested to record the *F-v* responses.

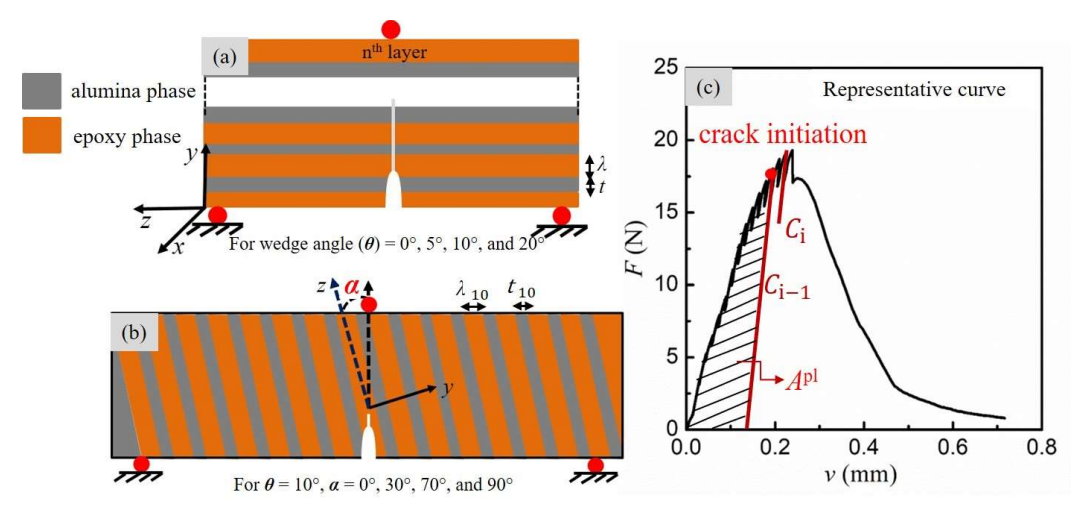


Fig. 2.13 Schematic representation of SENB samples of lamellar alumina/epoxy composites as a function of (a) wedge angle (θ). (b) crack orientation angle (α). (c) Representative F- ν curve with loading - partial unloading cycle.

The fracture toughness in terms of J- integral as a function of crack extension (Δa) is determined based on the non-linear fracture mechanics as reported in [6,15,17–19] for nacre type structures. The fracture toughness is calculated with the sum of elastic and plastic contributions. At each step of loading- partial unloading cycle, J-integral is defined by Eq. (2.7).

$$J = J_{\rm el} + J_{\rm pl} \tag{2.7}$$

Where,

$$J_{\rm el} = \frac{K_{\rm I}^2}{E'} \tag{2.8}$$

Here, $K_{\rm I}$ is the mode I stress intensity factor, $E' = E/1 - v^2$ is the plane strain modulus and v is Poisson's ratio. It is worth noting here that even though lamellar structure is fundamentally anisotropic, E' in Eq. (2.8) is evaluated by considering it as isotropic [17–20], as well as orthotropic material [6]. The value of E' varies from 19.3 GPa for isotropic case to 17.4 GPa for orthotropic case for the lamellar composites. The minor difference in elastic contribution due to variation in E' (from 19.3 to 17.4 GPa) will not significantly affects the sum of $J_{\rm el}$ and $J_{\rm pl}$ in Eq. (2.7). The stress intensity factor ($K_{\rm I}$) depends on the applied load through the relation (Eq. (2.9)) [15,17,18],

$$K_{\rm I} = \left[\frac{F_{\rm max}(4w)}{Bw^{1.5}}\right] f(a/w), \qquad (2.9)$$

where, f(a/w) is a non-dimensional function of the crack length a given by [15,17,18],

$$f(\frac{a}{w}) = \frac{3(\frac{a}{w})^{1/2} \left[1.99 - (\frac{a}{w})(1 - \frac{a}{w})(2.15 - 3.93(\frac{a}{w}) + 2.7(\frac{a}{w})^2)\right]}{2(1 + \frac{2a}{w})(1 - \frac{a}{w})^{3/2}}.$$

The plastic contribution to J-integral for non-growing crack in SENB configuration is obtained using Eq. (2.10) [15,17–19],

$$J^{\rm pl} = \frac{1.9A^{\rm pl}}{Rh} \tag{2.10}$$

Where, b is uncracked ligament (b = w - a), B is the thickness of the specimen, and $A^{\rm pl}$ is the plastic work measures from the F-v curve and unloading slope as shown in Fig. 2.13 (c). For growing crack, the ligament length (b) starts continuously decreasing then the incremental form of Eq. (2.10) is given by Eq. (2.11) [6,15,18], provided all the validity criteria discussed in Section 4.2.4.1 of Chapter 4 are satisfied [6,15,16].

$$J_{i}^{pl} = \left[J_{i-1}^{pl} + \left(\frac{1.9}{b_{i-1}}\right)\left(\frac{A_{i}^{pl} - A_{i-1}^{pl}}{B}\right)\right]\left[1 - \frac{a_{i} - a_{i-1}}{b_{i-1}}\right],\tag{2.11}$$

Where, $A_i^{pl} - A_{i-1}^{pl}$ represents the increment in plastic area in F - v curve and it is calculated using Eq. (2.12) [15].

$$A_{i}^{pl} - A_{i-1}^{pl} = (F_{i} + F_{i-1}) \left[\frac{v_{i}^{pl} - v_{i-1}^{pl}}{2} \right].$$
 (2.12)

Where, $v_i^{\rm pl}$ represents plastic part of the load-line displacement which is obtained using the relation $v_i^{\rm pl} = v_i - F_i C_i$. Here, C_i is the compliance at the $i^{\rm th}$ step, and v is the load line displacement. The crack extension (Δa) is recursively calculated based on compliance evolutions during loading – partial unloading cycles at the $i^{\rm th}$ step using Eq. (2.12 – 2.13) [15,16,19]. The value of Δa should be less than 0.25 times of uncracked ligament length (w-a) to ensure the applicability of J measurements [6,15,17,18].

$$a_{i} = a_{i-1} + \frac{w - a_{i-1}}{2} + \frac{c_{i} - c_{i-1}}{c_{i}},$$
(2.13)

$$\Delta a = a_{\rm i} - a \,. \tag{2.14}$$

It is to be noted that the crack extension (Δa) in the crack resistance curve (J - Δa) for brick-mortar alumina/epoxy composites (in Chapter 5) is determined on compliance evolutions during monotonic loading using Eq. (2.13 – 2.14) [19]. The compliance is calculated using

the relation c = v/F, where v and F represent the load-line displacement and force at each point in the F-v curve when crack starts growing.

2.3.4 Finite element simulation

To complement the results of fracture experiments for lamellar alumina/epoxy composites in Chapter 4, numerical models are developed using extended finite element method (XFEM) [21] in commercially available software Abaqus/standard 6.18. XFEM is preferred as it allows to model the crack/discontinuities within the structure by enriching the degrees of freedom with a special displacement function. The numerical simulations are carried out using cohesive segment approach with traction-separation constitutive laws (TSLs) [22,23]. The TSL accounts for elastic deformation, damage initiation, and damage evolution. The elastic properties define the initial stiffness, while the damage initiation is triggered by the maximum principal stress criteria (MAXPS) [23]. Once crack initiates, the crack propagation is governed by the fracture energy-based damage evolution criteria.

Table 2.2 Material parameters used in the numerical simulations of the alumina/epoxy lamellar composites.

Material	Young modulus	Poisson's	Maximum principal	Fracture
	(GPa)	ratio	stress (MPa)	Energy (N/mm)
Epoxy	1.94	0.3 [24]	13.27	0.2 [25]
Alumina	30	0.21 [26]	12.5	0.16

The geometry of the numerical model (Fig. 2.14) replicates the macro-scale microstructure (Fig. 2.12 (b)) of the experimental sample. As the primary aim of the numerical simulations is to understand the role of lamellae thickness and orientation on the crack behaviour in the lamellar alumina/epoxy composites, the micro-scale features such as bridges between the lamellas are not considered in the model. Numerical simulations are carried out with the following assumptions; (i) the thickness of each phase (epoxy, and alumina) is constant along its length, and have aligned lamellar structure (see Fig. 4.3 of Chapter 4), (ii) both the phases (alumina and epoxy) are modelled as linear elastic material. As reported, these assumptions simplify the model and yet provide useful insights on fracture mechanisms in lamellar composites [23,27]. Constitutive behaviour of each phase used in numerical simulations is given in Table 2.2.

To study the role of lamellae thickness and anisotropy in the lamellar alumina/epoxy composites, three sets of simulations are carried out. In the first set, the thickness t of alumina lamellae is varied in the range of 20 (t20), 40 (t40) and 80 (t80) microns with corresponding alumina volume fraction of 20%, 40%, and 80%. In the second set of simulations, the alumina volume fraction is kept constant at 50% while varying the lamellae thickness. These numerical models have lamellae thickness of t25-25 (25 microns thickness of each layer; 60 layers of each phase), t50-50, t75-75, and t100-100. The pre-crack is always perpendicular to lamellae in these two sets of simulations. Thus, they characterize the effect of lamellae thickness on the crack behavior in alumina/epoxy lamellar composites.

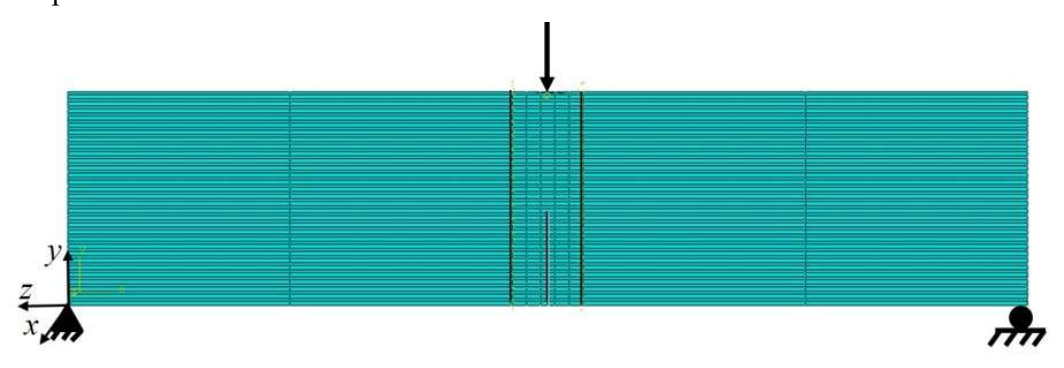


Fig. 2.14 Schematic of finite element model (t40) with boundary conditions.

The effect of crack orientation (α) on the fracture behavior of lamellar composites is considered in the third set of simulations. In these simulations, the crack orientation with respect to lamellae is varied for the base model (t40) only. Depending on the crack orientation angles ($\alpha = 0^{\circ}$, 30° , and 70°), these models are named as $\alpha 0$, $\alpha 30$, and $\alpha 90$ respectively. The numerical analysis is performed under plane strain conditions while the boundary conditions and loading are kept same as in experiments (Fig. 2.14). The specimen is discretized with a locally refined mesh having element size equal to the minimum size of the lamellae thickness in the central region (Fig. 2.14) to reduce the computational cost. Full numerical integration scheme is used in all the XFEM simulations performed here. The results of finite element analysis are discussed in the Section 4.2.4.4 of Chapter 4.

2.4 References

[1] K.H. Zuo, Y. Zeng, D. Jiang, Effect of cooling rate and polyvinyl alcohol on the morphology of porous hydroxyapatite ceramics, Mater. Des. 31 (2010) 3090–3094. https://doi.org/10.1016/j.matdes.2009.12.044.

- [2] A. Tsetsekou, C. Agra, I. Leon, A. Milias, Optimization of the rheological properties of alumina slurries for ceramic processing applications Part II: Spray-drying Optimization of the rheological properties of alumina slurries for ceramic processing applications Part II: Spray-drying, 2219 (2018). https://doi.org/10.1016/S0955-2219(00)00232-6.
- [3] H. Majidian, T. Ebadzadeh, E. Salahi, Stability evaluation of aqueous alumina-zircon-silicon carbide suspensions by application of DLVO theory, Ceram. Int. 37 (2011) 2941–2945. https://doi.org/10.1016/j.ceramint.2011.04.133.
- [4] S. Algharaibeh, A.J. Ireland, B. Su, Bi-directional freeze casting of porous alumina ceramics: A study of the effects of different processing parameters on microstructure, J. Eur. Ceram. Soc. 39 (2019) 514–521. https://doi.org/10.1016/J.JEURCERAMSOC.2018.09.030.
- [5] D. Ghosh, N. Dhavale, M. Banda, H. Kang, A comparison of microstructure and uniaxial compressive response of ice-templated alumina scaffolds fabricated from two different particle sizes, Ceram. Int. 42 (2016) 16138–16147. https://doi.org/10.1016/j.ceramint.2016.07.131.
- [6] F. Barthelat, H.D. Espinosa, An experimental investigation of deformation and fracture of nacre-mother of pearl, Exp. Mech. 47 (2007) 311–324. https://doi.org/10.1007/s11340-007-9040-1.
- [7] ASTM D638, Standard Test Method for Tensile Properties of Plastics, 2003.
- [8] ASTM D695-15, Standard Test Method for Compressive Properties of Rigid Plastics, 2010. https://doi.org/10.1520/D0695-15.
- [9] G.T. Gray III, High-strain-rate tesing of materials: the split hopkinson pressure bar, Charact. Mater., 1st ed. John Wiley & Sons, Inc., 2002. https://doi.org/10.1002/0471266965.com023.pub2.
- [10] S.N. Tiwari, P.K. Agnihotri, Effect of crumb rubber addition on the deformation and fracture behavior of ductile epoxy matrix, J. Appl. Polym. Sci. 140 (2023) 20–22. https://doi.org/10.1002/app.53255.
- [11] G. Ravichandran, G. Subhash, Critical Appraisal of Limiting Strain Rates for Compression Testing of Ceramics in a Split Hopkinson Pressure Bar, J. Am. Ceram. Soc. 77 (1994) 263–267. https://doi.org/10.1111/j.1151-2916.1994.tb06987.x.
- [12] W. W. Chen, B. Song, Split Hopkinson (Kolsky) bar: design, testing and applications, 1st ed. Springer Science & Business Media, New York, 2010. https://doi.org/10.1007/978-1-4419-7982-7.

- [13] M.F. Omar, H. Md Akil, Z.A. Ahmad, A.A.M. Mazuki, T. Yokoyama, Dynamic properties of pultruded natural fibre reinforced composites using Split Hopkinson Pressure Bar technique, Mater. Des. 31 (2010) 4209–4218. https://doi.org/10.1016/j.matdes.2010.04.036.
- [14] ASTM C1161-13, Standard Test Method for Flexural Strength of Advanced Ceramics at Ambient Temperature, 2013.
- [15] ASTM E1820 18, Standard Test Method for Measurement of Fracture Toughness, 2018.
- [16] A. Saxena, Nonlinear Fracture Mechanics for Engineers, CRC Press, Boca Raton, Florida, 1998.
- [17] E. Munch, M.E. Launey, D.H. Alsem, E. Saiz, A.P. Tomsia, R.O. Ritchie, Tough, bio-inspired hybrid materials, Science (80-.). 322 (2008) 1516–1520. https://doi.org/10.1126/science.1164865.
- [18] M.E. Launey, E. Munch, D.H. Alsem, H.B. Barth, E. Saiz, A.P. Tomsia, R.O. Ritchie, Designing highly toughened hybrid composites through nature-inspired hierarchical complexity, Acta Mater. 57 (2009) 2919–2932. https://doi.org/10.1016/j.actamat.2009.03.003.
- [19] F. Bouville, E. Maire, S. Meille, B. Van De Moortèle, A.J. Stevenson, S. Deville, Strong, tough and stiff bioinspired ceramics from brittle constituents, Nat. Mater. 13 (2014) 508–514. https://doi.org/10.1038/nmat3915.
- [20] E. Poloni, F. Bouville, C.H. Dreimol, T.P. Niebel, T. Weber, A.R. Biedermann, A.M. Hirt, A.R. Studart, Tough metal-ceramic composites with multifunctional nacre-like architecture, Sci. Rep. 11 (2021) 1–12. https://doi.org/10.1038/s41598-021-81068-z.
- [21] T. Belytschko, T. Black, Elastic crack growth in finite elements with minimal remeshing, Int. J. Numer. Methods Eng. 45 (1999) 601–620. https://doi.org/10.1002/(SICI)1097-0207(19990620)45:5<601::AID-NME598>3.0.CO;2-S.
- [22] A.E. Vellwock, L. Vergani, F. Libonati, A multiscale XFEM approach to investigate the fracture behavior of bio-inspired composite materials, Compos. Part B Eng. 141 (2018) 258–264. https://doi.org/10.1016/j.compositesb.2017.12.062.
- [23] F. Libonati, A.E. Vellwock, F. Ielmini, D. Abliz, G. Ziegmann, L. Vergani, Bone-inspired enhanced fracture toughness of de novo fiber reinforced composites, Sci. Rep. 9 (2019) 1–12. https://doi.org/10.1038/s41598-019-39030-7.

- [24] H.S. Bedi, M. Tiwari, P.K. Agnihotri, Quantitative determination of size and properties of interphase in carbon nanotube based multiscale composites, Carbon N. Y. 132 (2018) 181–190. https://doi.org/10.1016/j.carbon.2018.02.059.
- [25] N. Domun, H. Hadavinia, T. Zhang, T. Sainsbury, G.H. Liaghat, S. Vahid, Improving the fracture toughness and the strength of epoxy using nanomaterials-a review of the current status, Nanoscale 7 (2015) 10294–10329. https://doi.org/10.1039/c5nr01354b.
- [26] V. Vilchez, P.I.B.G.B. Pelissari, V.C. Pandolfelli, F. Bouville, Mixed-mode fracture model to quantify local toughness in nacre-like alumina, J. Eur. Ceram. Soc. 43 (2023) 4472–4481. https://doi.org/10.1016/j.jeurceramsoc.2023.03.044.
- [27] N.A. Abdullah, J.L. Curiel-Sosa, Z.A. Taylor, B. Tafazzolimoghaddam, J.L. Martinez Vicente, C. Zhang, Transversal crack and delamination of laminates using XFEM, Compos. Struct. 173 (2017) 78–85. https://doi.org/10.1016/j.compstruct.2017.04.011.

CHAPTER 3: Effect of freezing conditions on the microstructure and compressive response of lamellar alumina/epoxy composite

In accordance with the objective of the present study, experimental investigations are carried out to fabricate nacre-type alumina/epoxy (cerepoxy) composites using ice-templated technique. A polydimethylsiloxane (PDMS) wedge with varying angles (0°, 5°, 10°, and 20°) is used to modulate the temperature gradients during the freezing. While a 2D nucleation is observed in uni-directional freezing (0° wedge angle), bi-directional freezing in non-zero wedge angles show 1D nucleation. The lamellae thickness and interlamellar spacing increase with the increase in PDMS wedge angle. Moreover, the density of scaffolds varies along the freezing direction, with denser microstructure recorded at the bottom location (closer to the cold finger). The quasi-static and high strain rate compression testing reveals the anisotropy in the compressive mechanical properties of cerepoxy samples. The compressive strength and energy-absorbing capacity increase at higher loading rates. Finally, the present study establishes the structure-property relationship and shows that bi-directional freezing is an efficient route to design and fabricate cerepoxy composites having nacre-type microstructure.

3.1 Introduction

Designing advanced materials with high strength and toughness is desirable for many applications. However, improving both these properties simultaneously is a challenging problem. More often, there is some compromise between the two to design optimal material microstructures. Interestingly, natural material like nacre shows remarkable strength and toughness. For example, the work of fracture of the nacre is 3000 times higher than its major constituent (brittle aragonite) [1,2]. Its tensile strength may reach up to 140 - 170 MPa [3]. The combination of mechanical properties of nacre has been attributed to its hierarchical brick-mortar structure made of hard (ceramic), and soft (polymer) phases [4]. This has inspired researchers to mimic its structure to improve the strength, fracture toughness, and energy absorption capacity of artificial materials [5]. Several attempts have been made to fabricate nacre-type composites using different processing techniques [6]. Among these, ice-templating (or freeze casting) has emerged as a promising route due to its simplicity, control of processing parameters, and environment friendliness [7].

In the ice-templating technique, controlled freezing of a colloidal suspension is followed by the sublimation of frozen media (solvent) at low temperature and pressure. Subsequent sintering yields a scaffold with inter-connected pores that are the replica of the frozen solvent [8]. These pores enable the infiltration of second-phase materials to manufacture artificial nacre-type composites [8–12]. While the microstructure of the scaffold depends on several processing parameters, solidification is the key stage that determines most of the microstructural features of the scaffold [7]. A uni-directional (conventional freeze casting) temperature gradient provides a lamellar morphology with multiple small domains (submillimeter scale). However, these microstructures differ from the long-range aligned structures found in the natural nacre [13]. Lamellar orientation in the larger domain in uni-directional freezing is reported in a few studies by modifying the surface roughness [9,14] or freezing conditions [14–16].

H. Bai et al. [16] first reported the use of a bi-directional freezing strategy to produce a large-domain (up to cm scale) lamellar morphology in frozen scaffolds. They used a PDMS wedge between the cold finger and suspension to create bi-directional temperature gradients. Long-range order is reported in the hydroxyapatite (HAp) scaffold at optimum PDMS wedge angle and cooling rate. HAp/PMMA nacre-like composites are fabricated using the bi-directional freezing method with bending strength and modulus of 100 MPa, and 20 GPa respectively [10]. Later, the effect of processing parameters, i.e. cooling rate, mold slope angle, solid loading, and binder concentration on the microstructure of bidirectionally frozen alumina scaffold is studied [17]. Recently, a smart nacre-mimetic composite (alumina/Diels-Alder network polymer) with intrinsic healing and shapeprogramming capabilities has been processed using bi-directional freeze casting [18]. Even though the bi-directional freeze casting technique is used to obtain nacre-type microstructure, there is a lack of understanding of how process parameters like temperature gradients, and freezing front velocity influence the microstructure of porous scaffolds. In particular, the present study aims to address the following questions. (1) How do the temperature gradients in two directions depend on the PDMS wedge angle? (2) What is the freezing front velocity in bi-directional freeze casting? (3) How do the freezing velocity and temperature gradient influence the microstructure of ceramic scaffolds? (4) What is the structure-property relationship in alumina/epoxy nacre-type composites under static and high strain rate loading conditions?

To this end, the alumina ceramic scaffolds are fabricated at a fixed 20 vol% of loading using bi-directional freezing method. Scaffolds are also manufactured with uni-directional freezing conditions for comparison purposes. A polydimethylsiloxane (PDMS) wedge with varying wedge angles is used to induce the bi-directional temperature gradients. The range of wedge angles is motivated by the fact that the temperature gradient and velocity of the freezing front influence the microstructure (lamella thickness, lamella spacing, and alignment) of ceramic scaffolds. The freezing front velocity in the conventional freeze casting method lies in the range of $5-40 \mu m/sec$ to obtain lamellar structure [19]. However, no such range is reported for the bi-directional freezing method. Therefore, wedge angle is varied in the range of $5-20^{\circ}$ in this study. The alumina scaffold is infiltrated with epoxy using vacuum-assisted resin transfer molding (VARTM) to fabricate cerepoxy composites. The deformation behavior of cerepoxy as a function of wedge angle is investigated under quasi-static and high strain rate loading. Experimental testing shows that the wedge angle affects the average mechanical properties and failure mechanisms of cerepoxy composites. Moreover, anisotropy in mechanical properties is recorded in all types of cerepoxy samples irrespective of the wedge angle. Finally, it is shown that the wedge angle is a suitable design tool to tailor the microstructure and hence the average strength, toughness, and energyabsorbing characteristics of nacre-type composites.

3.2 Results

3.2.1 Effect of PDMS wedge angle on the structural alignment

To characterize the effect of the PDMS wedge angle on the scaffold microstructure, temperature at locations x_1 , and x_2 (Fig. 3.1 (a)) is recorded in uni- and bi-directional freezing experiments and given in Table 3.1. Fig. 3.1 (b-e) shows the temperature profiles in all four cases as a function of time (\hat{t} , in min). Expectedly, T_{x1} and T_{x2} are almost the same for 0° wedge (Fig. 3.1 (b)), while T_{x1} is lower than T_{x2} for non-zero PDMS wedge angles (Fig. 3.1 (c-f)) due to the thicker PDMS region at location x_2 in Fig. 3.1 (a). This implies that the insertion of 5°, 10°, and 20° PDMS wedge induces a horizontal temperature gradient (ΔT_x) in addition to a vertical temperature gradient (ΔT_z) that exists in 0° PDMS wedge.

The nucleation starts when the temperature above the PDMS wedge decreases below the freezing point of water. Due to the existence of only ΔT_z , the freezing starts simultaneously at all the nucleation sites randomly distributed over the PDMS wedge (2D nucleation) in case of 0° wedge angle. On the other hand, the nucleation starts at x_1 along the line 1-1'

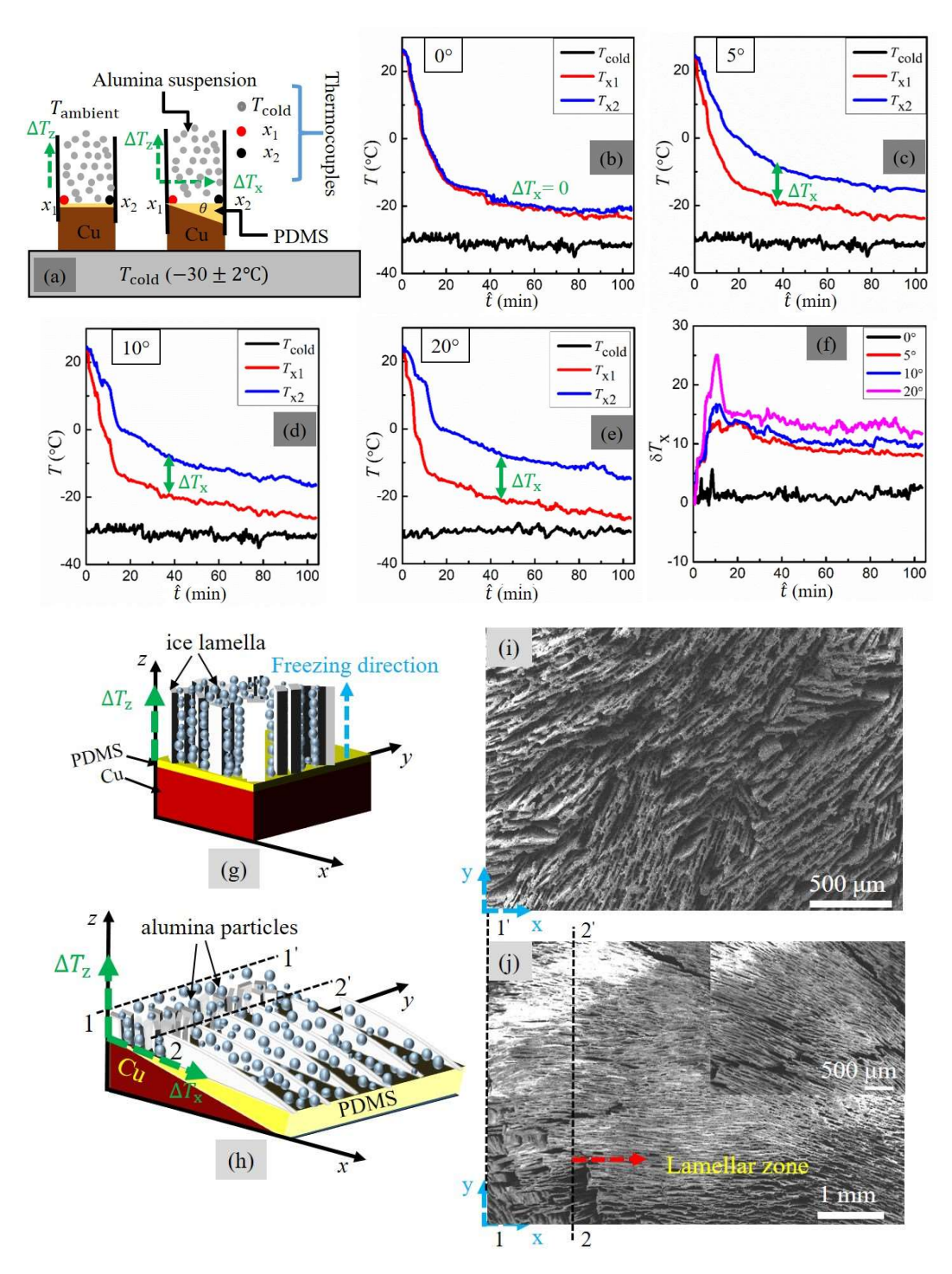


Fig. 3.1 (a) *In-situ* temperature measurement during conventional and bi-directional freeze casting. Temperature as a function of time at positions x_1 and x_2 for (b) 0° , (c) 5° (d) 10° , (e) 20° , and (f) horizontal temperature gradient for 0° , 5° , 10° and 20° . Schematic of (g) uni-directional, (h) bi-directional freezing, and evolved representative microstructures for (i) uni-directional (0°) , and (j) bi-directional freezing (10°) .

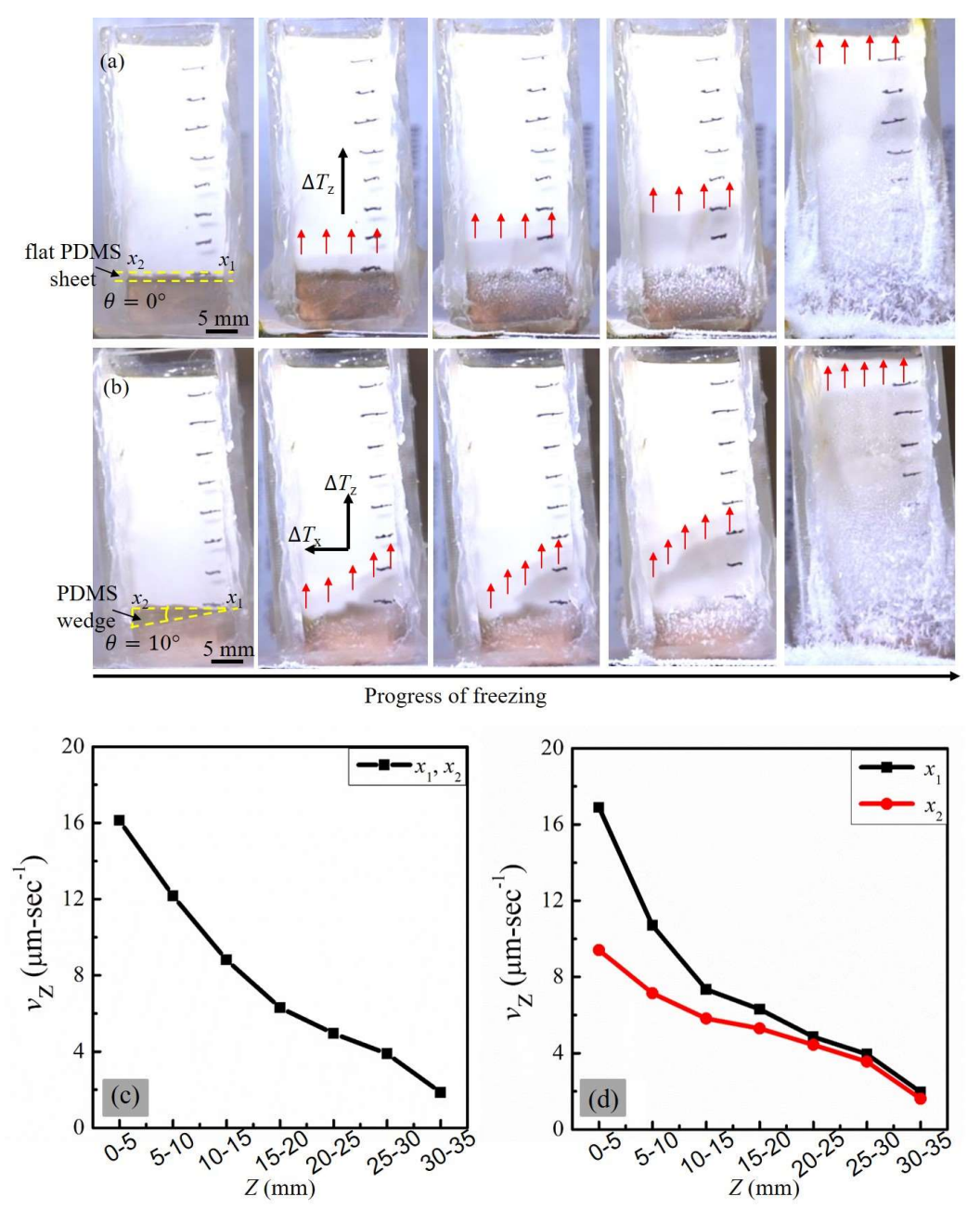


Fig. 3.2 Ice front profile in (a) uni-directional (0°) , (b) bi-directional freezing (10°) . Freezing front velocity obtained from the *in-situ* video recording (c) uni-directional temperature gradient (0°) (d) bi-directional temperature gradient (10°) .

(1D nucleation) and then gradually occurs along the x-axis till location x_2 (Fig. 3.1 (a)) in case of bi-directional freezing (Fig. 3.1 (h)). As a result, the ice crystals grow along the z-direction under the influence of ΔT_z alone in uni-directional freezing (Fig. 3.1 (g)) and the growth of ice crystals occurs along both x- and z-directions due to the dual temperature gradients in bi-directional freezing (Fig. 3.1 (h)). Consequently, randomly oriented lamellar

regions are formed in uni-directional freezing (see Fig. 3.1 (i)). A combination of randomly oriented lamellae in region 1 - 1' to 2 - 2', and a relatively larger aligned zone beyond the 2 - 2' line (Fig. 3.1 (h)) is observed in bi-directional freezing (see Fig. 3.1 (j)). This may be explained by the horizontal temperature gradient profiles compared in Fig. 3.1 (f). The horizontal temperature gradient is uniform throughout except for the initial 5 - 10 min in the bi-directional freezing case. During this time, the steady-state temperature is reached along the x-axis and freezing occurs under an almost constant horizontal temperature gradient. The freezing starts early at location x_1 (line 1 - 1') and the freezing front reaches line 2 - 2' by the time the temperature at the top edge of the PDMS wedge attains a steady state. Consequently, we get a random structure till region 2 - 2' and a relatively larger aligned zone beyond this line as shown in Fig. 3.1 (j).

The evolution of the freezing front is qualitatively investigated from the recorded video of the freezing process and the images at some time intervals are shown in Fig. 3.2 (a-b). Only two representative cases (0° and 10°) are considered for the comparison purpose. The images are presented at the same time scale as a function of freezing height (z in mm). The temperature over the PDMS surface at 0° wedge angle drops simultaneously (Fig. 3.1 (b)) and hence a flat ice front is observed in Fig. 3.2 (a). For wedge angle $\theta = 10^{\circ}$, the freezing initiates at location x_1 (Fig. 3.1 (d)) and then propagates towards location x_2 . This leads to a slanted ice front observed in Fig. 3.2 (b). Moreover, the ice front shows a gradual transition from a slant front profile to a flat front profile as the freezing progresses in bidirectional freezing in Fig. 3.2 (b). This implies that the wedge angle affects the microstructure up to a certain height (25 mm in this case) from the cold end. The freezing front velocity v_z presented in Fig. 3.2 (c-d) also confirms this proposition. The freezing velocity decreases with the freezing height (z-direction) in both cases. However, while v_z is the same at x_1 and x_2 for 0° wedge angle (Fig. 3.2 (c)), it is higher at x_1 than x_2 location for 10° wedge (Fig. 3.2 (d)). In addition, v_z at x_1 approaches v_z at x_2 as freezing progresses from the bottom to the top of the mold for 10° PDMS wedge (Fig. 3.2 (d)). The difference in v_z is reflected in the slanting of the freezing front recorded in Fig. 3.2 (a, b). The same v_z for 0° wedge induces a flat freezing front in Fig. 3.2 (a), an angled freezing front seen in Fig. 3.2 (b) is the consequence of the difference in v_z at x_1 and x_2 for 10° PDMS wedge. As the difference in v_z decreases (Fig. 3.2 (d)), the slanted front tends to be horizontal with the freezing height (Fig. 3.2 (b)).

Table 3.1 Average temperature at locations x_1, x_2 , and horizontal temperature gradient.

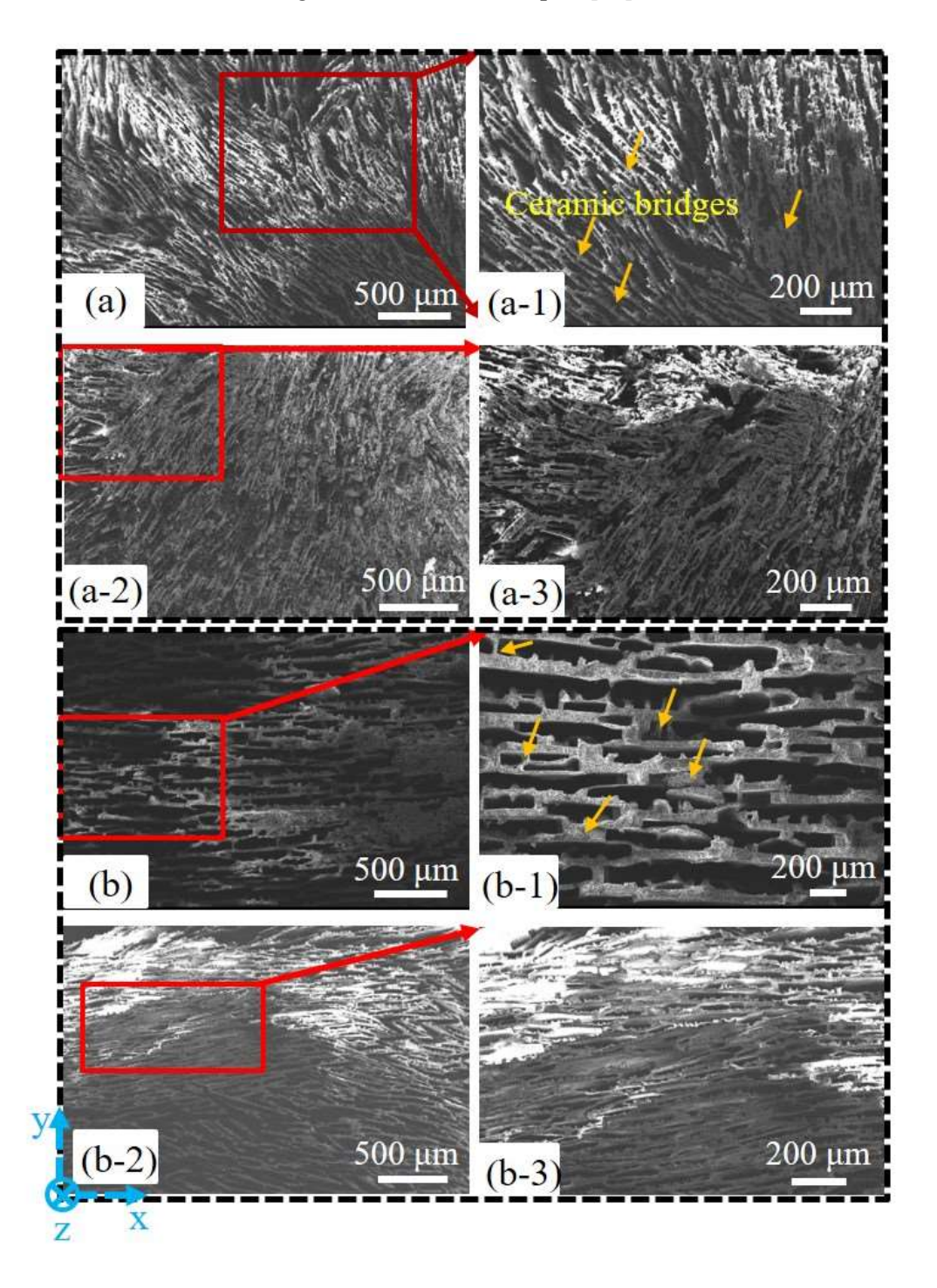
θ	<i>T</i> _{x1} (°C)	<i>T</i> _{x2} (°C)	$\Delta T_{\rm x}$ (°C)
0°	-21.3 ± 0.7	-20 ± 1.5	1.3 ± 0.7
5°	-21.4 ± 1.9	-12.5 ± 2.6	8.9 ± 0.8
10°	-22.8 ± 2.2	-12.3 ± 2.7	10.5 ± 0.5
20°	-22.9 ± 2.2	-9.8 ± 2.8	13.1 ± 0.8

3.2.2 Microstructural characteristics

The decreasing freezing front velocity (v_z) away from the cold end (see Fig. 3.2 (c-d)) will influence the scaffold microstructure. Therefore, SEM micrographs at the top (a-a1, b-b1, c-c1, d-d1) and bottom (a2-a3, b2-b3, c2-c3, d2-d3) positions of the sintered samples (0°, 5° , 10° , and 20°) in the x-y plane are shown in Fig. 3.3. The wedge angle and freezing front velocity seem to significantly affect the microstructure. In the case of uni-directional freezing, the ice nucleation is random over the 0° PDMS wedge, which results in the formation of random multiple colonies shown in Fig. 3.3 (a-a3). Moreover, as the freezing front velocity decreases with the freezing height (Fig. 3.2 (c)), finer and denser lamellae at the bottom location (Fig. 3.3 (a2-a3)) compared to the top location (Fig. 3.3 (a-a1)) are recorded in uni-directionally frozen scaffolds. The insertion of a non-zero PDMS wedge decreases the freezing front velocity and leads to gradual 1D freezing. Therefore, a relatively larger aligned zone with few domains is observed in Fig. 3.3 (b2, c2, and d2). Here again, finer microstructure is seen at bottom locations (Fig. 3.3 (b3, c3, and d3)) in comparison to samples taken from the top locations (Fig. 3.3 (b1, c1, d1)). Aligned porous lamellar structure (Fig. 3.3 (b-d), and ceramic bridges joining the adjacent ceramic lamellae wall (marked by orange arrows in Fig. 3.3 (a1, b1, c1, and d1)) are the key features of ceramic scaffolds akin to the structure of natural nacre [17,20,21]. The ceramic bridges between the lamellae walls are formed either due to the overgrown dendrites or because of the lower freezing front velocity during freezing [19].

The microstructural parameters: lamellae thickness (t), and interlamellar spacing (λ) are measured from these SEM micrographs for all types of scaffolds. The average values of these parameters for the bottom and top samples are compared in Fig. 3.4 (a-b). The lamellae thickness, and interlamellar spacing increase with the increase in wedge angle. However, both 10° and 20° samples show almost similar values of lamellae thickness, and interlamellar spacing which is consistent with the reported literature [16]. It is well established that a faster freezing front velocity leads to finer microstructure [7]. The average

freezing front velocity is higher in uni-directional freezing ($\theta = 0^{\circ}$) and hence these samples show lower lamellae thickness and interlamellar spacing observed in Fig. 3.3. The standard deviation (shown by the error bars) in Fig. 3.4 is quite large and may be attributed to the random nucleation and freezing conditions of the samples [16].



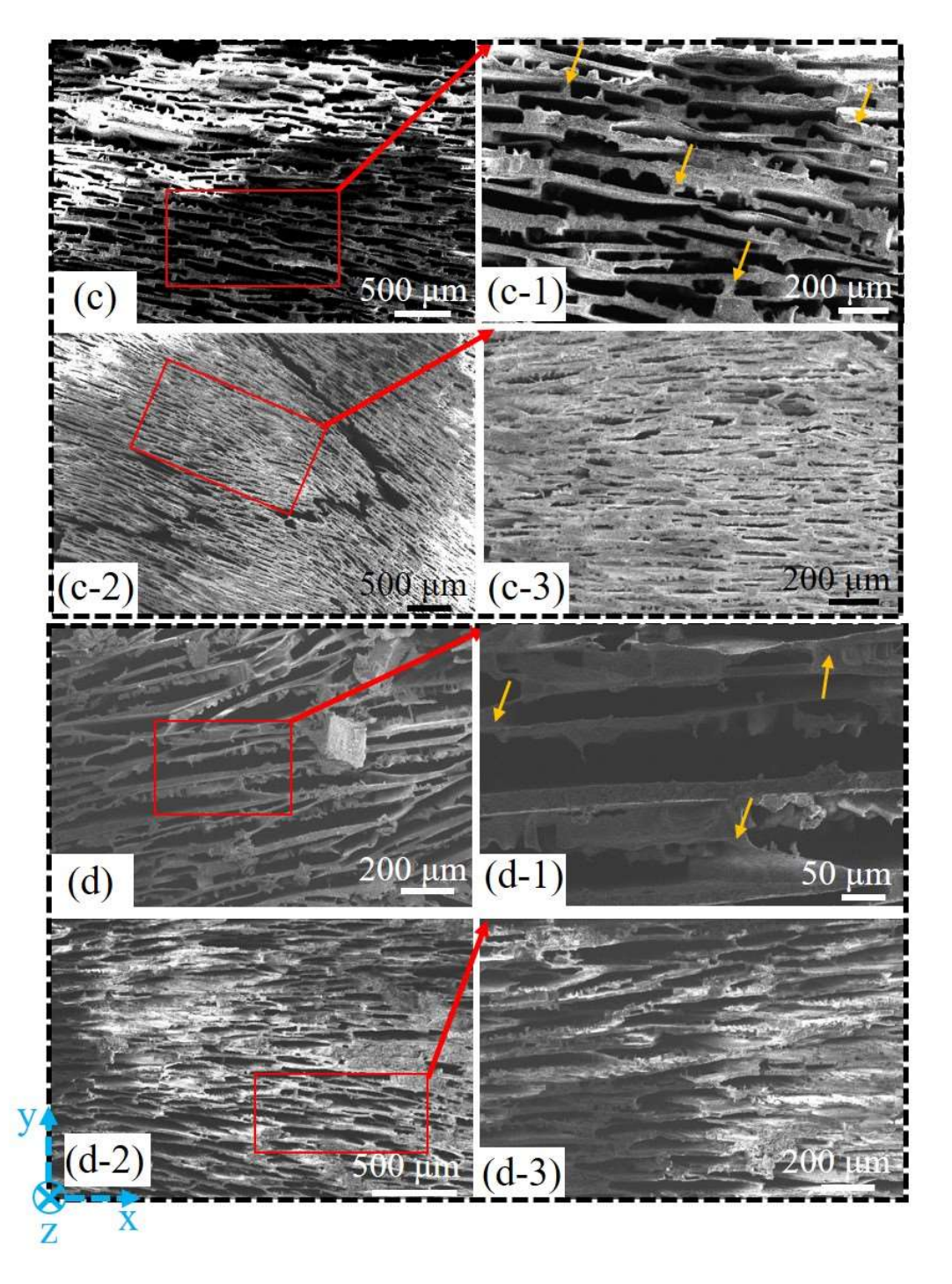


Fig. 3.3 SEM micrographs of sintered scaffold as a function of wedge angle (a-a1) 0° -top (a2-a3) 0° -bottom (b-b1) 5° -top (b2-b3) 5° -bottom (c-c1) 10° -top (c2-c3) 10° -bottom (d-d1) 20° -top (d2-d3) 20° -bottom.

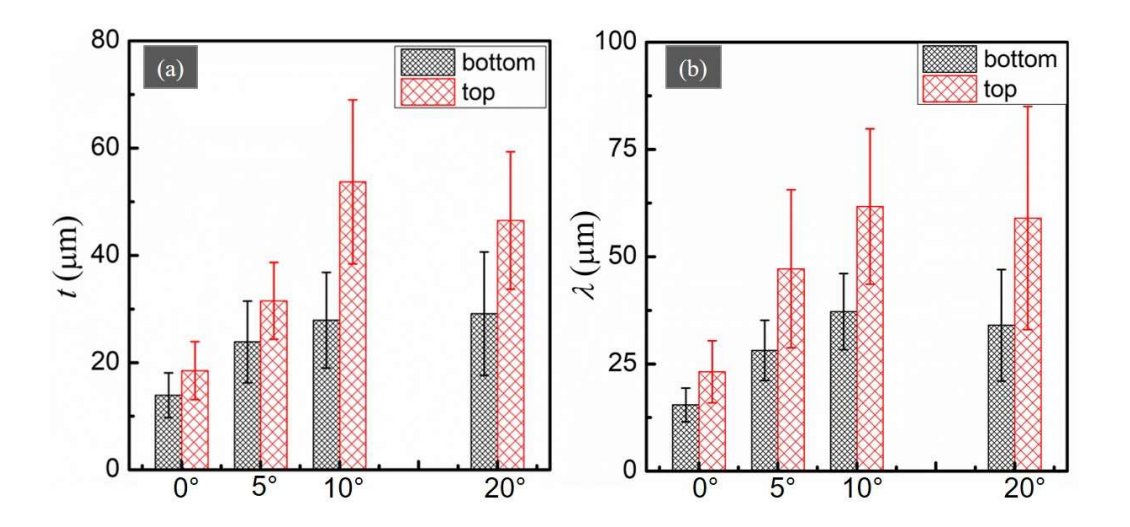


Fig. 3.4 (a) Lamellae thickness (*t*), and (b) interlamellar spacing (λ) as a function of position and wedge angle (θ).

3.2.3 Density of sintered alumina scaffolds and cerepoxy composites

The theoretical density of cerepoxy composites is calculated using the rule of mixture approach and the experimental density is measured using Archimedes buoyancy principle. At least three samples randomly taken from the top and bottom locations of the sintered scaffolds are considered to determine the average density for 0°, 5°, 10°, and 20° wedge angle cases and tabulated in Table 3.2. Expectedly, the average density is higher at the bottom than at the top for all types of samples due to decreasing freezing front velocity with the freezing height (see Fig. 3.2 (c, d)). For example, a representative optical image in Fig. 3.5 for $\theta = 0^{\circ}$ shows that the microstructure gets coarser in the freezing direction i.e. from bottom to top. The average value of the measured density for 0° scaffold at the bottom is 1.332 g-cm⁻³ and it decreases to 1.141 g-cm⁻³ at the top. A similar trend is observed for other scaffolds (5°, 10°, and 20° cases) in Table 3.2. The average density of the scaffold weakly depends on the wedge angle with a slight decrease at larger wedge angles. The average porosity (φ) of the scaffolds follows from their respective average density in Table 3.2. The sintered scaffolds are infiltrated with epoxy to process cerepoxy composites. Considering 100% infiltration, the volume fraction of epoxy is assumed to be the same as that of porosity. The theoretical density of cerepoxy composites ($\rho_{\text{(cerepoxy)}_{\text{th}}}$) is calculated following the rule of mixture approach (Table 3.3) in Eq. (3.1).

$$\rho_{\text{(cerepoxy)}_{\text{th}}} = \rho_{\text{alumina}} V_{\text{alumina}} + \rho_{\text{epoxy}} V_{\text{epoxy}}$$
(3.1)

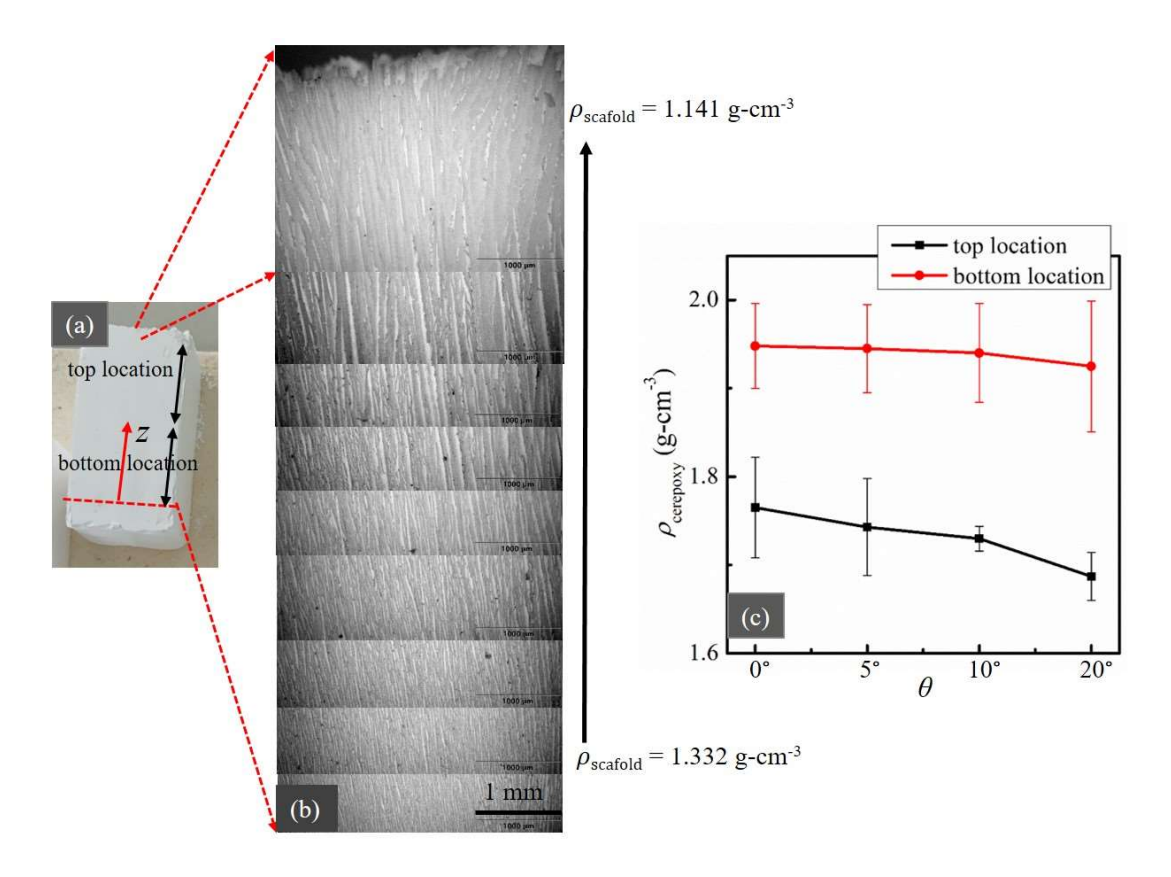


Fig. 3.5 (a) 0° sintered scaffold (b) optical image showing the evolution of microstructure for 0° sintered scaffold in the freezing direction (c) experimental density of cerepoxy composites.

The experimental density of cerepoxy ($\rho_{\text{(cerepoxy)}_{\text{exp}}}$) is obtained using Archimedes principle of buoyancy.

Table 3.2 Density of sintered alumina scaffolds and cerepoxy composites.

	Alumina scaffolds			Co	erepoxy compo	osites	
θ	ρ_{top} (g/cm^3)	ρ bottom (g/cm ³)	ρ average (g/cm ³)	Porosity (φ in %)	$ ho_{ m cerepoxy}$	$ ho_{ ext{cerepoxy}_{ ext{exp}}}$	Void fraction $V_{y}(\%)$
0°	1.141	1.332	1.205±0.109	69.09 <u>±</u> 3	1.968	1.856±0.114	5.69
5°	1.178	1.20	1.189±0.015	69.51±0.4	1.954	1.844±0.124	5.62
10°	1.148	1.180	1.164±0.022	70.15±0.6	1.941	1.835±0.125	5.46
20°	1.105	1.162	1.138±0.029	70.82±0.7	1.917	1.806±0.144	5.81

Table 3.3 Theoretical density of cerepoxy composites.

θ	ρ _{alumina} (g-cm ⁻³)	$V_{ m alumina}$	$ ho_{ m epoxy} \ m (g\text{-cm}^{-3})$	$V_{ m epoxy}$	$ ho_{(\text{cerepoxy})_{\text{th}}}$ (g-cm^{-3})
0°	3.90	0.31	1.10	0.69	1.968
5°	3.90	0.305	1.10	0.695	1.954
10°	3.90	0.3	1.10	0.701	1.941
20°	3.90	0.292	1.10	0.708	1.917

Table 3.4 Experimental density of cerepoxy composites.

	$ ho_{ ext{(cerepoxy)}_{ ext{exp}}}(ext{g-cm}^{-3})$			
θ	0°	5°	10°	20°
top location	1.806	1.782	1.74	1.668
top location	1.724	1.704	1.72	1.707
bottom location	1.914	1.981	1.98	1.978
bottom location	1.982	1.91	1.9	1.872
average	1.8565	1.84425	1.835	1.80625
standard deviation	0.114256	0.124590998	0.1258306	0.144666

Both theoretical and experimental densities of cerepoxy composites are given in Table 3.2. The experimental data for the samples extracted from the top and bottom locations of cerepoxy are given in Table 3.4 and also shown in Fig. 3.5 (c). Following the density of sintered scaffolds, the density of cerepoxy samples taken from the bottom location is comparatively higher than the samples extracted from the top location. Using the theoretical and experimental densities, the void fraction (V_v) in cerepoxy samples is obtained using Eq. (3.2) and included in Table 3.2.

$$V_{\nu}(\%) = \frac{\rho_{\text{(cerepoxy)}_{\text{th}}} - \rho_{\text{(cerepoxy)}_{\text{exp}}}}{\rho_{\text{(cerepoxy)}_{\text{th}}}} \times 100$$
(3.2)

The void fractions are almost the same in all the cerepoxy samples suggesting a uniform infiltration of epoxy in sintered scaffolds.

3.2.4 Compressive response of cerepoxy composites at different strain rates

The physical characterization reveals that the microstructure and density of scaffolds and cerepoxy composites depend on the PDMS wedge angle, freezing front velocity, and freezing height. Moreover, the scaffolds and cerepoxy composites show anisotropy in the microstructure. Therefore, it is expected that the response of cerepoxy composites will depend on the location of the sample (top or bottom), loading direction, and loading rate. Fig. 3.6 (a - l) compares the stress (σ) – strain (ε) response of cerepoxy composites at the

strain rate of 0.001 s⁻¹. The $\sigma - \varepsilon$ responses and their deformation behavior are significantly different for each type of sample. The peak load is relatively higher for all the samples when they are loaded along the z-direction in comparison to the x- or y-direction of loading. It is also noted in Fig. 3.6 that even though the peak load varies, the elastic modulus of all types of samples is nearly location-independent. The elastic modulus E (slope of the initial linear region of $\sigma - \varepsilon$ region) and strength σ (stress corresponding to the first peak) of all the cerepoxy composites are compared in Fig. 3.7. The bottom samples show relatively higher strength in comparison to the samples taken from the top location of the cerepoxy composite. This may be attributed to the finer microstructure and higher density of composites at the bottom location (see Fig. 3.5 (c)). Moreover, both elastic modulus and compressive strength show anisotropy and depend on the loading direction. The elastic modulus and compressive strength are significantly higher along the z-direction in comparison to the other two directions. While the response of the cerepoxy is primarily dominated by the harder alumina phase in the z-direction, the contribution of the softer epoxy phase increases for the x- and y-directions of loading. Consequently, the average compressive mechanical properties of cerepoxy are higher in the z-direction than in the xand y-directions in Fig. 3.7 (a-b). In addition, the elastic modulus and strength of cerepoxy also depend on the PDMS wedge angle. Both strength and modulus increase on increasing the PDMS wedge angle from 0° to 10° but decrease at 20°. This could be attributed to the increase in the lamellae thickness with the increase in the wedge angle. The small decrement in the average lamellae thickness of 20° samples might be the reason for a slight decrease in strength and modulus. These observations indicate a high degree of anisotropy in the average mechanical properties of cerepoxy samples. A large scatter in the data presented in Fig. 3.7 may be due to the randomness in the sample microstructure seen in Fig. 3.3 and similar observations are reported in the literature [22,23]. The peak strength of cerepoxy in the z-direction is relatively lower in comparison to the other work [23]. This may be due to the difference in the processing steps and the relatively low sintering temperature used in this study.

Apart from the average mechanical properties, the wedge angle also influences the failure behavior of cerepoxy composites. While most of the samples demonstrate reduced load-bearing capacity after peak stress showing the progressive type failure, catastrophic failure is recorded in a few samples. To get better insights into underlying failure mechanisms, fractography analysis of failed samples and a few partially damaged samples (for the *z*-

direction of loading case only, testing is stopped right after samples are loaded up to the peak stress to initiate damage) are compared in Fig. 3.8. The effect of uni-directional

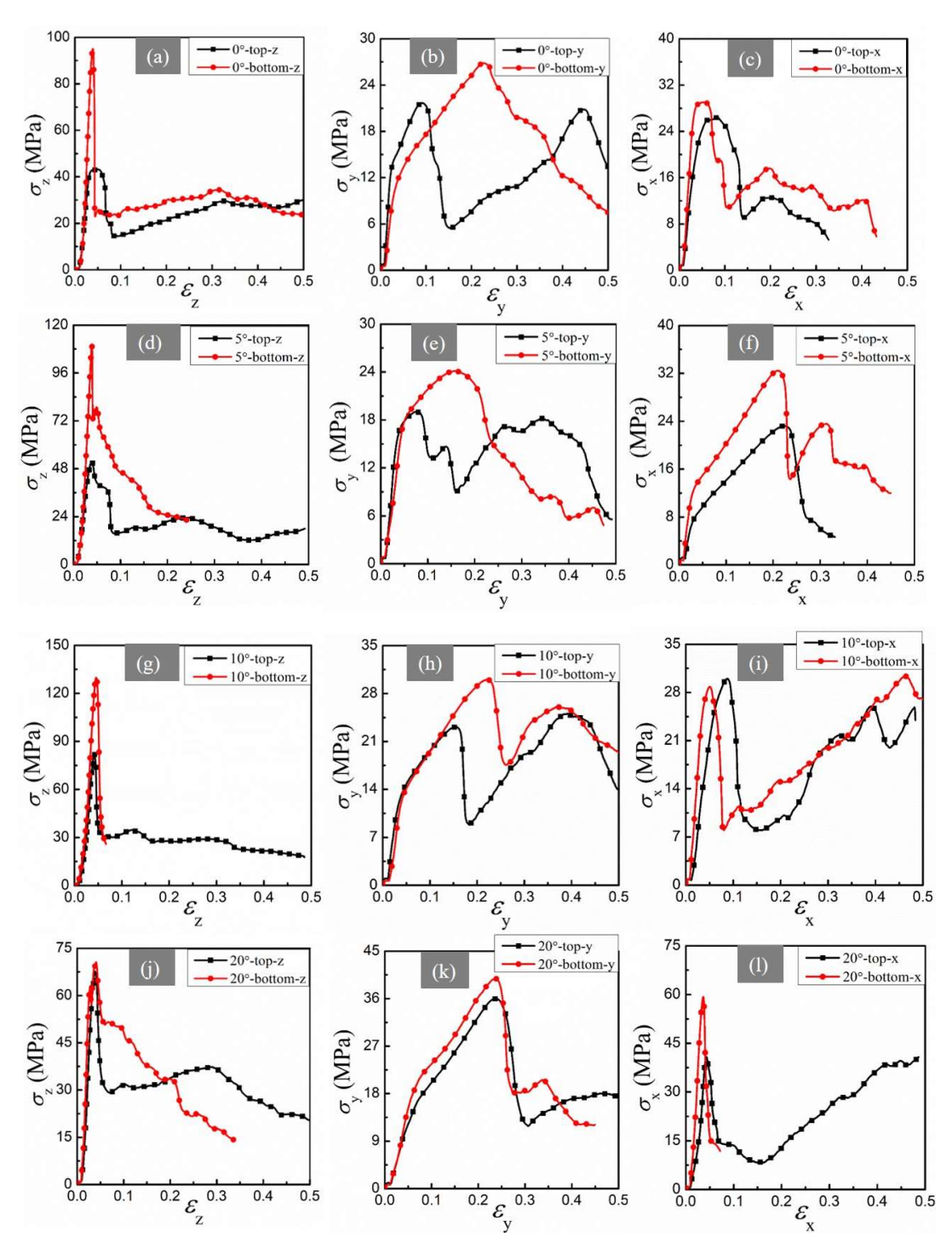


Fig. 3.6 Compressive stress-strain response of lamellar cerepoxy composites at the strain rate of $0.001 \, \text{s}^{-1}$ (a-c) 0° (d-f) 5° (g-i) 10° (j-l) 20° .

and bi-directional freezing on the failure mechanisms is investigated through the comparative SEM analysis of partially damaged/failed cerepoxy samples fabricated with 0° and 10° wedge angles only. Samples prepared with 5° and 20° wedge angles show similar deformation characteristics as recorded for 10° wedge angle samples. Delamination at the epoxy-alumina interface, crushing, bending, and buckling of alumina walls, crack deflection, and multiple cracking sites are the most common failure modes observed in these composites. These are marked in micrographs shown in Fig. 3.8.

Based on these observations, the primary causes of these failures could be the misorientation of alumina lamellae with respect to the loading direction, microstructural variations within the sample, and ceramic bridges between the adjacent lamellae. Fig. 3.8 (a) shows the optical picture of 0° partially damaged sample loaded along the *z*-direction. The SEM micrographs of damaged sites (b, c) marked in Fig. 3.8 (a) show that lamellae orientation has approximately 5 to 12° of tilt (marked in Fig. 3.8 (b-c)) relative to the loading (*z*-direction). Under axial compression, the resolved shear stress component at the interface causes delamination at the alumina-epoxy interface (Fig. 3.8 (b-c)). However, due to the presence of ceramic bridges at the interface, or multiple other domain boundaries shown in Fig. 3.3 (a-a3), the induced interfacial cracks either get arrested (leads to the formation of cracks at multiple locations, Fig. 3.9 (b'), or changes its path and grows across the lamellae (zigzag cracking (crack tortuosity) marked in Fig. 3.9 (c'-d')). Similar deformation characteristics are also seen for the 0° samples loaded in *y*, and *x*-directions (Fig. 3.8 (d-i)).

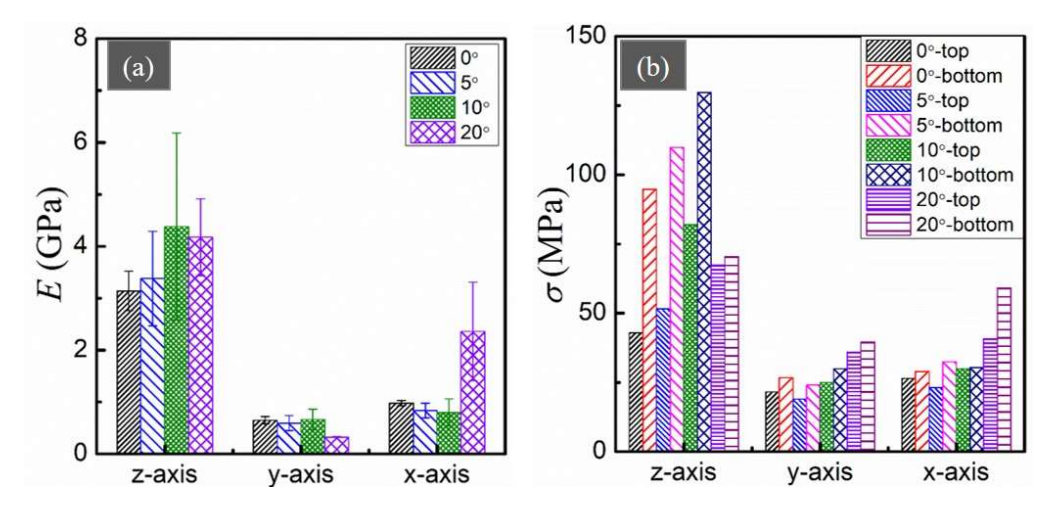


Fig. 3.7 (a) Modulus, and (b) strength of cerepoxy composites in x-, y-, and z-directions under quasi-static compression.

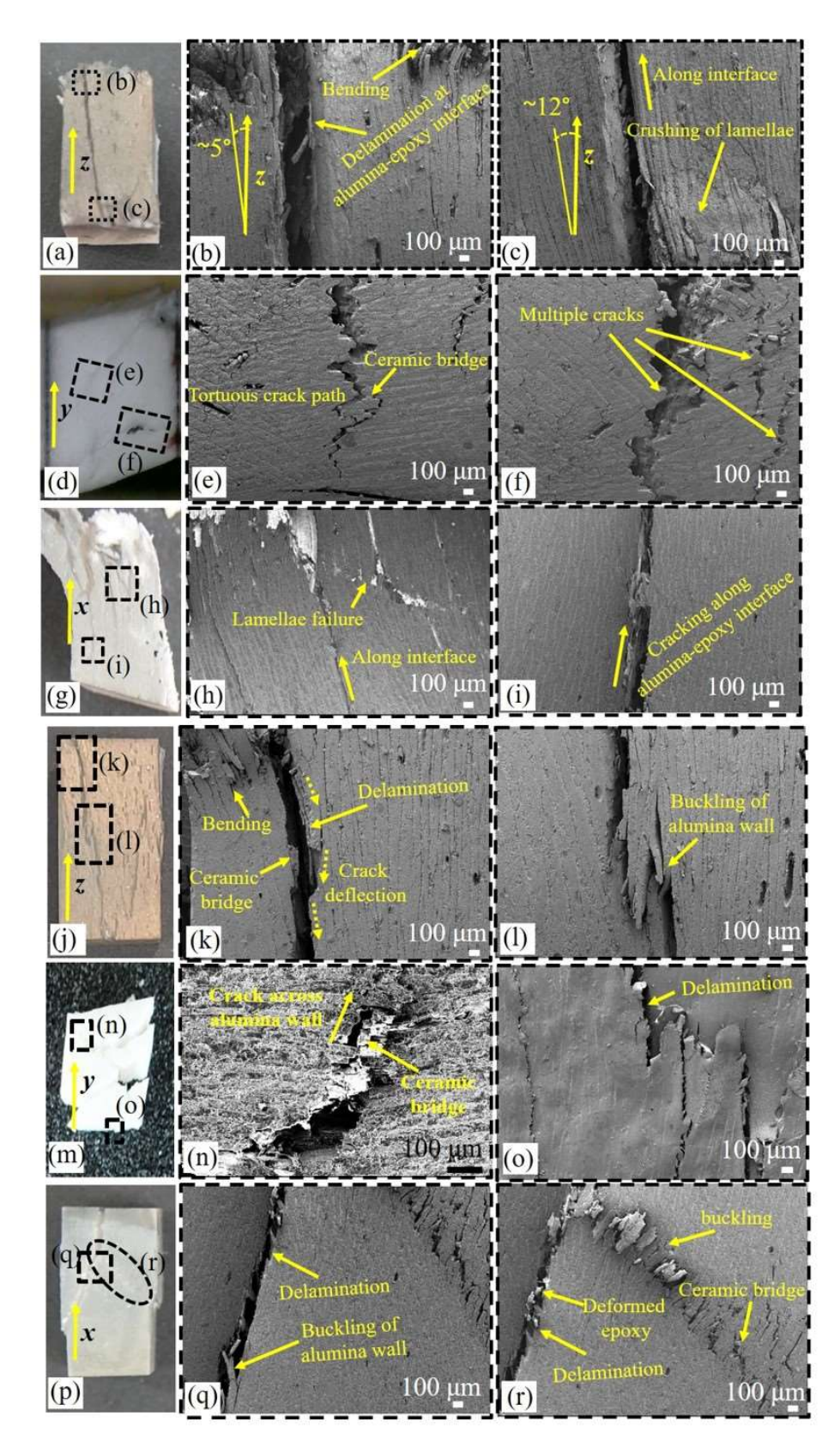


Fig. 3.8 Optical images and SEM micrographs of failed sample (a-c) 0° -z (d-f) 0° -y (g-i) 0° -x (j-l) 10° -z (m-o) 10° -y (p-r) 10° -x.

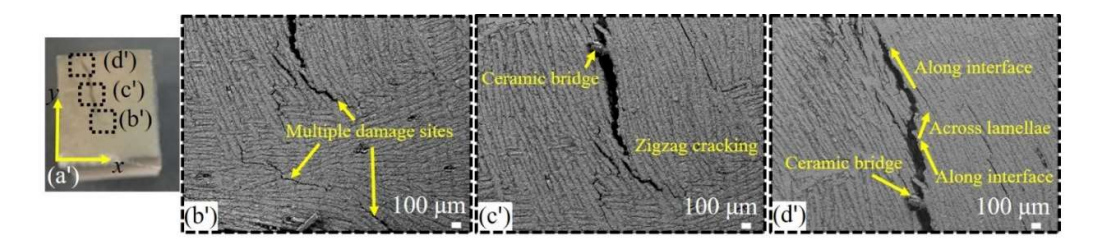


Fig. 3.9 (a') Optical image of the cross-sectional view of failed 0° sample loaded in the z-direction. (b'-d') SEM micrographs of damage sites marked in Fig. (a').

The SEM micrograph of a partially damaged 10° sample loaded in the z-direction, reveals that alumina ceramic walls fail due to both bending and buckling (Fig. 3.8 (j-r)), which is a common failure mode in anisotropic composites to decrease the overall strain energy under compressive loading [1]. As a result, both delamination and crack deflection occur as shown in Fig. 3.8 (k-1). Crack propagation through alumina lamellae, crack deflection due to the presence of ceramic bridges, and delamination is observed when 10° samples are loaded in the y-direction (Fig. 3.8 (m-o)). However, delamination and buckling are observed as dominant failure modes under the x-direction loading (Fig. 3.8 (p-r)). The presence of the aforementioned deformation patterns reveals the characteristics and features that are expected to be present in the progressive type of failure in anisotropic composites. It is also evident from the stress-strain response curve (Fig. 3.6 (a-1)), where all samples show the progressive type of deformation characteristics after reaching the peak stress except in Fig. 3.6 (g, l), where failure is catastrophic. The catastrophic failure in Fig. 3.6 (g, l) might be due to the axial splitting (delamination) of the test sample, which may occur due to variations in microstructural features (like ceramic bridges) from sample to sample. The quasi-static compression testing reveals that the cerepoxy samples prepared with 10° PDMS wedge angle have the highest modulus and compressive strength in comparison to other types of samples tested in this study.

In many applications, the composites may be subjected to high strain rate loading. Therefore, the response of 0° , and 10° wedge angle samples under high strain rate (>10³ sec⁻¹) compressive loading is compared next. The high strain rate testing is carried along z, y, and x-directions. The high strain rate testing is performed at the same striker velocity (v_s) of 11 m/s. The average strain rate according to Eq. (3.5) in these samples is included in Fig. 3.10 (a - f). The average strain rate induced in the samples varies with the loading directions with respect to the lamellae orientation. This is due to the fact that both elastic modulus of the sample varies with the direction of loading, density of the composite samples varies

with the type and position of the sample. These variations alter the transmitted and reflected strain signals acquired from the samples. The true stress-strain curves for 0° and 10° samples extracted from both top and bottom locations are shown in Fig. 3.10 (a - f). The samples taken from the bottom location show relatively larger peak strength due to their finer microstructure and higher density, which is also consistent with the results obtained at low strain rate. With respect to the loading directions, both 0° and 10° samples show higher compressive strength when loaded in the *z*- or *x*- directions. However, multiple jumps in stress are observed after the peak stress (Fig. 3.10 (e)). This may be attributed to the lamella orientation with respect to loading direction in the 10° samples in comparison to the 0° samples. Irrespective of the loading directions, a progressive type of failure is observed after reaching the peak stress for all the samples in high strain rate testing [24]. However, catastrophic type of failures may also occur at high strain rates depending on the microstructural features of the sample [23].

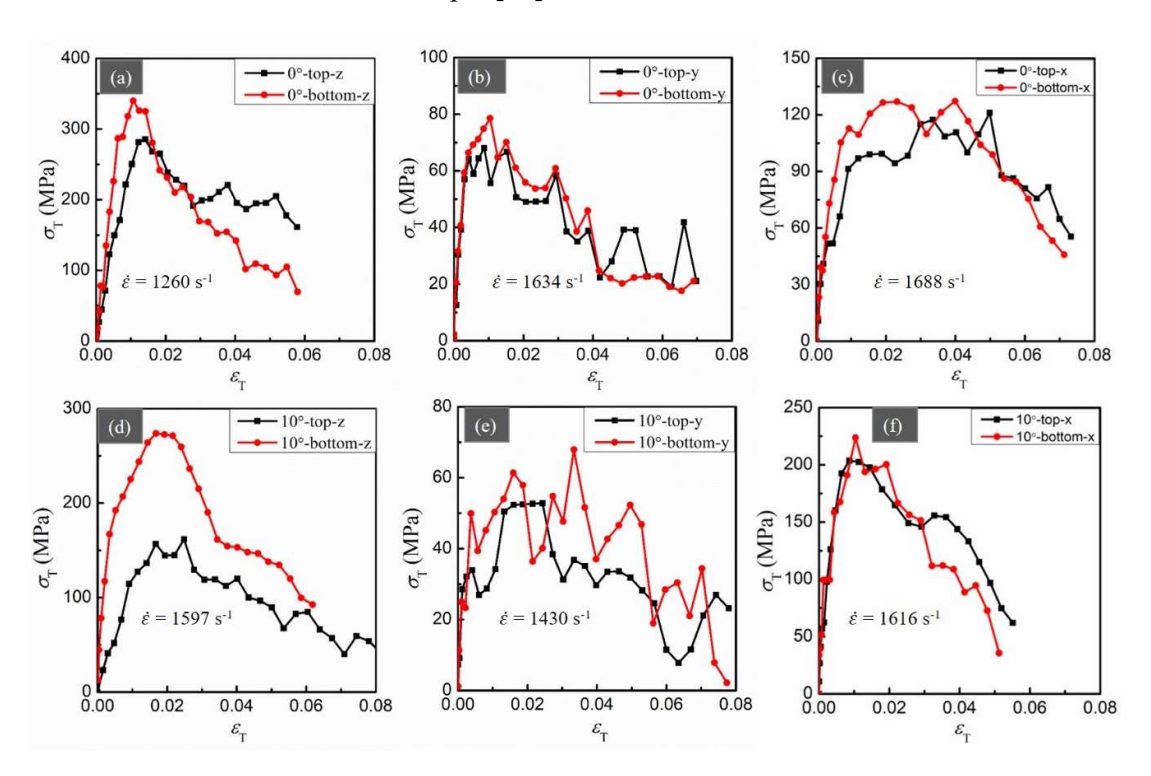


Fig. 3.10 Compressive true stress – true strain curves of cerepoxy lamellar composites as a function of loading direction at high strain rate (a - c) 0° samples (d - f) 10° samples.

3.3 Discussion

Experimental results reveal that the microstructure and hence elastic modulus, and strength of cerepoxy composites depend on the PDMS wedge angle. The introduction of non-zero

angled wedge affects the temperature distribution along the contact line of suspension and PDMS surface (x-axis) with the general observation that $T_{x1} > T_{x2}$ (see Fig. 3.1). This difference in temperature at two locations not only induces bi-directional temperature gradients, the freezing velocity (v_z) along the height (z-direction) of the suspension also varies along x as observed in Fig. 3.2 (c-d). The v_z is higher at x_1 than x_2 for the 10° wedge in Fig. 3.2 (d). It is well documented that the microstructure critically depends on the freezing velocity [7,25,26]. The decreasing v_z increases the lamellae spacing (λ) and thickness (t) along the freezing height of the frozen scaffold. This is reflected in Fig. 3.5 where a gradation in the density of the scaffold is recorded with a denser microstructure at the bottom. Moreover, the ρ is expected to be higher at x_1 than x_2 due to the higher v_z at x_1 in the non-zero PDMS wedge case. The variation in ρ_{top} and ρ_{bottom} in Fig. 3.5 (b) suggests that, though weakly, the average density of the scaffold decreases with an increase in PDMS wedge angle. Moreover, the effect of the PDMS wedge on ρ_{cerepoxy} is more pronounced at the top than at the bottom location. This implies that while the uni-directional freezing shows density variation only along z, the bi-directional temperature gradients affect the microstructure and density of scaffolds in both z- and x-directions. Moreover, the lamellar orientation and domain size also vary with the temperature gradients and freezing front velocity. Consequently, the average response of lamellar cerepoxy composites depends on the freezing conditions, loading rate, and loading directions.

To identify the optimum freezing conditions that provide higher strength and energy absorbing characteristics, the variation in strain energy density and microstructural feature (lamellae thickness) of cerepoxy composites with respect to PDMS wedge angles are compared in Fig. 3.11. Fig. 3.11 (a) compares the strain energy densities (U_{ε}) of 0° and 10° cerepoxy samples corresponding to 6% strain (a typical value of failure strain under high strain rate testing) at varying strain rates. Irrespective of the position of the sample and the loading directions, all the samples show higher strain energy density (4 to 6 times higher) at high strain rates in comparison to the quasi-static testing. U_{ε} of 10° wedge angle is comparable to the samples fabricated with 0° wedge angle when loaded in the z-direction. Fig. 3.11 (b) reveals that the lamellae thickness is higher at the top location in comparison to the bottom for all the wedge angles. On the other hand, the strength of the composite is higher for bottom samples due to higher density. Moreover, the lamellae thickness and strength are maximum for samples fabricated with 10° PDMS wedge in comparison to other samples. Therefore, 10° wedge angle is better suited to fabricate the nacre-type lamellar

cerepoxy composites with optimum mechanical properties using the bi-directional freeze casting method and slurry composition taken in this work.

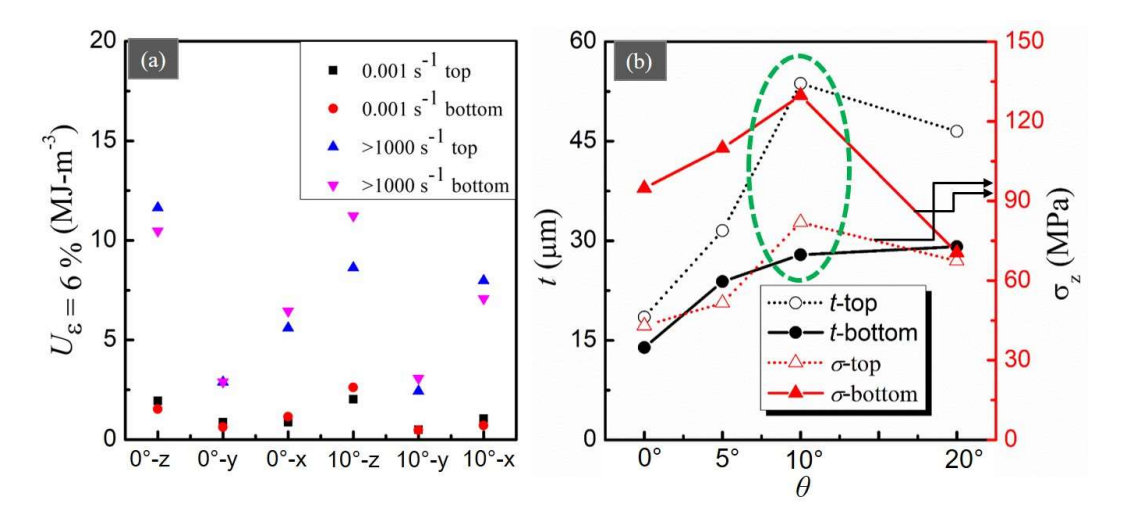


Fig. 3.11 (a) Strain energy density of lamellar cerepoxy composites at 0.001 s⁻¹ and >1000 s⁻¹, and (b) Comparison between lamellae thickness and strength (quasi-static) as a function of PDMS wedge angle.

It is to be noted here that apart from freezing front velocity, the sample microstructures depend on many other factors such as slurry composition, thermal properties of freezing layers, thermal properties of wedge and mold walls, etc. It is a challenging task to quantify the effect of all these parameters on the mechanical response of cerepoxy composites under varying loading rates. Moreover, controlling the formation of ceramic bridges between the adjacent lamellae, ensuring uniform lamellae thickness and spacing, and fabrication of larger sizes samples are some of the other limitations of the present study. Further analysis is warranted to better understand the process-microstructure-properties relationship in alumina/epoxy nacre-type composites which will be the subject of future studies. However, the present study clearly establishes the effect of freezing conditions on the microstructure and strain rate-dependent mechanical properties of cerepoxy composites.

3.4 Conclusions

This study systematically investigated the evolution of microstructure under uni-directional and bi-directional temperature gradients. Incorporating PDMS wedge over copper wedge plays a significant role in modulating the temperature gradients. Increasing the PDMS wedge angle increases the horizontal temperature gradient but decreases the freezing front velocity at the same time across the suspension. As a result, the evolved microstructural

features are greatly affected. Although the additional temperature gradient helps to align the growing ice crystal over a large domain, the thickness of growing ice crystals increases due to a decrease in ice-front velocity. Consequently, it is found that both lamellae thickness and interlamellar spacing of alumina scaffold increase with increasing PDMS wedge angle. Irrespective of the PDMS wedge angle, the lamellae thickness and interlamellar spacing also increase as a function of position in the freezing direction. The mechanical behavior of alumina/epoxy composites accessed through compressive loading reveals their anisotropy in mechanical response as well as in deformation characteristics. While the strength is found to be strongly dependent on alumina lamellae thickness, density of the composites, and loading direction, the energy absorbing capacity under high strain rate increases 4 to 6 times (up to 6 % of strain) with respect to low-strain rate tests. This shows the unique high strain rate capabilities of alumina/epoxy composites under dynamic loading. The comparison of lamellae thickness and peak strength with respect to wedge angle reveals that for the given slurry composition of 20 vol% alumina concentration, 10° is an optimum wedge angle to achieve higher strength and energy absorbing capacity in bi-directionally frozen nacre-type cerepoxy composites. Thus, the present study not only improves the understanding of the evolution of microstructure but also provides practical guidelines to process nacre-type composites using the bi-directional freezing method.

3.5 References

- [1] M.A. Meyers, P.Y. Chen, A.Y.M. Lin, Y. Seki, Biological materials: Structure and mechanical properties, Prog. Mater. Sci. 53 (2008) 1–206. https://doi.org/10.1016/j.pmatsci.2007.05.002.
- [2] J.D. Currey, Mechanical properties of mother of pearl in tension, Proc. R. Soc. London Biol. Sci. 196 (1977) 443–463. https://doi.org/10.1098/rspb.1977.0050.
- [3] A. P. Jackson J. F. Vincent, R. M. Turner, The mechanical design of nacre, Proc. R. Soc. London. B. 1277 (1988) 415–440. https://doi.org/10.1098/rspb.1988.0056.
- [4] U.G.K. Wegst, H. Bai, E. Saiz, A.P. Tomsia, R.O. Ritchie, Bioinspired structural materials, Nat. Mater. 14 (2015) 23–36. https://doi.org/10.1038/nmat4089.
- [5] H. Zhao, L. Guo, Nacre-Inspired Structural Composites: Performance-Enhancement Strategy and Perspective, Adv. Mater. 29 (2017) 1–7. https://doi.org/10.1002/adma.201702903.
- [6] I. Corni, T.J. Harvey, J.A. Wharton, K.R. Stokes, F.C. Walsh, R.J.K. Wood, A review of experimental techniques to produce a nacre-like structure, Bioinspir. Biomim. 7,

- 031001. https://doi.org/10.1088/1748-3182/7/3/031001.
- [7] S. Deville, Freeze-casting of porous ceramics: A review of current achievements and issues, Adv. Eng. Mater. 10 (2008) 155–169. https://doi.org/10.1002/adem.200700270.
- [8] S. Deville, E. Saiz, A.P. Tomsia, Ice-templated porous alumina structures, Acta Mater. 55 (2007) 1965–1974. https://doi.org/10.1016/j.actamat.2006.11.003.
- [9] M.E. Launey, E. Munch, D.H. Alsem, H.B. Barth, E. Saiz, A.P. Tomsia, R.O. Ritchie, Designing highly toughened hybrid composites through nature-inspired hierarchical complexity, Acta Mater. 57 (2009) 2919–2932. https://doi.org/10.1016/j.actamat.2009.03.003.
- [10] H. Bai, F. Walsh, B. Gludovatz, B. Delattre, C. Huang, Y. Chen, A.P. Tomsia, R.O. Ritchie, Bioinspired Hydroxyapatite/Poly(methyl methacrylate) Composite with a Nacre-Mimetic Architecture by a Bidirectional Freezing Method, Adv. Mater. 28 (2016) 50–56. https://doi.org/10.1002/ADMA.201504313.
- [11] J. Liu, R. Bai, Z. Lei, C. Xu, Q. Ye, W. Martens, P.K. Yarlagadda, C. Yan, Experimental and numerical investigation of the toughening mechanisms in bioinspired composites prepared by freeze casting, Compos. Sci. Technol. 182 (2019) 107768. https://doi.org/10.1016/j.compscitech.2019.107768.
- [12] H. Wan, N. Leung, S. Algharaibeh, T. Sui, Q. Liu, H.X. Peng, B. Su, Cost-effective fabrication of bio-inspired nacre-like composite materials with high strength and toughness, Compos. Part B Eng. 202 (2020). https://doi.org/10.1016/j.compositesb.2020.108414.
- [13] W. Gao, M. Wang, H. Bai, A review of multifunctional nacre-mimetic materials based on bidirectional freeze casting, J. Mech. Behav. Biomed. Mater. 109 (2020) 103820. https://doi.org/10.1016/j.jmbbm.2020.103820.
- [14] E. Munch, M.E. Launey, D.H. Alsem, E. Saiz, A.P. Tomsia, R.O. Ritchie, Tough, bio-inspired hybrid materials, Science (80-.). 322 (2008) 1516–1520. https://doi.org/10.1126/science.1164865.
- [15] F. Bouville, E. Portuguez, Y. Chang, G.L. Messing, A.J. Stevenson, E. Maire, L. Courtois, S. Deville, Templated grain growth in macroporous materials, J. Am. Ceram. Soc. 97 (2014) 1736–1742. https://doi.org/10.1111/jace.12976.
- [16] H. Bai, Y. Chen, B. Delattre, A.P. Tomsia, R.O. Ritchie, Bioinspired large-scale aligned porous materials assembled with dual temperature gradients, Sci. Adv. 1 (2015) 1–9. https://doi.org/10.1126/sciadv.1500849.

- [17] S. Algharaibeh, A.J. Ireland, B. Su, Bi-directional freeze casting of porous alumina ceramics: A study of the effects of different processing parameters on microstructure, J. Eur. Ceram. Soc. 39 (2019) 514–521. https://doi.org/10.1016/J.JEURCERAMSOC.2018.09.030.
- [18] G. Du, A. Mao, J. Yu, J. Hou, N. Zhao, J. Han, Q. Zhao, W. Gao, T. Xie, H. Bai, Nacre-mimetic composite with intrinsic self-healing and shape-programming capability, Nat. Commun. 10 (2019). https://doi.org/10.1038/s41467-019-08643-x.
- [19] S. Deville, Ice-Templating: Processing Routes, Architectures, and Microstructures, 2017. https://doi.org/10.1007/978-3-319-50515-2 4.
- [20] F. Barthelat, C.M. Li, C. Comi, H.D. Espinosa, Mechanical properties of nacre constituents and their impact on mechanical performance, J. Mater. Res. 21 (2006) 1977–1986. https://doi.org/10.1557/jmr.2006.0239.
- [21] H.D. Espinosa, J.E. Rim, F. Barthelat, M.J. Buehler, Merger of structure and material in nacre and bone Perspectives on de novo biomimetic materials, Prog. Mater. Sci. 54 (2009) 1059–1100. https://doi.org/10.1016/j.pmatsci.2009.05.001.
- [22] S. Akurati, J. Marin, B. Gundrati, D. Ghosh, Assessing the role of loading direction on the uniaxial compressive response of multilayered ice-templated alumina-epoxy composites, Materialia 14 (2020) 100895. https://doi.org/10.1016/j.mtla.2020.100895.
- [23] S. Akurati, N. Tennant, D. Ghosh, Characterization of dynamic and quasistatic compressive mechanical properties of ice-Templated alumina-epoxy composites, J. Mater. Res. 34 (2019) 959–971. https://doi.org/10.1557/jmr.2019.30.
- [24] M. Banda, D. Ghosh, Effects of porosity and strain rate on the uniaxial compressive response of ice-templated sintered macroporous alumina, Acta Mater. 149 (2018) 179–192. https://doi.org/10.1016/j.actamat.2018.02.027.
- [25] T. Waschkie, R. Oberacker, M. J. Hoffmann, Investigation of structure formation during freeze casting from very slow to very fast solidification velocities, Acta Mater. 59 (2011) 5135-5145. https://doi.org/10.1016/j.actamat.2011.04.046.
- [26] V. Naglieri, H.A. Bale, B. Gludovatz, A.P. Tomsia, R.O. Ritchie, On the development of ice-templated silicon carbide scaffolds for nature-inspired structural materials, Acta Mater. 61 (2013) 6948–6957. https://doi.org/10.1016/j.actamat.2013.08.006.

CHAPTER 4: Characterizing crack behavior in lamellar alumina/epoxy composites: microstructure and crack tortuosity

In the previous Chapters, methods are developed to fabricate long-range aligned lamellar alumina scaffolds and alumina/epoxy composites. The structure - property relations for lamellar alumina/epoxy composites are established at varying loading rates. It is noticed that such lamellar structures show anisotropic mechanical response as well as deformation characteristics in compression. Therefore, it becomes essential to understand underlying failure mechanisms and crack behaviour in anisotropic alumina/epoxy composites for the efficient design. To this end, fracture experiments are performed to record the crack evolution as a function of lamellae thickness and crack orientation. The mode-mixity K_{II}^k/K_I^k at the deflected crack tip is evaluated analytically for all cases. To experimentally characterize the anisotropy in crack propagation, a non-dimensional parameter $\delta^* = \max\{|\delta^+|, |\delta^-|\}/\min\{|\delta^+|, |\delta^-|\}$ is proposed using crack mouth opening displacement (CMOD) measurements. The variables δ^+ , and δ^- represent CMOD on the either side of the current location of the crack tip. It is shown that δ^* follows the variation of K_{II}^k/K_I^k and thus can be used to predict the degree of mode-mixity in crack propagation. Extended finite element simulations (XFEM) are carried out to compliment the experimental understanding of crack behavior in lamellar composites. Finally, this study reveals new insights on crack growth and proposes an experimentally measurable parameter to quantify the mode mixity in lamellar anisotropic composites.

4.1 Introduction

Design and fabrication of strong, tough, and lightweight materials is desirable in many areas including protective systems, structures, automobiles, and space applications [1–3]. Designing artificial materials having high strength and toughness is a very complex and challenging problem. Most of the engineering materials exhibit conflict between strength and toughness due to their inherent material characteristics [4]. Interestingly, there is a class of natural materials that show high strength and toughness [2]. One of the widely cited example is the nacreous part of sea shell with fracture toughness 1000 times higher than its major constituent because of its hierarchical brick-mortar type structure [5,6]. Consequently, efforts have been made to fabricate nacre-like structures using several fabrication routes [7]. Among these, bi-directional freeze casting route has emerged as one

of the most promising method to fabricate long-range aligned lamellar structure over multiple length scales akin to the nacre [8–11].

The fabrication, structural characterization, mechanical, and fracture testing of nacre-like artificial composites is key to experimentally realize stronger and tougher materials [12-19]. The nacre-like ceramic/polymer composites show improved mechanical response as well as rising crack resistance curves [12–14]. The ceramic/polymer composites are usually toughened with crack arrest at the interface, crack bridging and deflection due to stiffness mismatch between the constituents [20]. Using freeze casting technique, E. Munch et al. developed lamellar alumina/PMMA composites which show rising crack resistance curve with fracture toughness (K_I) values up to 15 MPa-m^{0.5} [12]. The metal/ceramic composites are mostly toughened due to large plastic deformation and crack bridging in the metal layers [21–23]. Ceramic/ceramic laminated structures are designed with weak interfaces to increase the fracture toughness [16,24]. Bouville et al. [24] have used silica and calcia as the secondary phases to fabricate alumina/silica-calcia composites having initiation toughness of 6.1 MPa-m^{0.5} and maximum toughness ($K_{\rm J}$) of 17.3 MPa-m^{0.5}. In addition to the experimental observations, numerical models are also developed to quantify the onset of crack deflection in nacre-like alumina composites [25,26]. Recently, a phase-field fracture model is proposed to understand the influence of oblique angle i.e. the angle between loading and platelet directions, on the strength and fracture behaviour of nacretype composites [27].

Although improvements in mechanical performance and fracture toughness have been reported for nacre-like artificial composites, the underlying mechanisms driving the crack initiation and propagation is not well understood yet. The cracks do not follow the self-similar growth process in these anisotropic layered materials. Moreover, quantifying the crack behaviour is rather difficult due to the complex crack path with multiple crack deflections. Most of the studies [13,14,18,23] use ASTM E1820 to characterize the crack in nacre-like composites. But, ASTM E1820 [28] standard assumes that there is single crack propagating in pure mode I only. It does not consider the mode mixity and complex crack paths present in the nacre-like composites. Another standard ASTM C1421 [29] which is used to measure the fracture resistance of advanced ceramics, only accounts for materials which show brittle nature with catastrophic failure. Hence, the measured R-curves using these standards provides a global averaged fracture response only. They do not account the local mode mixity at the crack tip and the how the local anisotropy influences the crack

propagation. Characterizing the crack behavior and mode mixity at the crack tip as a function of the material anisotropy in nacre-like layered composite materials is the primary objective of the present work.

To this end, nacre-like lamellar alumina/epoxy composites with varying microstructural features (lamellae thickness, lamellae spacing and orientation) are fabricated using bidirectional freeze casting method [11]. Fracture testing is performed to record the fracture toughness using single edge notch beam (SENB) tests [28]. The local stress intensity factors and mode mixity at the deflected crack tip are calculated using analytical relations. Later on, the mode mixity in fracture tests is quantified using crack mouth opening displacement (CMOD) measurements. A non-dimensional CMOD, $\delta^* = \max\{|\delta^+|, |\delta^-|\}/\min\{|\delta^+|, |\delta^-|\}$ is defined to quantify the deviation of crack growth in anisotropic nacre-like layered materials from the self-similar crack growth conditions as shown in Fig. 4.1. The variation of δ^* with lamellae orientation and crack angle follows the mode mixity K_{II}^k/K_I^k obtained from the analytical and numerical simulations. It is shown that δ^* can be used to characterize the crack behaviour in nacre-like layered anisotropic composite materials. Finally, the relevance of the current study in the context of microstructure, toughening mechanisms, and fabrication of bio-inspired lamellar composites is discussed.

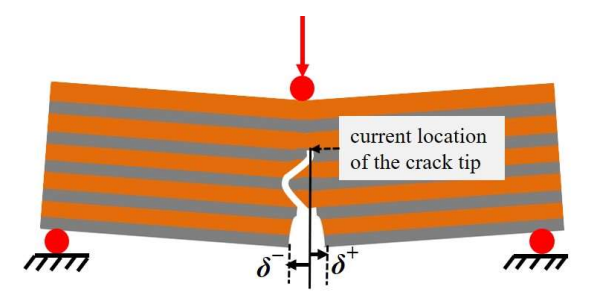


Fig. 4.1 Schematic of CMOD measurement in layered alumina/epoxy composite during fracture tests.

4.2 Results

4.2.1 Microstructural characteristics

Fig. 4.2 (a) shows the schematic of bi-directional freeze casting. A representative SEM micrograph of lamellar ceramic scaffold is shown in Fig. 4.2 (b). Both interlamellar spacing (λ) and lamellae thickness (t) (refer Fig. 4.2 (b1)) increase with the increase in PDMS wedge angle. However, the fabricated scaffolds usually show large scatter in lamellae

spacing and thickness [8,9,11]. The scatter in these microstructural features is included as error bars in Fig. 4.2 (c). The alumina scaffolds are infiltrated with epoxy to prepare alumina/epoxy composites with lamellar architecture (see Fig. 4.2 (d)). The complete details of alumina/epoxy composites fabrication are given in [11]. The detailed 3D lamellar structure of alumina scaffold fabricated with 10° PDMS wedge angle obtained from micro X-ray computed tomography (μ XCT) is shown in Fig. 4.3 (a-d). It is to be noted here that lamellar structure fabricated in this study is recorded in the sample size of $16 \times 12 \text{ mm}^2$ which is significantly higher than the earlier reported study ($7 \times 3 \text{ mm}^2$) [8]. However, at higher magnifications (smaller length scale), the ordered microstructure may show randomness shown in Fig. 4.2 (b).

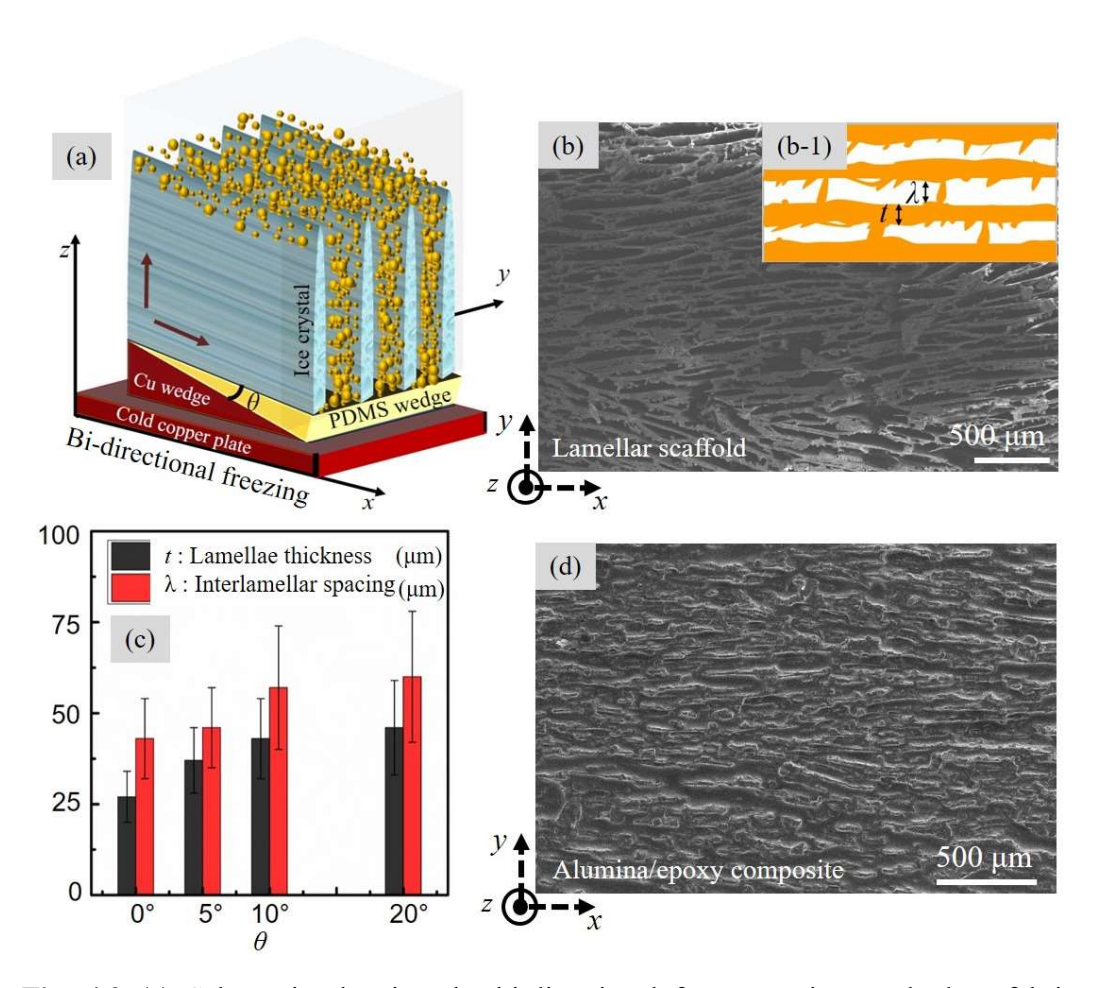


Fig. 4.2 (a) Schematic showing the bi-directional freeze casting method to fabricate lamellar alumina scaffold. (b) SEM image of alumina scaffold. (b-1) Schematic showing lamellae thickness (t), and interlamellar spacing (λ) . (c) Variation of t, and λ as a function of PDMS wedge angle (θ) . (d) SEM image of alumina/epoxy composite.

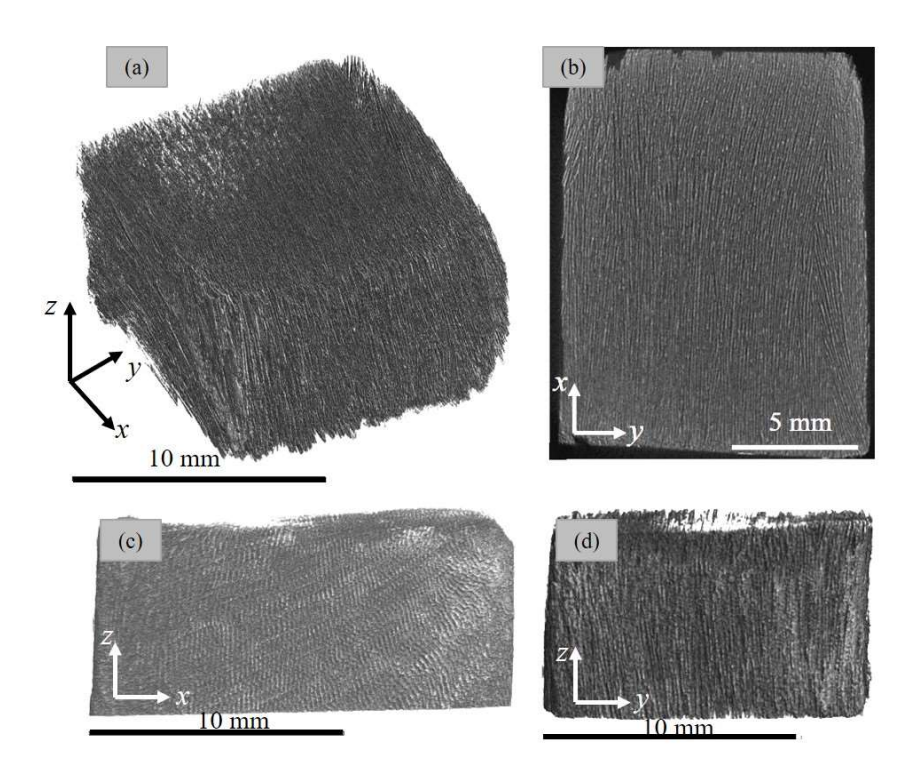


Fig. 4.3 Micro X-ray computed tomographs (μ XCT) of alumina scaffold fabricated with 10° PDMS wedge angle (a) 3-D image of the sample (16 × 12 × 6 mm³) and the corresponding 2-D images in (b) *x-y* plane (c) *x-z* plane (d) *y-z* plane.

4.2.2 Tensile testing

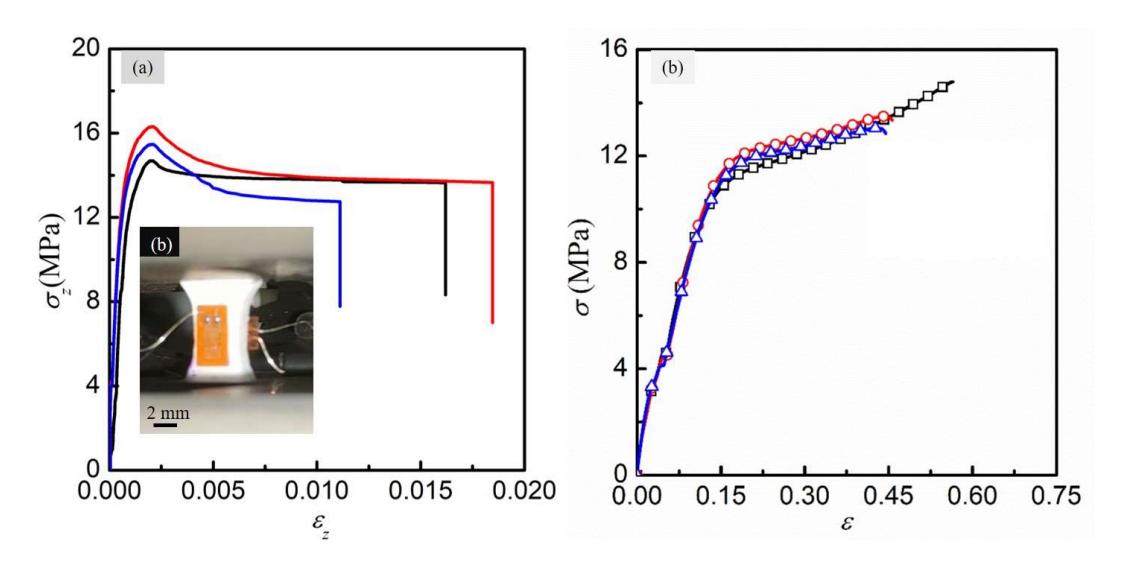


Fig. 4.4 (a) Tensile stress - strain curve of (a) lamellar alumina/epoxy composite, and (b) neat epoxy.

The stress – strain curves recorded from the tensile test on dog bone shaped coupon for lamellar alumina/epoxy composites are shown in Fig. 4.4 (a). To eliminate the effect of

machine compliance, material anisotropy and inhomogeneity, the sample strain is recorded with the strain gauge mounted on the sample. The initial response is linear elastic ($E \sim 17.65$ GPa) followed by a plateau yield stress of 16 MPa. As the deformation progresses, the material is strain softened and failed at a strain of around 0.018. The elastic modulus, and tensile strength of the lamellar composites are 18 ± 2 GPa and 15 ± 1.5 MPa respectively and can be treated as insensitive to the PDMS wedge angle θ when loaded along the z-direction. Fig. 4.4 (b) shows the stress – strain curves for neat epoxy samples. The measured average modulus and tensile strength of neat epoxy sample is found to be 1.94 GPa and 13.27 MPa respectively.

4.2.3 Nano-indentation result

The recorded load – indenter displacement data for neat epoxy sample is shown in Fig. 4.5. Due to very high modulus of indenter (1140 GPa), the reduced modulus (slope of unloading F - v curves) of neat epoxy sample is approximated as the modulus of epoxy. Using load – indenter displacement data, the measured value of average elastic modulus of neat epoxy is 1.94 GPa.

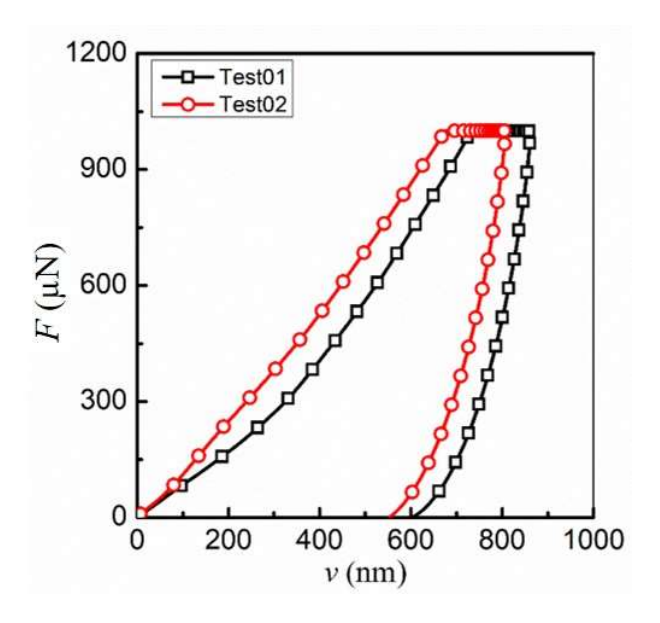


Fig. 4.5 Indentation load – displacement curves for neat epoxy.

4.2.4 Fracture toughness measurements

The fracture behavior of each type of composites for both the schemes are characterized under three point bending of SENB samples. In the first scheme, the crack is made perpendicular to the lamellae orientation, while thickness of epoxy and alumina layer varies *i.e.* effect of PDMS wedge angles. In the second scheme, the average thickness of epoxy

and alumina is same (for θ_10 samples only), while the crack orientation is varied with respect to the lamellae.

4.2.4.1 Effect of lamellae thickness on J

The F-v curves recorded from SENB testing of lamellar alumina/epoxy composites for θ _0, θ _5, θ _10, and θ _20 samples are shown in Fig. 4.6 (a-d). Appearance of knee in some F-v curves is observed in the load range of 3-8 N. No crack growth is recorded at such low loads and it may be associated with the nature of epoxy used in this study [30]. The bell shape of all the curves indicates a stable crack propagation [5,31]. The J - Δa (J_R) curves are constructed using the data shown in F-v curves following Eqs. (2.6 – 2.13) of the Chapter 2. It must be noted here that considerable inelastic region exists ahead of the crack tip in nacre, and laminated composites [5,32]. Thus, nonlinear fracture mechanics-based J-integral approach is preferred to characterize the material toughness. The condition for J-dominance in SENB specimen is [5,31]:

$$B, w - a \ge 25 \frac{J_{Q}}{\sigma y}. \tag{4.1}$$

Moreover, as the crack advances, the material ahead of the crack tip experiences unloading, which contradicts J-integral validity. However, under limited amount of crack growth, J still characterizes the state of stress at the crack tip if [5]:

$$\frac{w-a}{J} \frac{\partial J}{\partial a} >> 1.$$
(4.2)

It is important to mention here that the Eq. (4.1 - 4.2) is derived for isotropic materials and have limited validity for anisotropic materials. However, they are assumed to be valid for nacre-like lamellar structure if $\omega > 1$ and $\Delta a < 0.25(w - a)$ [5,12,13]. To ensure the applicability of J measurements, the evolution of ω and Δa is monitored and it is recorded that ω remains greater than 4.5 and $\Delta a < 0.25(w - a)$ during the crack growth in the valid region marked in Fig. 4.6 (e). Beyond this region, the large-scale yielding may take over and J become geometry dependent [31]. Following the Eq. (4.1 - 4.2), the J-valid region is marked in the J_R curves shown in Fig. 4.6 (e). While the initial toughness (J_{min}) of all the samples is similar $(0.2 - 0.5 \text{ kJ-m}^{-2})$ and does not show a particular trend. This may be attributed to the location of pre-crack tip and microstructural randomness in the experimental samples. The J_{max} (~2.3 kJ-m⁻²) is higher for θ _10 and θ _20 samples having

relatively thicker alumina phase. Moreover, the J_{max} is 3 to 7 times of J_{min} for all types of composites leading to the rising J_{R} curves in Fig. 4.6 (e). The rising J_{R} curves indicate that the existing pre-crack or other flaws present in the microstructure are stable, a typical characteristic of damage-tolerant material as reported for natural nacre [33]. It is a very useful property to ensure integrity of structural materials during service conditions.

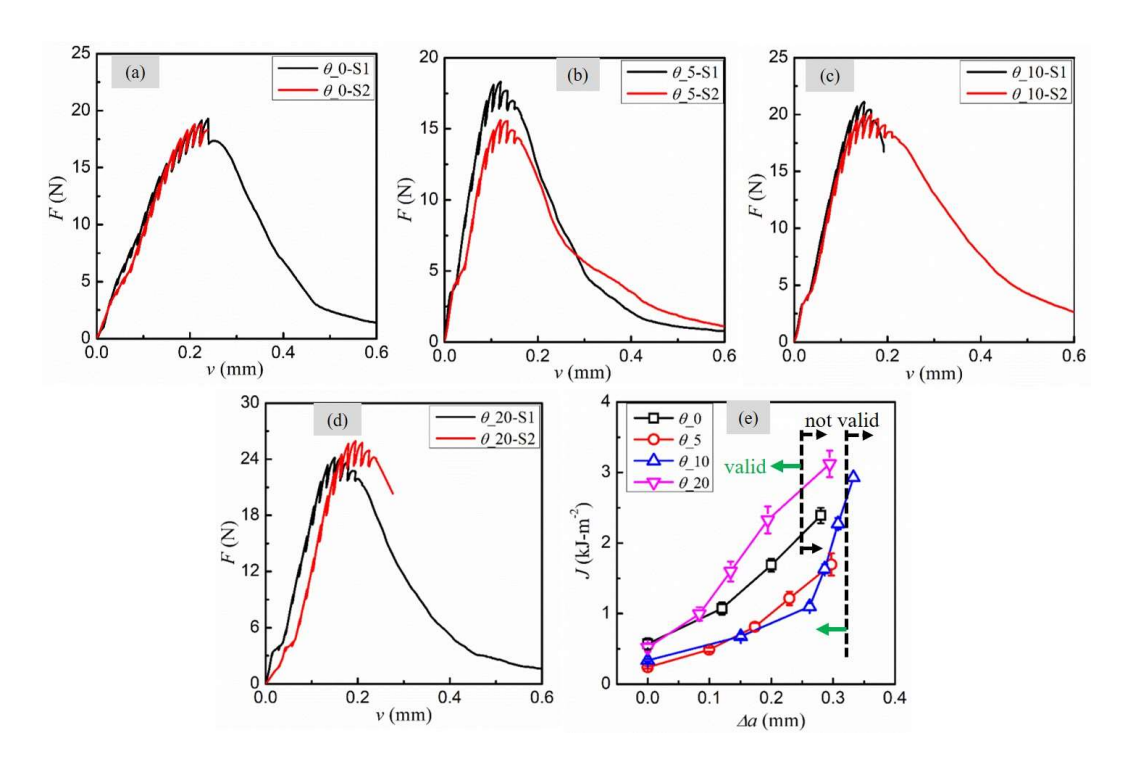


Fig. 4.6 F-v curves for (a) θ_0 (b) θ_5 (c) θ_1 0 and (d) θ_2 0 lamellar alumina/epoxy composite samples from SENB testing. (e) $J - \Delta a$ curves of lamellar alumina/epoxy composites fabricated with varying PDMS wedge angles (θ).

4.2.4.2 Effect of crack orientation on J

The effect of crack orientation ($\alpha = 0^{\circ}$, 30° , 70° , and 90°) on the F-v response of lamellar alumina/epoxy composites is shown in the Fig. 4.7 (a - c). Here again, the curves are bell shaped and the peak load increases as the crack orients perpendicular to the lamellae. Moreover, the J_{\min} increases with the crack orientation in Fig. 4.7 (d). The J_{\min} of $\alpha 90$ (0.34 kJ/m²) is 4 times higher than $\alpha 0$ (0.08 kJ/m²). All the samples show rising J_R curves regardless of the crack orientation and the J_{\max} for $\alpha 90$ sample is approximately 3.5 times higher than the J_{\max} of $\alpha 0$. These observations reveal that it is easier for the crack to propagate along alumina/epoxy interface in $\alpha 0$ samples than growing through the alumina or epoxy phase in $\alpha 90$ case. However, the exact crack growth and toughening mechanisms

are not clear yet. To understand this, detailed fractography analysis of all the tested samples is performed and discussed next.

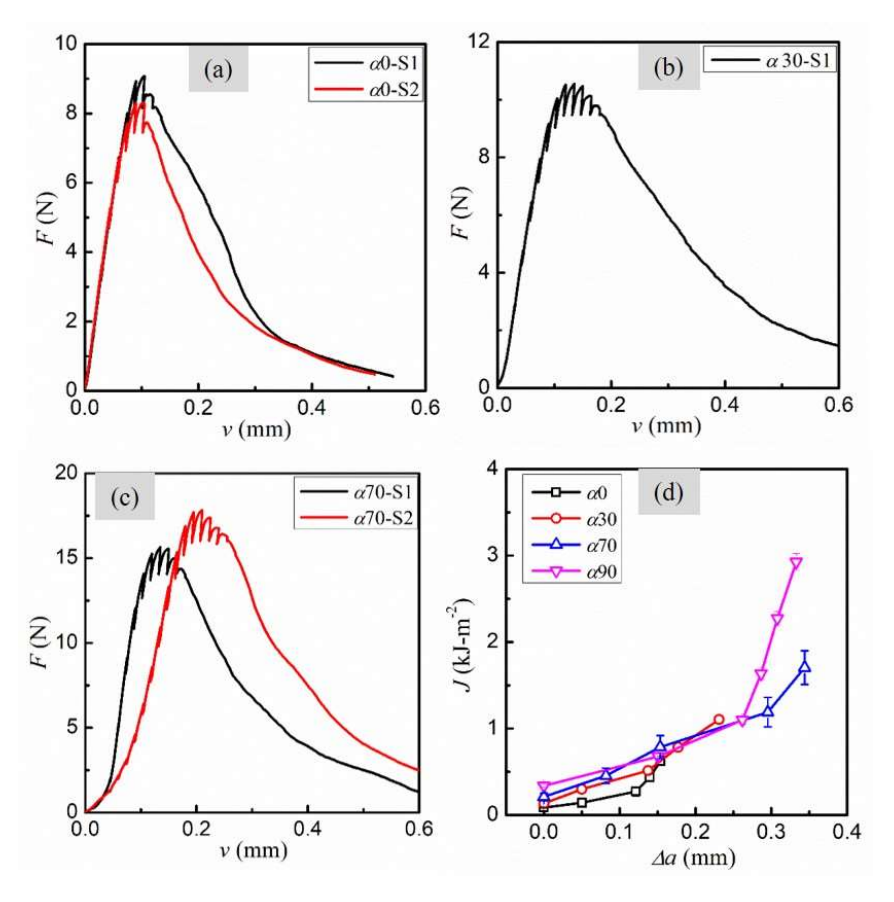


Fig. 4.7 F-v curves of composite samples having crack orientation of (a) α 0 (b) α 30 and (c) α 70 in SENB fracture tests. (d) J - Δa curves as a function of α .

4.2.4.3 Toughening mechanisms

Fig. 4.8, and Fig. 4.9 show the SEM micrographs of fractured surfaces of θ_-0 , and θ_-10 samples. The fracture characteristics in θ_-5 and θ_-20 samples are similar and shown in the Fig. 4.10 and Fig. 4.11 respectively. The SEM of θ_-0 sample before the test in Fig. 4.8 (a) shows that the pre-crack is perpendicular to the layered multiphase structure. The crack forms a tortuous path as it grows through the thickness of the sample in Fig. 4.8 (b). A similar crack growth behaviour is reported for other types of materials with lamellar and nacre like microstructure including natural nacre [2,5,34]. It may be attributed to the presence of two phases in the material. Each phase has a preferential crack growth direction depending on its type and composition. While crack grows under the influence of maximum normal stress in alumina phase, it prefers to grow along maximum shear stress direction in

relatively softer epoxy phase in alumina/epoxy composites. As a result, it forms a tortuous crack growth profile in the sample. The scatter in lamellae orientation within the microstructure of the sample (see Fig. 4.8 (a)) also contributes in crack deflection. To get better insights, the two crack faces are examined under SEM and shown in Fig. 4.8 (b1-b2). The corresponding magnified surfaces are shown in Fig. 4.8 (c1-c3) and 4.8 (d1-d3) respectively. In Fig. 4.8 (b1-b2), the yellow dotted line marks the tip of the pre-crack on two crack faces and the arrow denotes the crack growth direction.

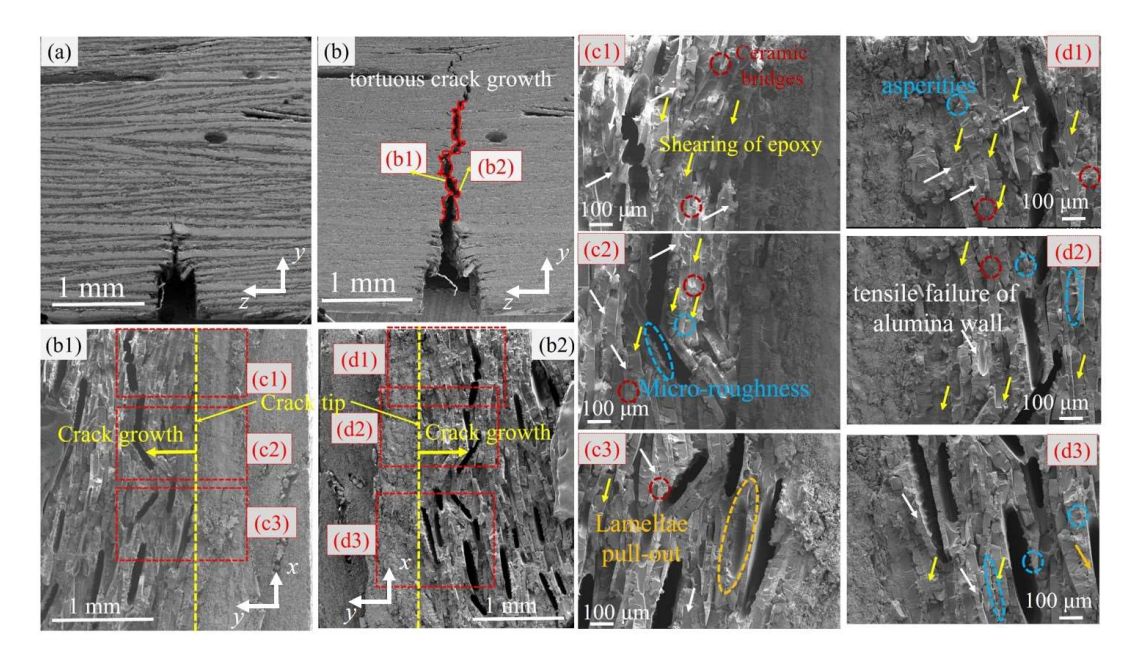


Fig. 4.8 (a) SEM of untested θ_0 SENB sample. (b) Fractured SENB sample, showing tortuous crack paths (b1) left fractured surface, and (b2) right fractured Surface (c-d) magnified view of left and right fractured surfaces near the crack tip respectively.

The fractured surfaces show regions of smoother and rough features along with the signatures of multiple toughening mechanisms in Fig. 4.8 ((c1-c3) - (d1-d3)). Shear yielding of epoxy phase, breaking of lamellae, crack deflection, and lamellae pull-out are found to be the dominant failure mechanisms that contribute towards resistance against the crack propagation and hence rising J_R curves of alumina/epoxy lamellar composites. Ceramic bridges (marked by red circle), micro- asperities, and roughness (marked by light blue) also contribute to both stiffness and toughness of these composites [15]. Similar features are observed on the failed surfaces of θ_1 10 (Fig. 4.9) as well as in θ_2 5 and θ_3 20 sample shown in the Fig. 4.10 and Fig. 4.11 respectively. In addition, de-bonding at the interface and relatively larger crack deflection is recorded in θ_3 10 (Fig. 4.9) and θ_3 20 (Fig.

4.11) samples. The larger crack deflection may be attributed to the thicker alumina phase present in these samples (see Fig. 4.2 (c)). These additional mechanisms lead to higher J_{max} for $\theta_{-}10$ and $\theta_{-}20$ samples in comparison to $\theta_{-}0$ and $\theta_{-}5$ samples in Fig. 4.6 (e). Thus, the higher lamellae thickness introduces additional failure mechanisms and improves the fracture toughness of alumina/epoxy lamellar composites.

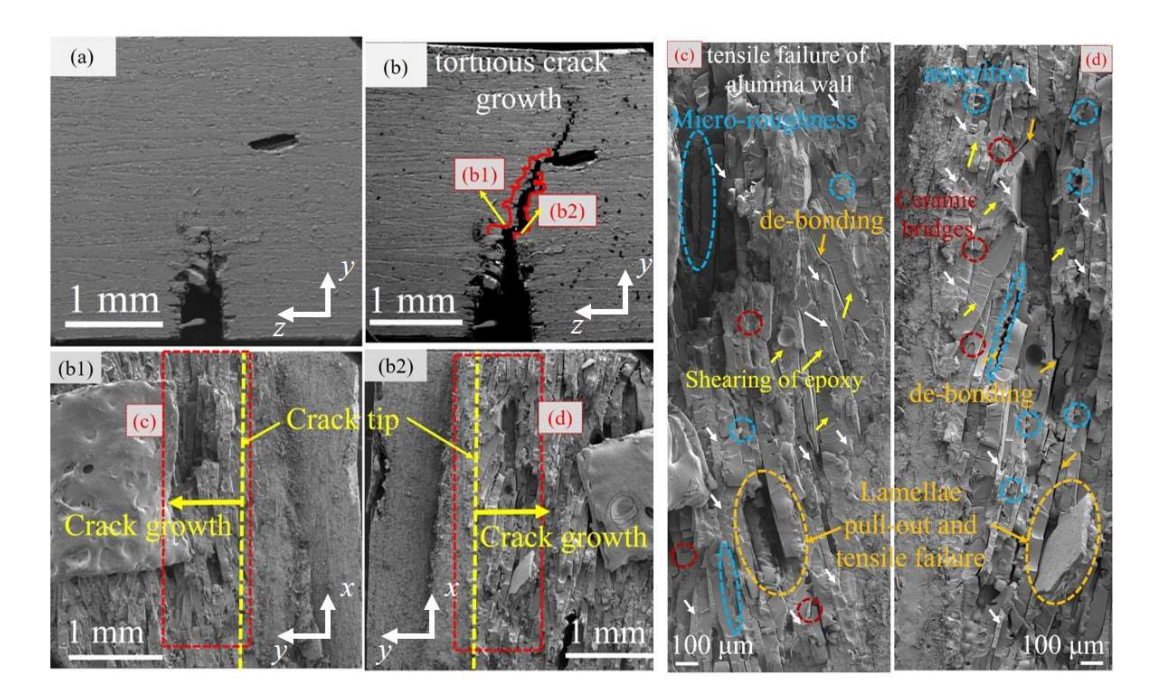


Fig. 4.9 (a) SEM of untested $\theta_{-}10$ SENB sample (b) Fractured SENB sample, showing tortuous crack paths (b1) left fractured surface, and (b2) right fractured Surface (c-d) magnified view of left and right fractured surfaces near the crack tip respectively.

It is important to note here that even though the pre-crack is perpendicular to lamellae, the lamellae orientation may vary across the volume of the scaffold. The experimentally prepared sample contains regions of varying lamellae orientations with short range order in Fig. 4.2 (b). The distribution in lamellae orientations influence the crack behaviour in these composites. Therefore, fracture tests are performed by varying the lamellae orientation with respect to pre-crack in Section 4.2.4.2 and Fig. 4.7 for a constant wedge angle case. The fractography of these samples is shown in Fig. 4.12 to Fig. 4.13. Fig. 4.12 (a-d), and Fig. 4.12 (e-h) show the SEM micrographs before and after the fracture tests on $\alpha 0$ and $\alpha 30$ samples. In case of $\alpha 0$, the pre-crack is oriented in the direction of the lamellae length and it grows along the alumina/epoxy interface with very limited deflection (Fig. 4.12 (b)). Consequently, the composite offers least resistance against the crack growth and

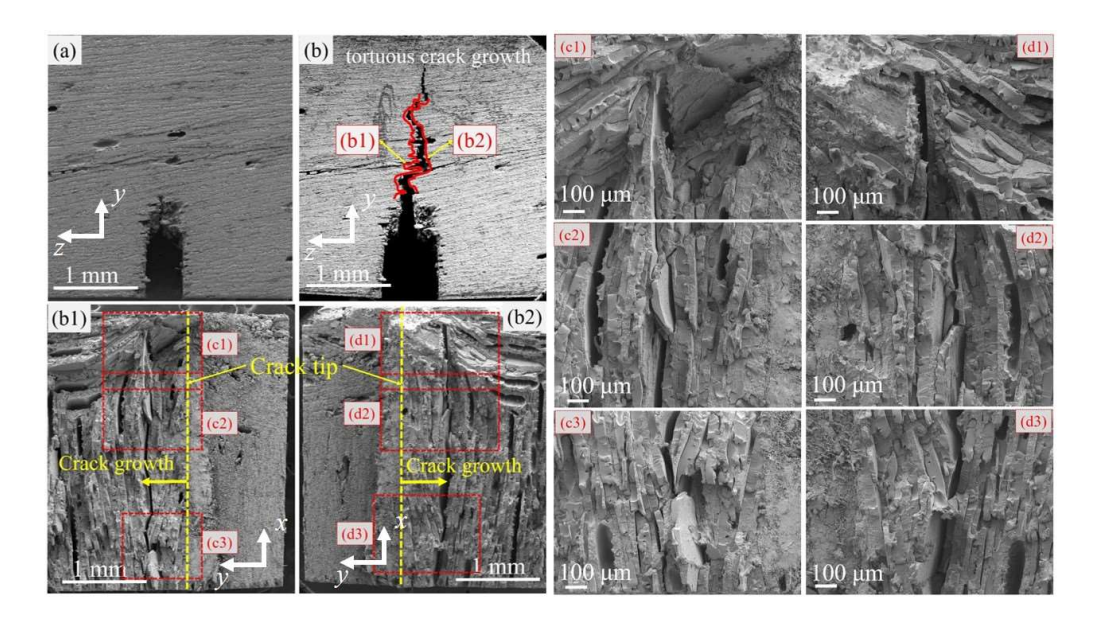


Fig. 4.10 (a) SEM of untested θ_5 SENB sample (b) Fractured SENB sample, showing tortuous crack paths (b1) left fractured surface, and (b2) right fractured Surface (c-d) magnified view of left and right fractured surfaces near the crack tip respectively.

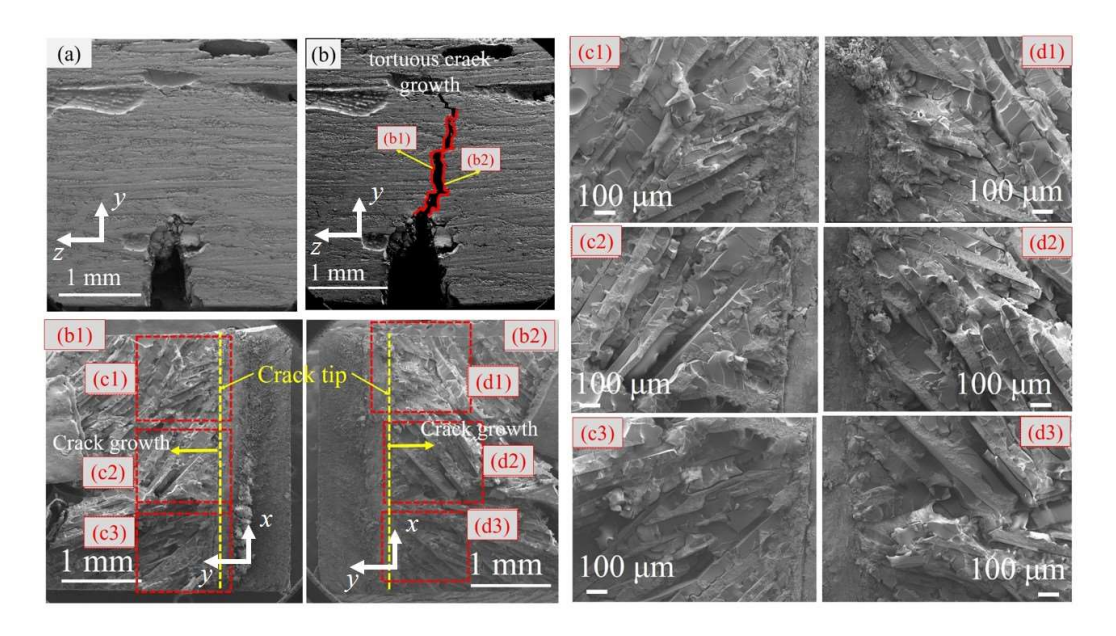


Fig. 4.11 (a) SEM of untested θ_2 0 SENB sample (b) Fractured SENB sample, showing tortuous crack paths (b1) left fractured surface, and (b2) right fractured Surface (c-d) magnified view of left and right fractured surfaces near the crack tip respectively.

shows minimum J_{min} and J_{max} in Fig. 4.7 (d). As the crack grows, few signatures of fractured lamellae and shearing of epoxy are observed in failed samples in Fig. 4.12 (c1-c3), and Fig. 4.12 (d1-d3). This contributes in stable crack growth and rising J_{R} curves for $\alpha 0$ sample in

Fig. 4.7 (a), and Fig. 4.7 (d) respectively. On increasing the crack orientation to 30° in Fig. 4.12 (e), a combination of inter- and cross-lamellar fracture is observed in Fig. 4.12 (f). The crack grows in a zig-zag manner through the alumina and epoxy phases in these samples. This requires higher energy for the crack to grow and leads to increase in fracture toughness of α 30 sample in comparison to the α 0 in Fig. 4.7 (d). Similar deformation and fracture behaviour with relatively larger crack deflections (more tortuous crack path) are also recorded in α 70 sample (Fig. 4.13) and α 90 samples (Fig. 4.9).

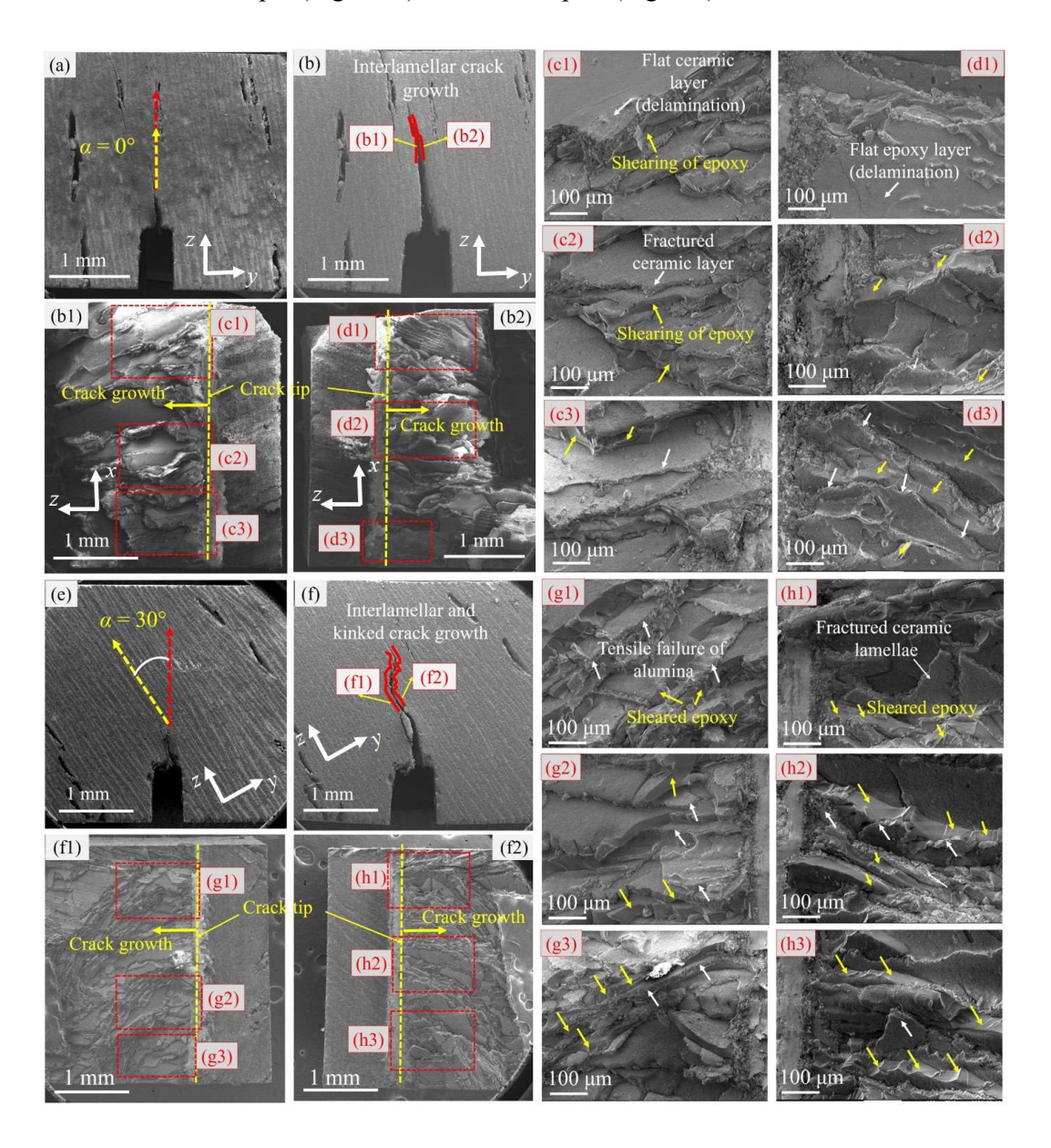


Fig. 4.12 (a, e) SEM of untested $\alpha 0$ and $\alpha 30$ and (b, f) respective fractured SENB sample, (b1, f1) left fractured surface, and (b2, f2) right fractured Surface (c1-c3 and d1-d3, g1-g3

and h1-h3) magnified view of left and right fractured surfaces near the crack tip for 0° and 30° crack oriented SENB sample respectively.

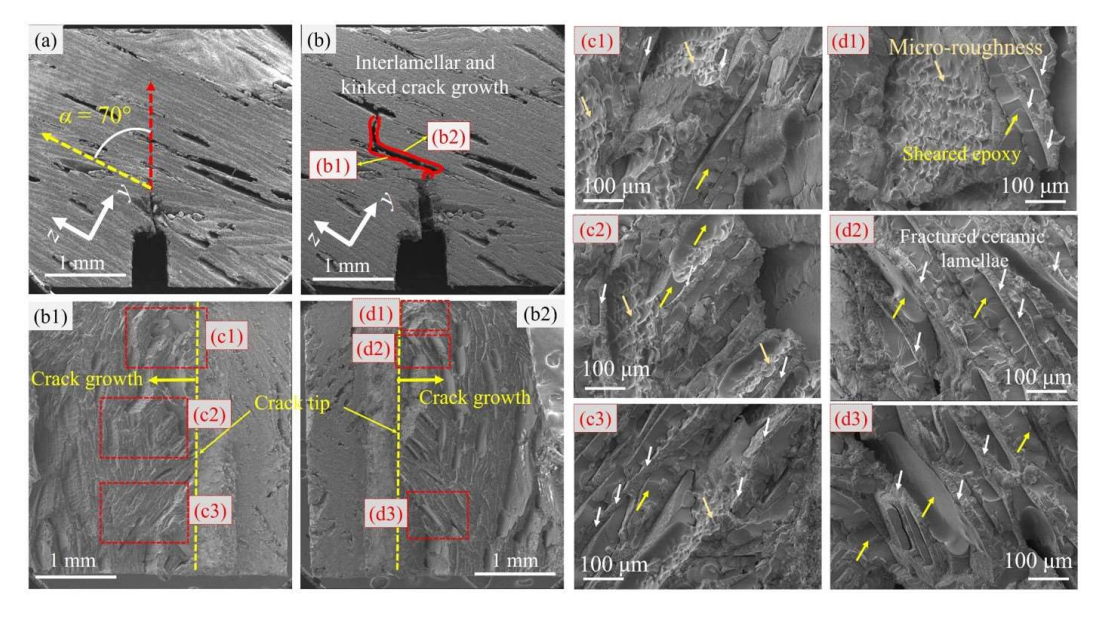


Fig. 4.13 (a) SEM of untested α 70 SENB sample (b) fractured SENB sample, (b1) left fractured surface, and (b2) right fractured Surface (c1-c3 and d1-d3) magnified view of left and right fractured surfaces near the crack tip respectively.

One may argue here that the phase present at the tip of pre-crack may influence the crack growth behaviour in lamellar composites containing alternate layers of hard and soft phase. However, it does not cause a significant difference and the average response remains similar due to the microstructural randomness and small thickness of each layer (25-60 μ m). Once crack growth initiates, it may encounter either hard ceramic phase, polymer phase, interface, or a combination of these. In such case, if crack interacts with hard layer causing its failure then the stress is transferred to the next soft layer through the interfacial shear stresses. These shear stresses cause local deformation and fracture within the polymer layer (Fig. 4.9 - 4.13)). This delays the fracture process and promotes stable crack growth as also reported in [35,36].

4.2.4.4 Finite element analysis

Based on the experimental results in Fig. (4.6 - 4.7), and fractography analysis presented in Fig. (4.9 - 4.13), it is observed that relatively thicker lamellae in $\theta_{-}10$ and $\theta_{-}20$ samples that are perpendicular to the crack induces higher tortuosity in the crack growth. However, the randomness in microstructure makes it difficult to accurately correlate the lamellae thickness and orientation to the crack behavior in alumina/epoxy lamellar composites. To

complement the experimental insights, XFEM based numerical simulations are performed to characterize the crack behavior as a function of microstructural parameters such as lamellae thickness (with varying alumina volume fraction, and at constant alumina volume fraction), and crack orientation (for t40 model only). Following the literature [37], the base numerical model ($t40 \text{ or } \alpha 90$) is calibrated to capture the experimental F-v response till the peak load. Here, the calibration refers to determine the elastic modulus and fracture energy of alumina phase only. The mechanical properties of epoxy phase are obtained experimentally. Determining the mechanical properties of alumina layer is difficult due to the complexities associated with the experimental conditions used in preparing alumina scaffolds and microstructural randomness. It is quite difficult to prepare alumina sample for bulk testing having exactly similar microstructure as in alumina/epoxy composites. The elastic modulus of alumina/epoxy composite is found to be ~18 GPa from Fig. 4.4 (a). The elastic modulus of epoxy obtained from nano-indentation tests is 1.94 GPa (Fig. 4.5), and Poisson's ratio as 0.3 [38]. The lower modulus may be associated with the chemistry of epoxy used in this work. Taking the alumina volume fraction as 40% (t40), the rule of mixtures predicts the elastic modulus of alumina phase ~ 41 GPa. However, this may be an overestimate [39] and modulus of alumina phase in composites may be lower due to the presence of voids and sintering conditions [11]. A trial and error approach by fitting the numerical and experimental F-v curves yields the elastic modulus and fracture energy of alumina around ~30 GPa and 0.16 N/mm respectively. The Poisson's ratio of alumina phase is taken as 0.21 [17]. The strength of epoxy and alumina phase is taken as 13.27 and 12.5 MPa respectively. The damage evolution parameter for epoxy and alumina are set to 0.2 and 0.16 N/mm respectively (Table 2.2). Based on $K_{\rm IC}$ of epoxy (0.64 MPa-m^{0.5}) [40], the fracture energy (K^2_{IC}/E) for damage evolution in epoxy is kept at ~ 0.2 N/mm.

To characterize the effect of lamellae thickness (or effect of ceramic volume fraction), the crack simulations are performed on numerical models having varying thickness of (20, 40 and 80 μ m) alumina layers. The total thickness of the model is kept constant at 3 mm. Expectedly, the peak load and stiffness increases with an increase in the thickness (or volume fraction) of alumina layer with the highest peak load and stiffness for t80 model as shown in Fig. 4.14 (a). This agrees well with the experimental data shown in Fig. 4.6 for different wedge angles. The alumina volume fraction increases with wedge angle θ (0 - 20°) in the range of 38 – 44 %. Fig. 4.14 (b-d) compares the maximum principal stress contours, and the crack paths for t20, t40, and t80 models. Multiple crack deflections and cross lamellar failure is seen in the model with largest alumina thickness (t80). On the other hand,

the crack grows relatively less tortuous for t20 model. Thus, in line with the experimental observations in Fig. (4.8 – 4.9), the crack tortuosity is higher for thicker alumina layer (or higher volume fraction of alumina phase). However, it may imply that the strength and crack tortuosity will keep on increasing with the thickness of alumina phase and eventually, the sample will have 100% alumina and no epoxy phase. This is contrary to the observations as natural nacre shows better combination of strength and toughness than 100% ceramic materials [1]. To understand this, XFEM simulations are performed for varying alumina lamellae thickness at a constant volume fraction $V_{\rm f}$ of 50%.

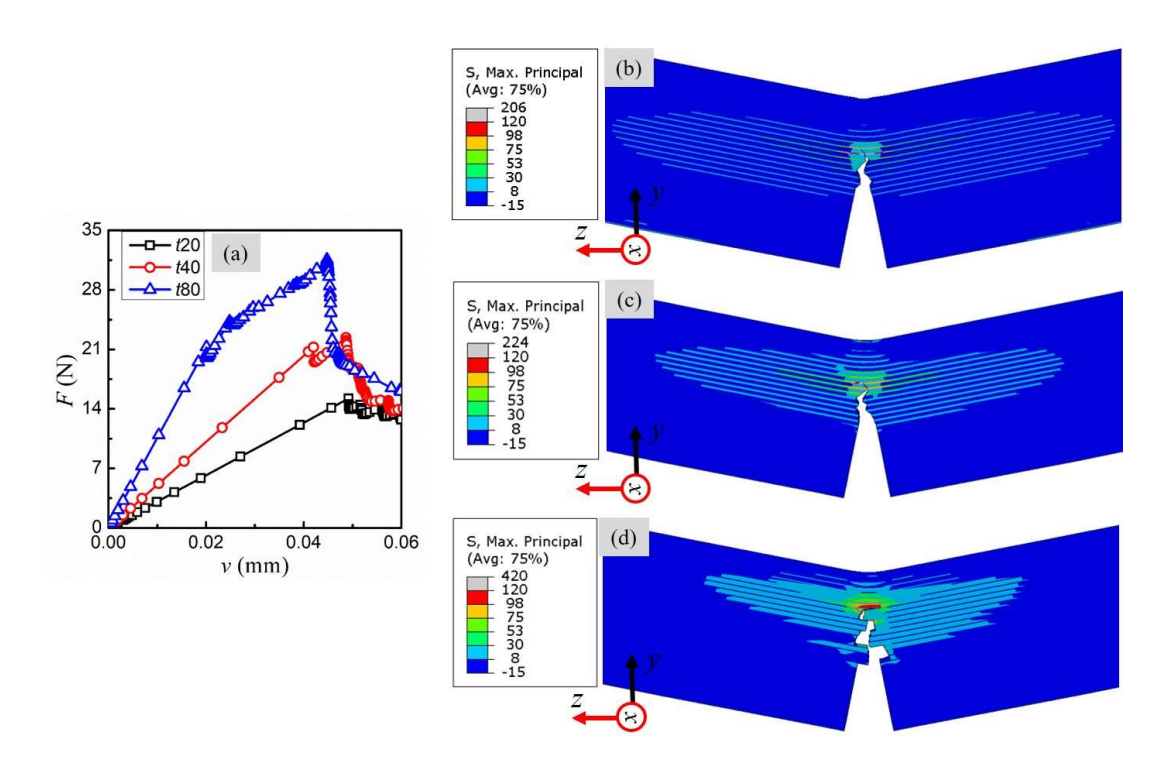
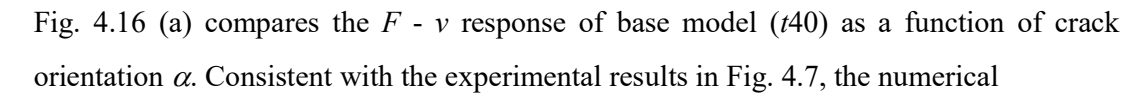


Fig. 4.14 (a) Computational F - v curves for varying lamellae thickness and maximum principal stress contour for (b) t20 (c) t40 (d) t80 numerical model.

Fig. 4.15 (a-e) compares the F-v response and maximum principal stress contours obtained from these simulations. The peak force is higher for the case of t50-50, and t75-75 in comparison to t25-25 and t100-100 models. Thus, the peak force does not increase gradually with the lamellae thickness and there seems to be an optimum lamellae thickness to fabricate stronger alumina/epoxy lamellar composites. The optimum lamellae thickness is found to be in the range of 50-75 microns for the parameters considered here. In line with the peak force, the crack tortuosity is higher for t50-50 model in Fig. 4.15 (f).



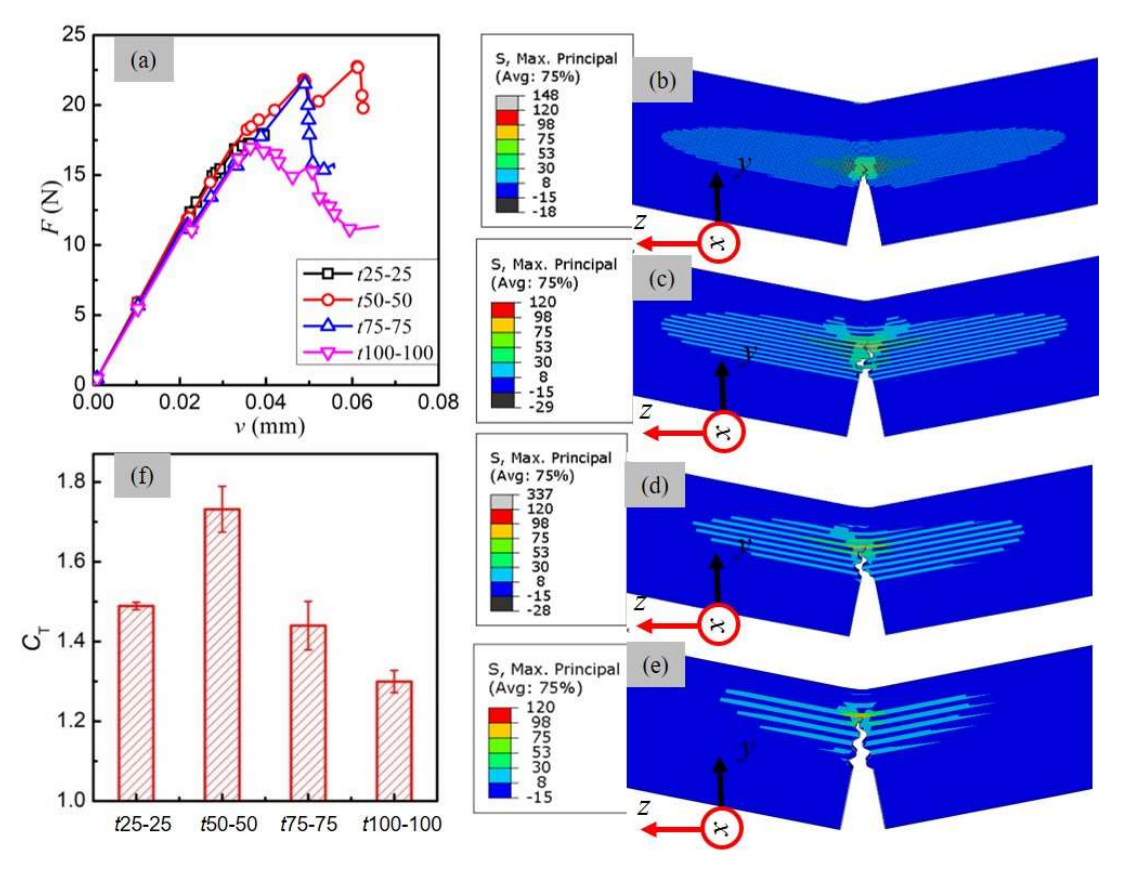


Fig. 4.15 (a) Computational F - v curves for varying lamellae thickness at a constant alumina volume fraction of 50%. (b-e) shows the corresponding maximum principal stress contour and crack path. Crack tortuosity from these simulations is compared in (f).

simulations predict the lowest peak load for 0° and highest load for 90° crack orientations. Moreover, the crack deflection increases as the crack orientation increases from 0° to 90° in Fig. 4.16 (b-e). For $\alpha 0$ model, the crack propagates along the alumina/epoxy interface showing the lowest resistance against the crack growth. In this case, the failure is dominated by the delamination and results in inter-lamellar fracture (please refer to Fig. 4.12 (a-d) and Fig. 4.16 (b-c)). On increasing the crack orientation to 30° , the fracture behaviour changes from delamination to mixed type failure *i.e.* combination of inter-lamellar and cross-lamellar fracture shown in Fig. 4.16 (d-e). This mixed fracture behaviour is due to the lamellae orientation and direction of the maximum principal stress within the lamellar composite. The crack propagation not only causes the inter-lamellar and cross-lamellar fracture but shows higher crack deflection for $\alpha 90$ sample in Fig. 4.16 (f-g). Consequently,

the peak load is maximum for the α 90 crack orientation. The peak load for α 30, α 70 are in between α 0 and α 90 samples. The crack bending at the initiation of crack growth in numerical simulations (Fig. 4.16 (b, d, and f)) is found to be similar as recorded in fracture experiments (Fig. 4.16 (c, e, and g)).

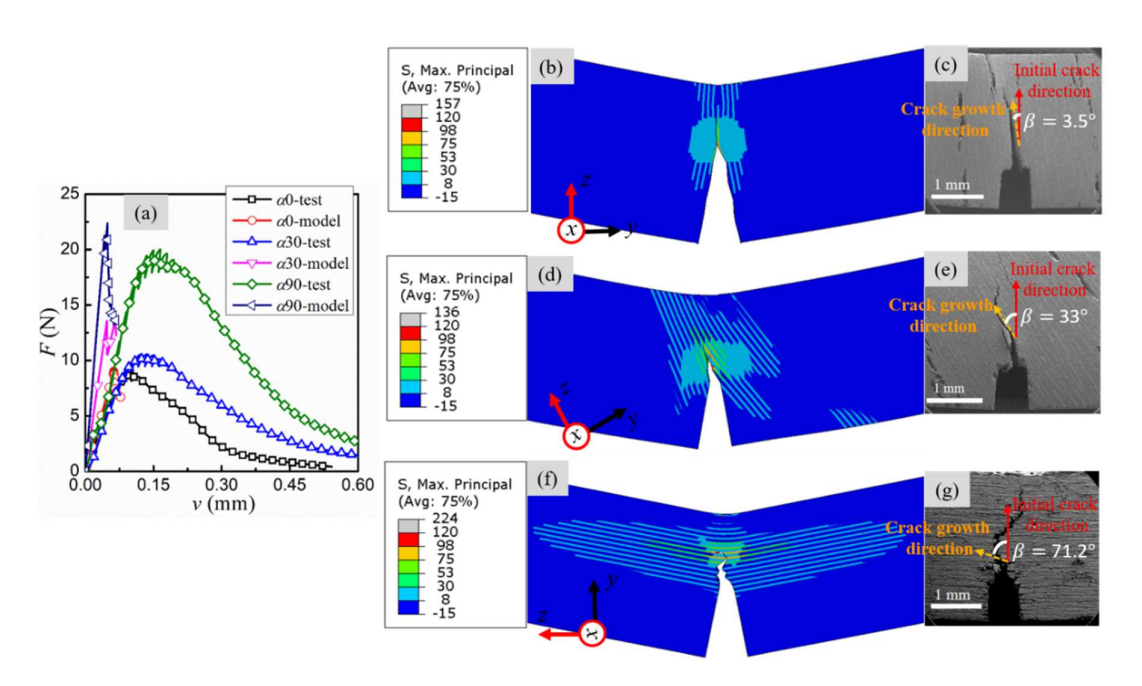


Fig. 4.16 (a) Comparison of experimental and computational F - v curves for varying crack orientations. Maximum principal stress contours and crack path including kink angle (β) for (b-c) α 0 (d-e) α 30 (f-g) α 90.

Even though, the numerical simulations accurately capture the key features of the crack behaviour in lamellar alumina/epoxy composites, the simulations predict higher stiffness and lower toughness (area under the F - v curve) than the experimental results. While the higher stiffness may be attributed to the perfect bonding assumed between the two phases in simulations, the lower toughness from simulation is due to the combination of various factors such as absence of microstructural randomness, ceramic bridges between the lamellae (see Fig. 4.2) and lamellae pull-out Fig. (4.8 - 4.11) mechanisms observed in experimental samples. Nonetheless, the simulations provide the key insights on crack behaviour in lamellar composites as a function of lamellae thickness, spacing and crack orientations. The numerical predictions also support the crack tortuosity and fracture mechanisms observed in fractography analysis of the failed samples.

4.3 Discussion

Rising J_R curves in fracture experiments imply stable crack growth in all types of lamellar composite coupons. The microstructural features in these samples differ in terms of lamellae thickness, spacing and distribution of lamellae orientations. The only common feature among them is their lamellar microstructure. Therefore, it is imperative to ask then what governs the crack propagation in these composites. These composites contain the layers of harder ceramic (alumina) and softer polymer (epoxy) phase. While the ceramic phase has negligible plasticity, the epoxy phase shows considerable plastic deformation ahead of the crack tip. The size of the plastic zone (r_p) is determined using the following relation (Eq. (4.3)),

$$r_{\rm p} = \frac{1}{2\pi} \frac{K_{\rm I}^2}{\sigma_{\rm v}^2} \tag{4.3}$$

Where, $K_{\rm I}$ is the applied stress intensity factor and $\sigma_{\rm y}$ is the yield strength of the composites.

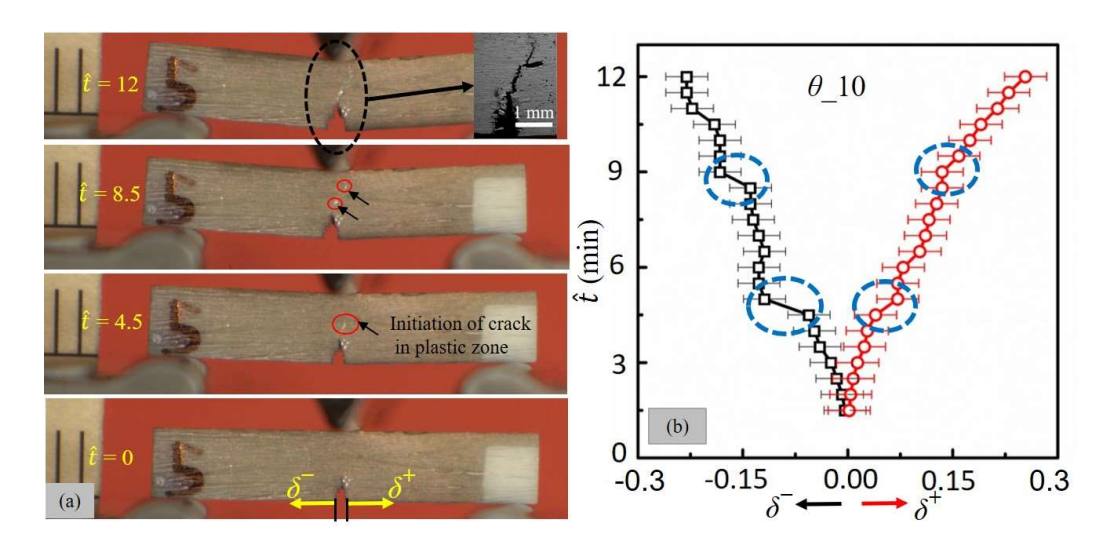


Fig. 4.17 (a) Optical images of SENB sample showing crack growth and (b) evolution of CMOD (δ - and δ +) at the crack mouth with time (\hat{t}) in θ 10 sample during SENB test.

The parameter, $K_{\rm I}$ is calculated from the experimental F-v data shown in Fig. (4.6 – 4.7) and summarised in Table 4.1. As the average yield/tensile strength ($\sigma_{\rm y}$) of all the composites 15 MPa, $r_{\rm p}$ lies in the range of 0.35 – 1 mm and 0.2 – 0.69 mm for varying wedge angle (θ) and crack orientation angle (α) respectively. This is much larger than the thickness of individual lamellae in each sample. Due to the large plastic zone size, the local stresses are expected to be distributed over a larger volume ahead of the crack tip. The tensile nature of these stresses may initiate multiple cracks in the weaker region as marked in Fig. 4.17 (a)

at time (\hat{t}) = 4.5 min in $\theta_{-}10$ sample (refer Fig. 4.6 (c)). As the crack propagates, the damage induced in nearby zone coalesce and results in final failure of the sample with multiple crack deflection and tortuosity (Fig. 4.17 (a) at time (\hat{t}) = 12 min). The multiple crack initiation leads to higher fracture toughness and increasing J_{R} curves. Both these parameters, crack deflection and multiple cracking, are influenced by the material microstructure and anisotropy in the sample. Therefore, they vary with the wedge angle (θ) and crack orientation (α) as recorded in the fracture experiments.

Sample type	$K_{\rm I}$ (MPa-m ^{0.5})	Sample type	$K_{\rm I}({\rm MPa\text{-}m^{0.5}})$
θ_0	1.02 ± 0.08	α0	0.54 ± 0.02
θ_5	0.7 ± 0.09	α30	0.63 ± 0.09
θ_10	0.99 ± 0.02	α70	0.84 ± 0.01
θ_20	1.27 ± 0.10	α90	0.99 ± 0.02

TABLE 4.1 Mode I stress intensity factors ($K_{\rm I}$) of different types of samples.

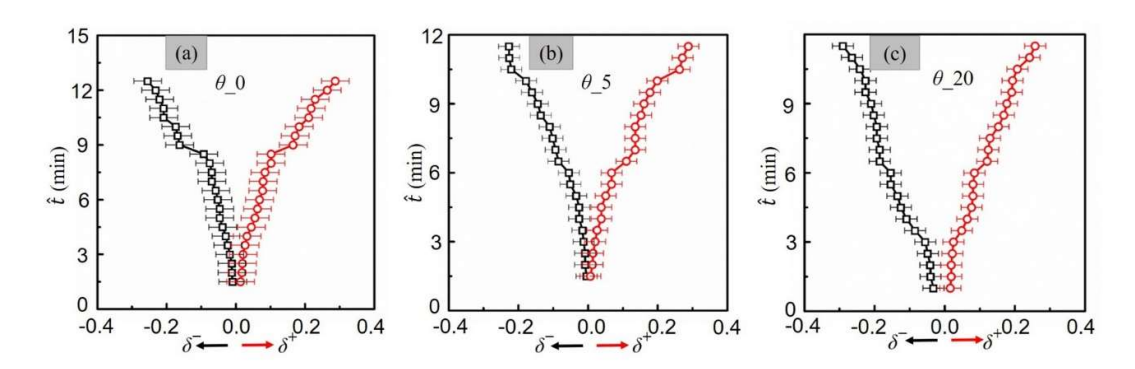


Fig. 4.18 CMOD measurement as δ and δ at the crack mouth with time for (a) θ_0 , (b) θ_5 , (c) θ_2 0.

The anisotropy in lamellae orientation and material properties also induces mode mixity in the cracks that are initiated from the main crack. This mode mixity is quantified through kinked crack theory proposed by Cottrell and Rice [41]. Accordingly, the local stress intensity factors $K_{\rm I}^{\rm k}$, and $K_{\rm II}^{\rm k}$ are calculated at the deflected crack tip using Eqs. (4.4 – 4.5) when main crack has just grown,

$$K_{\rm I}^{\rm k} = \frac{1}{4} (3\cos\frac{\beta}{2} + \cos\frac{3\beta}{2}) \times K_{\rm I} + O(\sqrt{a})$$
 (4.4)

$$K_{II}^{k} = \frac{1}{4} \left(\sin \frac{\beta}{2} + \sin \frac{3\beta}{2} \right) \times K_{I} + O(\sqrt{a})$$
 (4.5)

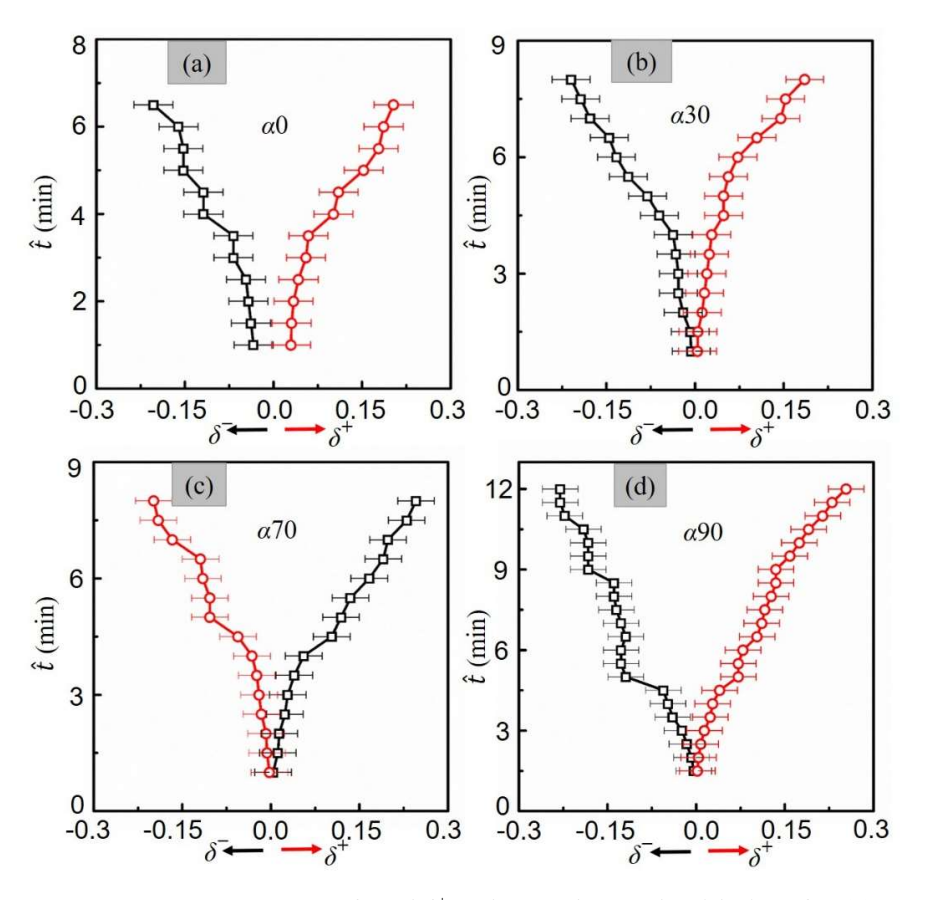


Fig. 4.19 CMOD measurement as δ and δ at the crack mouth with time for (a) α 0, (b) α 30, (c) α 70, and (d) α 90.

here, β is the kink angle of the crack as shown in the Fig. 4.20 (a-1) for θ_-0 . The kink angle as a function of crack orientation angles (α) is also marked in Fig. 4.16 (c, e, g). The angle β is measured at the tip of the crack when crack has just grown and experienced the first kink. Using the kink angle at the crack initiation and principal stress intensity factor (K_1) of the main crack, the mode mixity (K_1^k/K_1^k) is calculated for all the cases considered here. The mode mixity as a function of wedge angle θ (materials inhomogeneity) and crack orientation angles α (anisotropy) are shown in Fig. 4.20 (a, c). It reveals that thicker alumina lamellae induces higher mode mixity in θ_-10 and θ_-20 than in θ_-0 and θ_-5 samples. The higher mode mixity leads to improved fracture toughness for these samples recorded in Fig. 4.6. Thus, lamellae thickness plays a critical role in determining the resistance to crack growth in lamellar composites. The variation of K_1^k/K_1^k with the crack orientation is in accordance with the established theory of fracture mechanics in composites. The mode mixity increases as the crack orients perpendicular to the lamellae and same is observed in Fig. 4.7. Due to the distribution of lamellae orientation and lamellae

thickness, both these factors contribute to the fracture process in experimentally prepared samples.

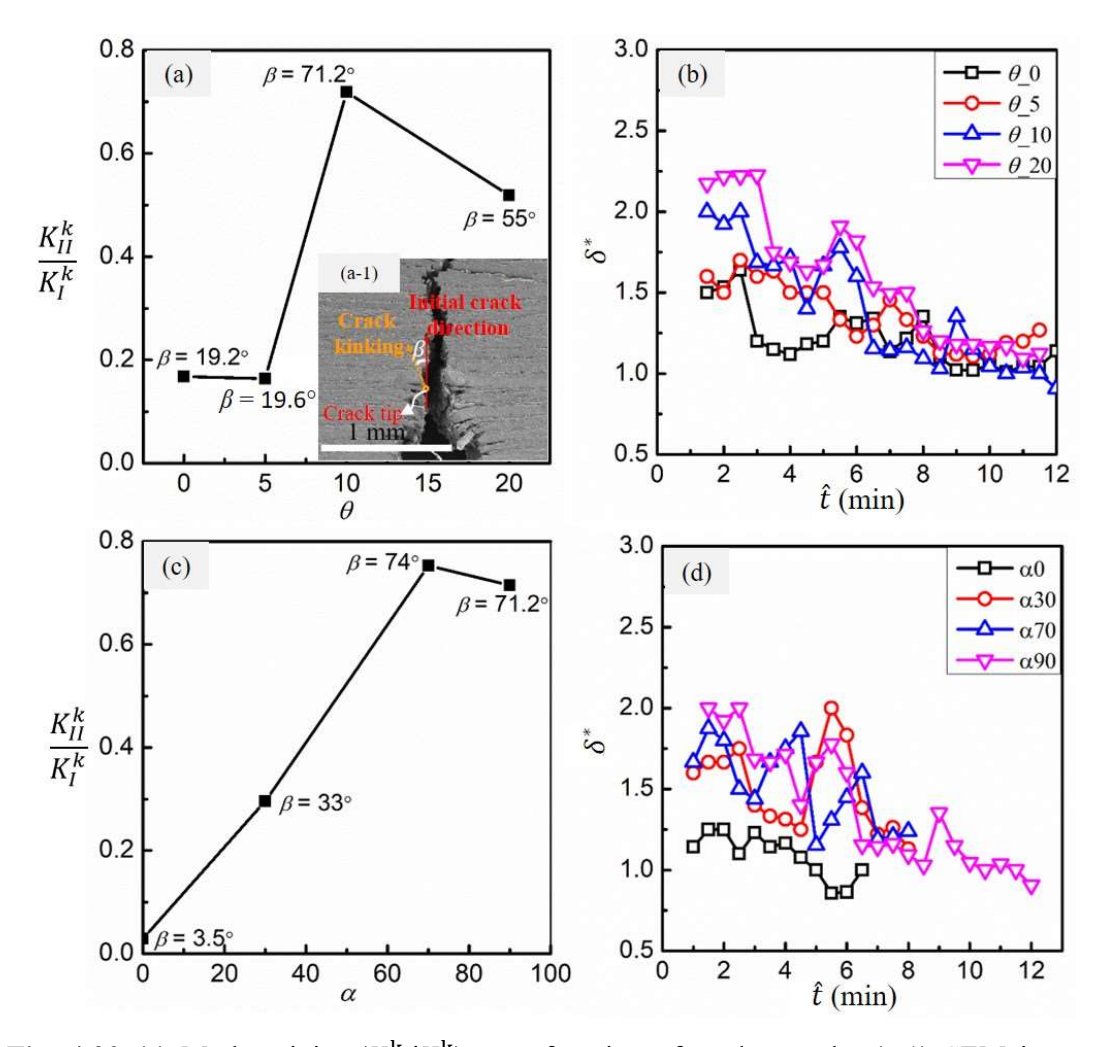


Fig. 4.20 (a) Mode mixity (K_{II}^k/K_I^k) as a function of wedge angle, (a-1) SEM image showing kink angle (β) for θ_0 sample as representative. (b) crack anisotropy $(\delta^* - \hat{t})$ as a function of wedge angle. (c) Mode mixity (K_{II}^k/K_I^k) , and (d) crack anisotropy $(\delta^* - \hat{t})$ as a function of crack orientation angle.

As discussed earlier that ASTM E1820 is the standard procedure to characterize the toughness of isotropic materials, it is extremely difficult to quantify the mode mixity in fracture experiments. Previously, some attempts have been made to characterize the mode mixity during crack growth [42,43]. Since, it is relatively easier to record the variation in crack mouth opening displacement (CMOD) during the crack propagation, a non-dimensional parameter $\delta^* = \max\{|\delta^+|, |\delta^-|\}/\min\{|\delta^+|, |\delta^-|\}$ is proposed here to

characterize the mode mixity in different types of lamellar composites. δ^+ and δ^- being the CMOD on the either side of the current location of the crack tip as schematically shown in Fig. 4.1. The δ^* will be unity for a self-similar crack growth in an isotropic homogenous material. The crack will not propagate in a self-similar manner in inhomogeneous and anisotropic material and δ^* will be greater than 1 due to the mode-mixity in such cases. Fig. 4.17 (b) shows the evolution of δ^+ and δ^- with time in the fracture testing of θ_- 10 sample. Expectedly, both the displacements gradually increase showing the crack opening with time. However, there are few locations, marked by dotted circle, that show sudden increase in δ^+ or δ^- . These points mark the crack deflection in the experimental sample. The two branches no longer remain symmetric and thus signify the deviation from the self-similar crack growth conditions. For a comparative analysis, the evolution of δ^+ and δ^- in various samples is compared in Fig. (4.18 - 4.19).

Fig. 4.20 (b) compares the δ^* with time in samples prepared with varying wedge angle (θ) (or increasing lamellae thickness in Fig. 4.2 (c)). At the starting of crack growth, the δ^* is relatively higher in θ 10 and θ 20 samples suggesting higher mode mixity and crack deflection in these samples. However, the δ^* approaches to 1 with time in all types of sample. It is consistent with the classical fracture mechanics theory. The angled crack always tries to align itself in pure mode I loading conditions to release more energy i.e. $K_{\rm II}$ = 0 criteria [41,42]. Thus, even though, crack initially feels the effect of material inhomogeneity and anisotropy in the lamellar composites, it eventually finds a path that allows it to grow in a self-similar manner under mode I loading conditions. A similar evolution of δ^* is recorded in samples having varying crack orientation in Fig. 4.20 (d). The initial δ^* is lower for the cracks that are aligned along the lamellae and it approaches to unity as the crack propagates across the thickness of the sample. Thus, the perpendicular crack in a sample having thicker lamellae will experience more severe crack deflections and will show larger deviation from the ideal self-similar crack growth conditions. Consequently, these types of sample will show higher fracture toughness. Fig. 4.20 (b) also suggest that the effect of lamellae thickness is stronger than the crack orientation due to higher initial δ^* in Fig. 4.20 (b) than in Fig. 4.20 (d).

The experimental and numerical analysis show that the variation in lamellae thickness and/or orientation induces varying degree of crack deflection. To quantify the deflection in crack path, crack tortuosity (C_T) is evaluated from SEM micrographs of all failed samples (see Fig. 4.8 - 4.13)) and compared in Fig. 4.21. C_T is defined as the ratio of the crack

contour length (S) to the straight unbroken ligament length in the pre-cracked specimen (S₀) [36]. While unbroken ligament length ahead of the pre-crack is known before the testing, the contour length of the crack is extracted from the micrographs of the failed sample using imageJ software. Fig. 4.21 compares the C_T for all the samples having varying lamellae thickness and crack orientations. Average value of 5 samples is used for comparison and the standard deviations among one type of samples is shown as error bars in Fig. 4.21. Consistent with the earlier observations, C_T is lowest for θ_0 samples (1.3 \pm 0.04) and increases with the increase in wedge angle (or lamellae thickness) with the maximum value of 1.7 \pm 0.08 for $\theta_{-}10$ samples with a slightly lower tortuosity (1.64 \pm 0.06) for θ 20 samples. On the other hand, the crack tortuosity gradually increases with crack orientation from 0 to 90° in Fig. 4.21 (b). The variation in crack tortuosity in numerical simulations is also in-line with the experimental measurements (see Fig. 4.14 -4.16). It is interesting to note that the lamellae thickness and crack tortuosity predicted by t50-50 numerical model are similar to θ_1 10 samples prepared experimentally. It suggests that 10° is the optimum wedge angle to fabricate alumina/epoxy lamellar composites using bi-directional freeze casting method. Higher C_T implies the longer crack paths and hence improved fracture toughness of the material. However, it is not the only parameter that determines the fracture toughness. Other toughening mechanisms such as shear deformation of matrix, de-bonding at interface, lamellae pull out, progressive fracture of lamellae (refer to Fig. (4.8 - 4.13)) contribute towards stable crack growth in alumina/epoxy lamellar composites.

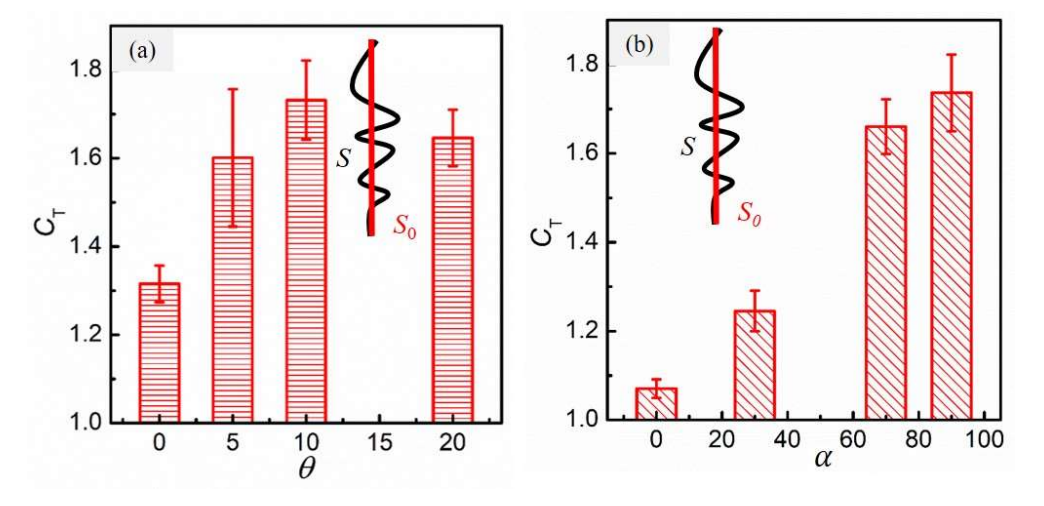


Fig. 4.21 Crack tortuosity as a function of (a) wedge angle and (b) crack orientation in lamellar composites.

The experimental results and numerical analysis suggest that both lamellae thickness and crack orientation with respect to lamellae influence the crack propagation and fracture response of the lamellar composites. In such composites, fracture initiates at the crack tip and proceeds with sequential deformation and failure of lamellae ahead of the main crack. The thicker alumina layer leads to larger crack deflections (crack tortuosity) and multiple cracking. The presence of softer epoxy between the alumina layers show large scale yielding and thus plays an important role in improving the fracture toughness and stable crack growth in the lamellar composites. Additionally, the lower mismatch (modulus ratio ~ 15) in the modulus of alumina and epoxy cause lower stress concentration across the interface and favors stress transfer from one phase to another phase [36].

The natural nacre contains about 95% hard phase (Aragonite) and 5% softer phase (biological protein) with a hierarchical microstructure [2]. Thus, the material composition as well their arrangements are important to achieve high strength and toughness. Currently, replicating the same in artificial materials is rather difficult due to the lack of suitable fabrication routes. However, the findings of the present study suggest that it is preferable to design lamellar composites with thicker hard layer and thinner soft layer to achieve higher strength and toughness.

4.4 Conclusions

Fracture testing on coupons fabricated with varying wedge angle (θ) and crack orientations (α) are performed to understand the crack behaviour in lamellar alumina/epoxy composites. The experimental results show rising J_R curves with increasing strength (F_{max}) and fracture toughness (J_{max}) for larger θ and α . The crack initiation, crack deflection and propagation mechanisms seem to depend on the lamellae thickness and crack orientation. Moreover, the tortuous crack path suggest that crack grows under mixed mode conditions in lamellar composites. Mode mixity (K_{II}^k/K_{I}^k) increases with the increase in the thickness of alumina layer (for θ _10, and θ _20 samples) or crack orientation angle (for α 70, and α 90 samples). The CMOD measurements based non-dimensional parameter δ^* shows similar variation and accurately captures the anisotropic crack propagation in lamellar composites. The higher anisotropy makes the crack path more tortuous and thus increases the fracture toughness of lamellar composites having thicker alumina phase (θ _10, θ _20) or higher crack orientations (α 70, and α 90). Moreover, there is an optimum alumina lamellae thickness (50 – 70 microns) to fabricate stronger and tougher alumina/epoxy lamellar

composites. Consequently, 10° is found to be the optimum PDMS wedge angle to achieve such microstructure in bi-directionally frozen sample. It is shown that the presence of softer phase plays an important in enhancing the strength and toughness of lamellar composites. The plastic zone in softer epoxy layer induces multiple cracking and spread the damage zone ahead of the crack tip and thus improves the fracture toughness and strength of alumina/epoxy composites. Finally, the present study provides a tool to design and analyse the strength and fracture toughness of lamellar composites by varying the PDMS wedge angle and monitoring δ^* .

4.5 References

- [1] U.G.K. Wegst, H. Bai, E. Saiz, A.P. Tomsia, R.O. Ritchie, Bioinspired structural materials, Nat. Mater. 14 (2015) 23–36. https://doi.org/10.1038/nmat4089.
- [2] M.A. Meyers, P.Y. Chen, A.Y.M. Lin, Y. Seki, Biological materials: Structure and mechanical properties, Prog. Mater. Sci. 53 (2008) 1–206. https://doi.org/10.1016/j.pmatsci.2007.05.002.
- [3] A.R. Studart, Towards high-performance bioinspired composites, Adv. Mater. 24 (2012) 5024–5044. https://doi.org/10.1002/adma.201201471.
- [4] R.O. Ritchie, The conflicts between strength and toughness, Nat. Mater. 10 (2011) 817–822. https://doi.org/10.1038/nmat3115.
- [5] F. Barthelat, H.D. Espinosa, An experimental investigation of deformation and fracture of nacre-mother of pearl, Exp. Mech. 47 (2007) 311–324. https://doi.org/10.1007/s11340-007-9040-1.
- [6] H.D. Espinosa, J.E. Rim, F. Barthelat, M.J. Buehler, Merger of structure and material in nacre and bone - Perspectives on de novo biomimetic materials, Prog. Mater. Sci. 54 (2009) 1059–1100. https://doi.org/10.1016/j.pmatsci.2009.05.001.
- [7] I. Corni, T.J. Harvey, J.A. Wharton, K.R. Stokes, F.C. Walsh, R.J.K. Wood, A review of experimental techniques to produce a nacre-like structure, Bioinspiration and Biomimetics 7 (2012). https://doi.org/10.1088/1748-3182/7/3/031001.
- [8] H. Bai, Y. Chen, B. Delattre, A.P. Tomsia, R.O. Ritchie, Bioinspired large-scale aligned porous materials assembled with dual temperature gradients, Sci. Adv. 1 (2015) 1–9. https://doi.org/10.1126/sciadv.1500849.
- [9] S. Algharaibeh, A.J. Ireland, B. Su, Bi-directional freeze casting of porous alumina ceramics: A study of the effects of different processing parameters on microstructure, J. Eur. Ceram. Soc. 39 (2019) 514–521.

- https://doi.org/10.1016/J.JEURCERAMSOC.2018.09.030.
- [10] W. Gao, M. Wang, H. Bai, A review of multifunctional nacre-mimetic materials based on bidirectional freeze casting, J. Mech. Behav. Biomed. Mater. 109 (2020) 103820. https://doi.org/10.1016/j.jmbbm.2020.103820.
- [11] S.N. Tiwari, P.K. Agnihotri, Effect of freezing conditions on the microstructure and compressive response of alumina/epoxy nacre-type composites, Mater. Today Commun. 37 (2023) 107470. https://doi.org/10.1016/j.mtcomm.2023.107470.
- [12] E. Munch, M.E. Launey, D.H. Alsem, E. Saiz, A.P. Tomsia, R.O. Ritchie, Tough, bio-inspired hybrid materials, Science (80-.). 322 (2008) 1516–1520. https://doi.org/10.1126/science.1164865.
- [13] M.E. Launey, E. Munch, D.H. Alsem, H.B. Barth, E. Saiz, A.P. Tomsia, R.O. Ritchie, Designing highly toughened hybrid composites through nature-inspired hierarchical complexity, Acta Mater. 57 (2009) 2919–2932. https://doi.org/10.1016/j.actamat.2009.03.003.
- [14] T.P. Niebel, F. Bouville, D. Kokkinis, A.R. Studart, Role of the polymer phase in the mechanics of nacre-like composites, J. Mech. Phys. Solids 96 (2016) 133–146. https://doi.org/10.1016/j.jmps.2016.06.011.
- [15] M. Grossman, F. Bouville, F. Erni, K. Masania, R. Libanori, A.R. Studart, Mineral Nano-Interconnectivity Stiffens and Toughens Nacre-like Composite Materials, Adv. Mater. 29 (2017). https://doi.org/10.1002/adma.201605039.
- [16] L. Cheng, M. Sun, F. Ye, Y. Bai, M. Li, S. Fan, L. Zhang, Structure design, fabrication, properties of laminated ceramics: A review, Int. J. Light. Mater. Manuf. 1 (2018) 126–141. https://doi.org/10.1016/j.ijlmm.2018.08.002.
- [17] V. Vilchez, P.I.B.G.B. Pelissari, V.C. Pandolfelli, F. Bouville, Mixed-mode fracture model to quantify local toughness in nacre-like alumina, J. Eur. Ceram. Soc. 43 (2023) 4472–4481. https://doi.org/10.1016/j.jeurceramsoc.2023.03.044.
- [18] J. Liu, R. Bai, Z. Lei, C. Xu, Q. Ye, W. Martens, P.K. Yarlagadda, C. Yan, Experimental and numerical investigation of the toughening mechanisms in bioinspired composites prepared by freeze casting, Compos. Sci. Technol. 182 (2019) 107768. https://doi.org/10.1016/j.compscitech.2019.107768.
- [19] F. Bouville, Strong and tough nacre-like aluminas: Process-structure-performance relationships and position within the nacre-inspired composite landscape, J. Mater. Res. 35 (2020) 1076–1094. https://doi.org/10.1557/jmr.2019.418.
- [20] P. Fratzl, H.S. Gupta, F.D. Fischer, O. Kolednik, Hindered crack propagation in

- materials with periodically varying young's modulus Lessons from biological materials, Adv. Mater. 19 (2007) 2657–2661. https://doi.org/10.1002/adma.200602394.
- [21] H.C. Cao, A.G. Evans, On crack extension in ductile/brittle laminates, Acta metall. mater. 39 (1991) 2997–3005.
- [22] Y. Wang, Q. Liu, Z.F. Lan, B. Zhang, H.Q. Zhang, J.W. Liu, F. Ye, Strong and tough bioinspired nacre-like B4C/Al functionally graded materials with eliminated abrupt interfaces, Compos. Commun. 25 (2021) 100741. https://doi.org/10.1016/j.coco.2021.100741.
- [23] E. Poloni, F. Bouville, C.H. Dreimol, T.P. Niebel, T. Weber, A.R. Biedermann, A.M. Hirt, A.R. Studart, Tough metal-ceramic composites with multifunctional nacre-like architecture, Sci. Rep. 11 (2021) 1–12. https://doi.org/10.1038/s41598-021-81068-z.
- [24] F. Bouville, E. Maire, S. Meille, B. Van De Moortèle, A.J. Stevenson, S. Deville, Strong, tough and stiff bioinspired ceramics from brittle constituents, Nat. Mater. 13 (2014) 508–514. https://doi.org/10.1038/nmat3915.
- [25] A. Doitrand, R. Henry, H. Saad, S. Deville, S. Meille, Determination of interface fracture properties by micro- and macro-scale experiments in nacre-like alumina, J. Mech. Phys. Solids 145 (2020). https://doi.org/10.1016/j.jmps.2020.104143.
- [26] T. Duminy, R. Henry, J. Adrien, A. Doitrand, S. Meille, Anisotropic fracture in nacre-like alumina. Theor. Appl. Fract. Mech. 123 (2023) 103710. https://doi.org/10.1016/j.tafmec.2022.103710.
- [27] K. Kang, Y. Chen, J. Hou, Y. Liu, Fracture behaviors of nacre-like composites via phase-field fracture modeling, Eng. Fract. Mech. 296 (2024) 109837. https://doi.org/10.1016/j.engfracmech.2023.109837.
- [28] ASTM E1820 18, Standard Test Method for Measurement of Fracture Toughness, ASTM International, 2018.
- [29] ASTM C1421-18, Standard Test Methods Determination of Fracture Toughness of Advanced Ceramics at Ambient Temperature, ASTM International, 2018.
- [30] L. Pan, S. Lu, X. Xiao, Z. He, C. Zeng, J. Gao, J. Yu, Enhanced mechanical and thermal properties of epoxy with hyperbranched polyester grafted perylene diimide, RSC Adv. 5 (2015) 3177–3186. https://doi.org/10.1039/c4ra13609h.
- [31] A. Saxena, Nonlinear Fracture Mechanics for Engineers, CRC Press, Boca Raton, Florida, 1998.

- [32] F. Zok, C.L. Hom, Large scale bridging in brittle matrix composites, Acta Metall. Mater. 38 (1990) 1895–1904. https://doi.org/10.1016/0956-7151(90)90301-V.
- [33] J.D. Currey, Mechanical properties of mother of pearl in tension, Proc. R. Soc. London Biol. Sci. 196 (1977) 443–463. https://doi.org/10.1098/rspb.1977.0050.
- [34] G. Tan, J. Zhang, L. Zheng, D. Jiao, Z. Liu, Z. Zhang, R.O. Ritchie, Nature-Inspired Nacre-Like Composites Combining Human Tooth-Matching Elasticity and Hardness with Exceptional Damage Tolerance, Adv. Mater. 31 (2019) 1–9.
- [35] M. Grossman, D. Pivovarov, F. Bouville, C. Dransfeld, K. Masania, A.R. Studart, Hierarchical toughening of nacre-like composites, Adv. Funct. Mater. 29 (2019) 1806800.
- [36] T. Magrini, A. Senol, R. Style, F. Bouville, A.R. Studart, Fracture of hierarchical multi-layered bioinspired composites, J. Mech. Phys. Solids 159 (2022). https://doi.org/10.1016/j.jmps.2021.104750.
- [37] J. Li, S. Yang, D. Li, V. Chalivendra, Numerical and experimental studies of additively manufactured polymers for enhanced fracture properties, Eng. Fract. Mech. 204 (2018) 557–569. https://doi.org/10.1016/j.engfracmech.2018.11.001.
- [38] H.S. Bedi, M. Tiwari, P.K. Agnihotri, Quantitative determination of size and properties of interphase in carbon nanotube based multiscale composites, Carbon N. Y. 132 (2018) 181–190.
- [39] W. Yu, Common Misconceptions on Rules of Mixtures for Predicting Elastic Properties of Composites, AIAA J. 62 (2024) 1982–1987.
- [40] N. Domun, H. Hadavinia, T. Zhang, T. Sainsbury, G.H. Liaghat, S. Vahid, Improving the fracture toughness and the strength of epoxy using nanomaterials-a review of the current status, Nanoscale 7 (2015) 10294–10329. https://doi.org/10.1039/c5nr01354b.
- [41] B. Cotterell, J. Rice, Slightly curved or kinked cracks, Int. J. Fract. 16 (1980) 155– 169. https://doi.org/10.1007/BF00012619.
- [42] M.T. Tilbrook, R.J. Moon, M. Hoffman, Crack propagation in graded composites, Compos. Sci. Technol. 65 (2005) 201–220. https://doi.org/10.1016/j.compscitech.2004.07.004.
- [43] M.T. Tilbrook, K. Rozenburg, E.D. Steffler, L. Rutgers, M. Hoffman, Crack propagation paths in layered, graded composites, Compos. Part B Eng. 37 (2006) 490–498. https://doi.org/10.1016/j.compositesb.2006.02.012.

CHAPTER 5: Comparison of crack behavior in lamellar and brick-mortar alumina/epoxy composites

In the previous Chapter, it is observed that crack behavior in terms of crack initiation and crack growth, mainly depends on the lamellae thickness and crack orientation with respect to the lamellae. In lamellar composites, crack grows under mixed mode condition, and mode mixity (K_{II}^k/K_{I}^k) increases with the increase in the thickness of alumina layer or crack orientation angle. The higher mode mixity makes the crack path more tortuous and thus increases the fracture toughness of lamellar composites having thicker alumina phase or higher crack orientations. These observation leads to an obvious question that how these mechanisms will differ in brick – mortar kind of microstructure. To this end, the lamellar alumina scaffolds fabricated using bi-directional freeze casting ($\theta = 10^{\circ}$) are infiltrated with sacrificial wax, followed by uniaxial pressing at 40 MPa, and 80 °C to get brick-like alumina scaffolds. After re-sintering of brick-like alumina scaffolds, epoxy is infiltrated to get brickmortar alumina/epoxy composites. The flexure tests are carried out to determine the strength of lamellar/brick-mortar composites. The fracture toughness measurements are performed on SENB specimens in three-point bend configuration. The effect of microstructural features such as ceramic lamellae/brick thickness, thickness of the polymer phase, and volume fraction of lamellae/brick on the strength and fracture toughness of lamellar and brick-mortar alumina/epoxy composites have been investigated. By combining microstructural features obtained through the image analysis of lamellar/brickmortar composites, an analytical model based on shear lag theory is put forward to complement the experimental findings in this Chapter.

5.1 Introduction

Developing stronger and tougher lightweight structural materials for diverse applications including protective systems, building structures to transportation or energy is a demanding challenge [1–3]. Although, both these properties of strength and toughness are mutually exclusive [4], nacre (inner layer of mollusc shell) provides a source of inspiration to address this problem in synthetic composites. However, it will depend on our understanding of the material's architecture at various length scales present in the nacre and its relation to the mechanical response under varying loading conditions. Furthermore, it becomes essential to develop a suitable fabrication technique to mimic such architecture in synthetic

composites at bulk scale. Even though, nacre consists of brittle ceramics (95 wt%) and biological proteins (5 wt%), its fracture toughness is 1000 times higher than its major constituent *i.e.* aragonite [1,5]. Thus, the idea of exploring such natural architecture design with multiple materials combination in synthetic composites is being explored since a few decades[6–14]. The complex structure of natural materials evolves using controlled self-assembly of building blocks through 'bottom up' approach [2]. Many efforts have been made using multitude of fabrications techniques to fabricate artificial nacreous composites[15]. Among these, the bi-directional freeze casting technique emerges as most promising method due to its ability to mimic several microstructural features of the natural nacre[16–18]. Using the freeze casting technique, the fabricated nacre-like composites using hard (ceramic) and soft (polymer) phase show strength and toughness of ~100 MPa, 2 kJ-m⁻² for hydroxyapatite/PMMA[6], and ~175 MPa, 1 - 2 kJ-m⁻² for zirconia/ dental resin[19].

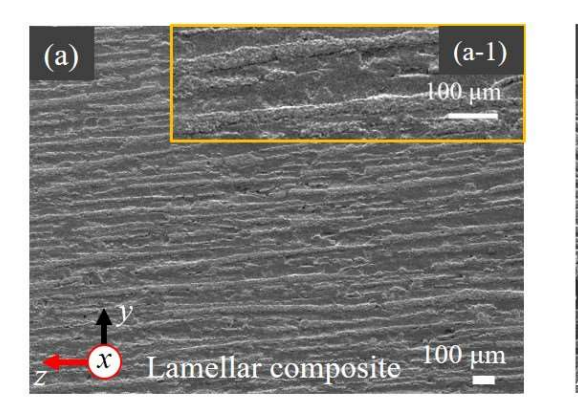
Analytical models and experimental studies provide insightful guidelines to design nacreous composites for optimal stiffness, strength and toughness [20-28]. For example, the size of the inclusions/bricks should be small for the higher strength [20,29]. The aspect ratio of the inclusion should be large for higher performance [30,31]. The asperities over the bricks enhance the interaction between the bricks and mortar i.e. increasing area fraction of the asperities enhances the strength [31,32]. The overlap length between the bricks should be large for high strength, stiffness, and toughness, but it should be under limit, a constrained imposed due to fracture of the bricks [33–35]. The optimum overlap length is linked to the length of cohesive zone at the interface [36] and maximum strain energy density [37]. The quantitative measurement between mechanical properties of the constituent, composite architecture, and the macroscopic mechanical response are crucial for the development of synthetic composites for optimal strength and toughness. Notably, the microstructural parameters such as thickness of lamellae/brick, polymer phase, and volume fraction of hard/soft phase, ceramic bridges/pillars between the hard phase, asperities, overlap length, aspect ratio of the overlap length influence the strength and toughness of biological composites[20,26,28,38]. Among these, the lamellae/polymer thickness and overlap length seems to critically affect the strength and toughness of brickmortar like composites [37,39]. Understanding the influence of lamellae/polymer thickness and overlap length in lamellar/brick-mortar composites is still immature i.e. How lamellae/polymer thickness and overlap length influence the deformation and failure

mechanisms of the composites if the microstructure is converted from lamellar to brick-mortar composites? This is the prime objective of the present work.

To this end, nacre-like lamellar and brick-mortar alumina/epoxy composites are fabricated using bi-directional freeze casting method. The flexure and fracture tests are performed to determine the strength and fracture toughness of the prepared lamellar and brick-mortar composites. The role of microstructural features such as thickness of ceramic lamellae/brick, thickness of the polymer phase, and volume fraction of ceramic lamellae/brick on the strength and fracture toughness of lamellar and brick-mortar composites have been investigated. We then use shear lag analysis to estimate the distribution of axial stress in the lamellae/brick, and shear stresses in the polymer phase as a function of overlap length. This analysis helps us to determine the optimum overlap length at which elastic strain energy density is maximized *i.e.* composite offers highest resistance to damage initiation and the evolution of crack path during the crack growth.

5.2 Results

5.2.1 Microstructural features of lamellar and brick-mortar composites



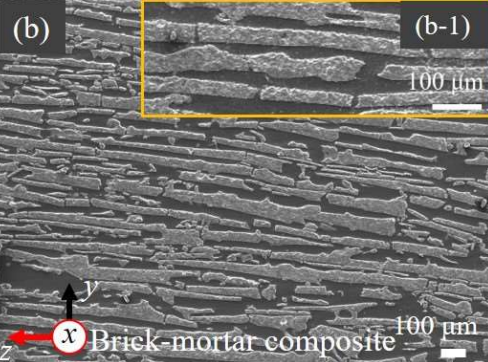


Fig. 5.1 (a - a1) SEM micrographs of lamellar alumina/epoxy composites (b - b1) SEM micrographs of brick-mortar alumina/epoxy composite.

Fig. 5.1 ((a - a1) - (b - b1)) shows the SEM micrographs of the fabricated lamellar and brick-mortar alumina/epoxy composites. A representative SEM micrograph shown in the Fig. 5.2 (a) represents the microstructural features such as ceramic lamellae thickness (t), thickness of polymer phase (λ), length of the brick (L), and overlap length (L0) in B-M composites. Both the thickness of ceramic lamellae and epoxy phase is comparatively higher for lamellar composites than brick-mortar composites shown in Fig. 5.2 (b). Due to the hot pressing of lamellar scaffolds at 40 MPa and subsequent re-sintering at 1450°C and

1600°C, the average thickness of the lamellae decreases by 5 to 10 μm. However, there is considerable decrease in average polymer thickness from 60 μm for lamellar composite to 18 - 20 μm for brick-mortar composites (see Fig. 5.2 (b)). The decrement in the lamellae thickness of ceramic and polymer phase of lamellar materials is primarily due to the hot pressing and re-sintering at higher temperature [39].

Due to highly aligned and approximately parallel ceramic layers in lamellar composites (Chapter 4, Fig. 4.3), both the average length and overlap length of the lamellae can be assumed to be same and the measured average value is 2000 μ m. However, the brick length in brick-mortar composites ranges from 44 \pm 17 μ m to 1022 \pm 341 μ m with an average value of 408 \pm 284 μ m. Similarly, the overlap length in brick-mortar composites ranges from 20 \pm 5 μ m to 260 \pm 94 μ m with an average value of 130 \pm 97 μ m. The above-mentioned microstructural features represent average value from the SEM micrograph, however there are regions in the sample where some of the features such as lamellae and polymer thickness are in sub-micrometer range (Fig. 5.1 (a - b)).

Burnout tests reveal that the ceramic content of lamellar materials increases with hot pressing and subsequent sintering. The average ceramic wt% for 1450-L, 1450-BMC, and 1600-BMC composites are found to 62%, 70%, and 78% respectively.

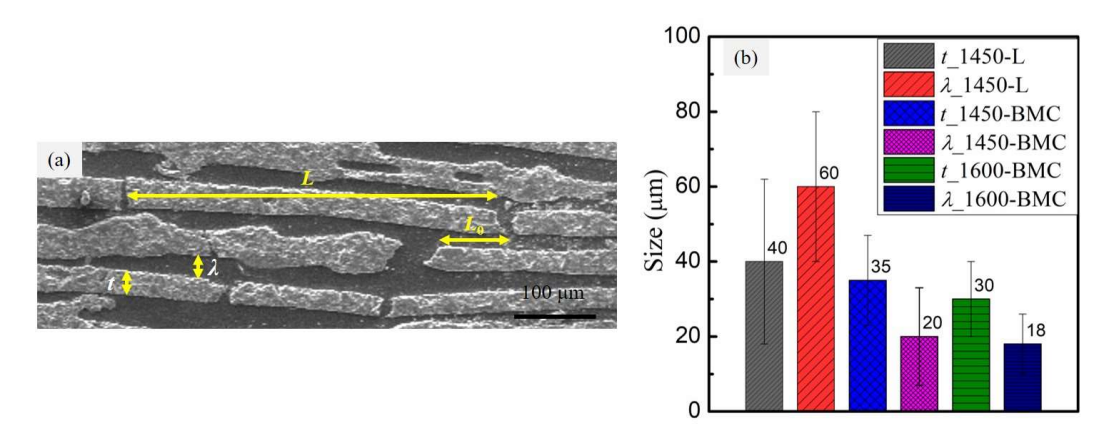


Fig. 5.2 (a) Representative SEM micrograph of 1450-BMC showing the definition of microstructural features (b) average thickness of alumina phase (t) and epoxy phase (λ) in lamellar and brick-mortar composites.

5.2.2 Bending stress – strain curve behavior

Bending stress (σ_{flexural}) – strain (ε) curves of alumina/epoxy composites with lamellar and brick-mortar structures are shown in Fig. 5.3 (a). The ultimate flexure strength of these composites is summarized in Fig. 5.3 (b). The flexure strength is minimum for lamellar

composites and higher for brick-mortar composites. Further, the strength of 1600-BMC sample is higher than 1450-BMC composite samples. Both the 1450-BMC, and 1600-BMC composites differ from the 1450-L composites in terms of structure, composition, and additional pressing and sintering processing steps. The additional processing steps accounts for the conversion of longer lamellae into relatively smaller bricks (Fig. 5.1 (a - b)), refinement of the lamellae/polymer thickness (Fig. 5.2 (b)) and increase in ceramic wt% (62% to 78%). The increased strength of brick-mortar composite may be due to the refinement of the lamellae thickness and increased ceramic wt% from 62% to 78%. A similar experimental observation has been reported by Launey et al. [39] that the probability of the presence of large size flaws is higher in the sample with thicker lamellae representing large sampling volume, and hence such flaws greatly influence the strength of the composites.

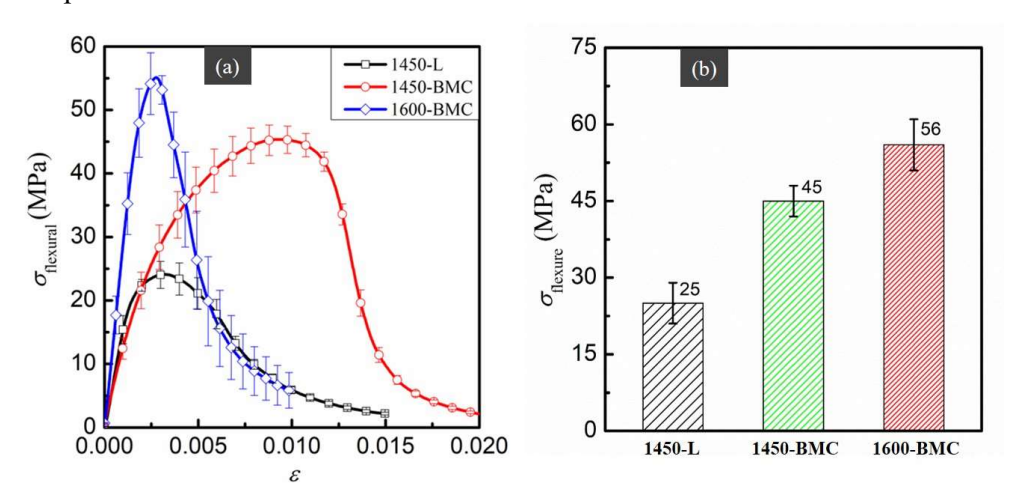


Fig. 5.3 (a) Bending stress – strain curves of lamellar and brick-mortar composites. (b) The ultimate flexure strength of 1450-L, 1450-BMC, and 1600-BMC composite samples.

5.2.3 Crack resistance curve behavior

The recorded F-v curves shown in Fig. 5.4 (a) are analysed to measure the crack resistance curves $(J - \Delta a)$. The measured $J - \Delta a$ curve for lamellar and brick-mortar composite specimens are shown in Fig. 5.4 (b). Following the ASTM standard [40], the maximum J_{max} , or J_c value are limited by $J_{\text{max}} \leq B\sigma_y/25$, or (w- $a)\sigma_y/25$, and maximum allowed crack growth $\Delta a_{\text{max}} \leq 0.25(w - a)$. Based on the SENB test results satisfying the condition of J-dominance, the J_c for lamellar and brick-mortar composites are marked in the Fig. 5.4 (b) with cyan colour dots. The J_c for 1450-L composite specimens (~2.3 kJ-m⁻²) is slightly higher than 1450-BMC specimens (~2.16 kJ-m⁻²). The J_c for 1600-BMC specimens (~1.68

kJ-m⁻²) is lowest among the all sample type. Moreover, it is apparent that both the lamellar and brick-mortar composites show rising J - Δa curve. The nature of all the F-v curves shown in Fig. 5.4 (a) is bell shaped, a typical sign of stable crack propagation [5]. As a result, both the lamellar and brick-mortar composites show rising J - Δa curve (Fig. 5.4 (b)). The rising J - Δa curve clearly indicates the presence of multiple toughening mechanisms during the crack growth. The crack behavior in both type of composites is qualitatively similar, and it is discussed in the next section.

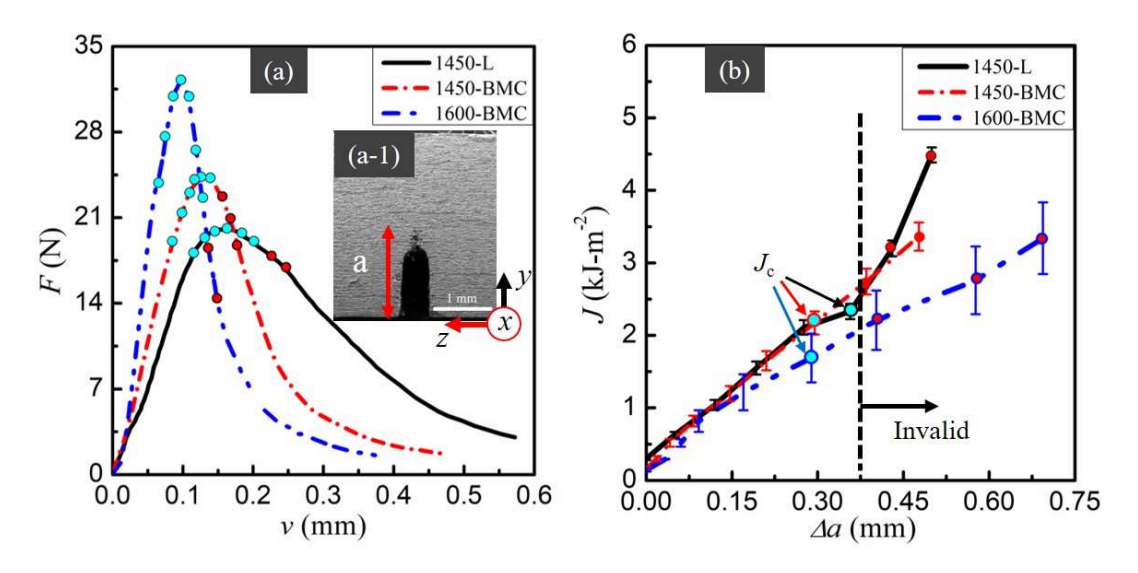


Fig. 5.4 (a) Typical F-v curves of lamellar and brick-mortar SENB composite samples. (a-1) SEM of representative SENB sample (b) J- Δa curve of 1450-L, 1450-BMC, and 1600-BMC composite samples, indicating validity of the data points following the ASTM standards[40].

5.3 Discussion

Both lamellar and brick-mortar composites show failure strains >1 % (Fig. 5.3 (a)), qualitatively mimicking the mechanical behaviour of natural nacre in bending [39]. The refinement in the thickness of lamellae and polymer phase improved both the strength and initiation fracture toughness as shown in Fig. 5.3 (b), and Fig. 5.5 (a). The flexure strength and $K_{\rm IC}$ of 1600-BMC is even higher than 1450-BMC. Moreover, $K_{\rm IC}$, a linear elastic parameter to characterize the crack, does not account the multiple toughening mechanisms present in such composites. In such cases, $J - \Delta a$ curve (Fig. 5.4 (b)) is better suited to characterize the crack behavior during crack initiation and its growth. The measured critical toughness (J_c) (shown in Fig. 5.5 (b)) for lamellar and brick-mortar composites has reverse trend *i.e.* refinement in the lamellae, and polymer thickness reduces the critical fracture

toughness with minimum value recorded for 1600-BMC. One of the primary reasons for the decrement in J_c for brick-mortar composites may be associated with the crack tortuosity (C_t) . The definition of crack tortuosity (C_t) and its measurement is discussed in the Section 4.3 of the Chapter 4. From Fig. 5.5 (c-d), it is evident that crack growth in the brick-mortar composites (1450-BMC as representative) is relatively straight in comparison to the lamellar composites. As a result, crack tortuosity (C_t) is relatively small for brick-mortar composites $(C_t = 1.4 \pm 0.05)$ in comparison to the lamellar composites $(C_t = 1.7 \pm 0.08)$. Moreover, the relatively thicker polymer phase in lamellar composites causes large ductile deformation ahead of the crack tip, and may contribute largely to the toughness, J_c [41].

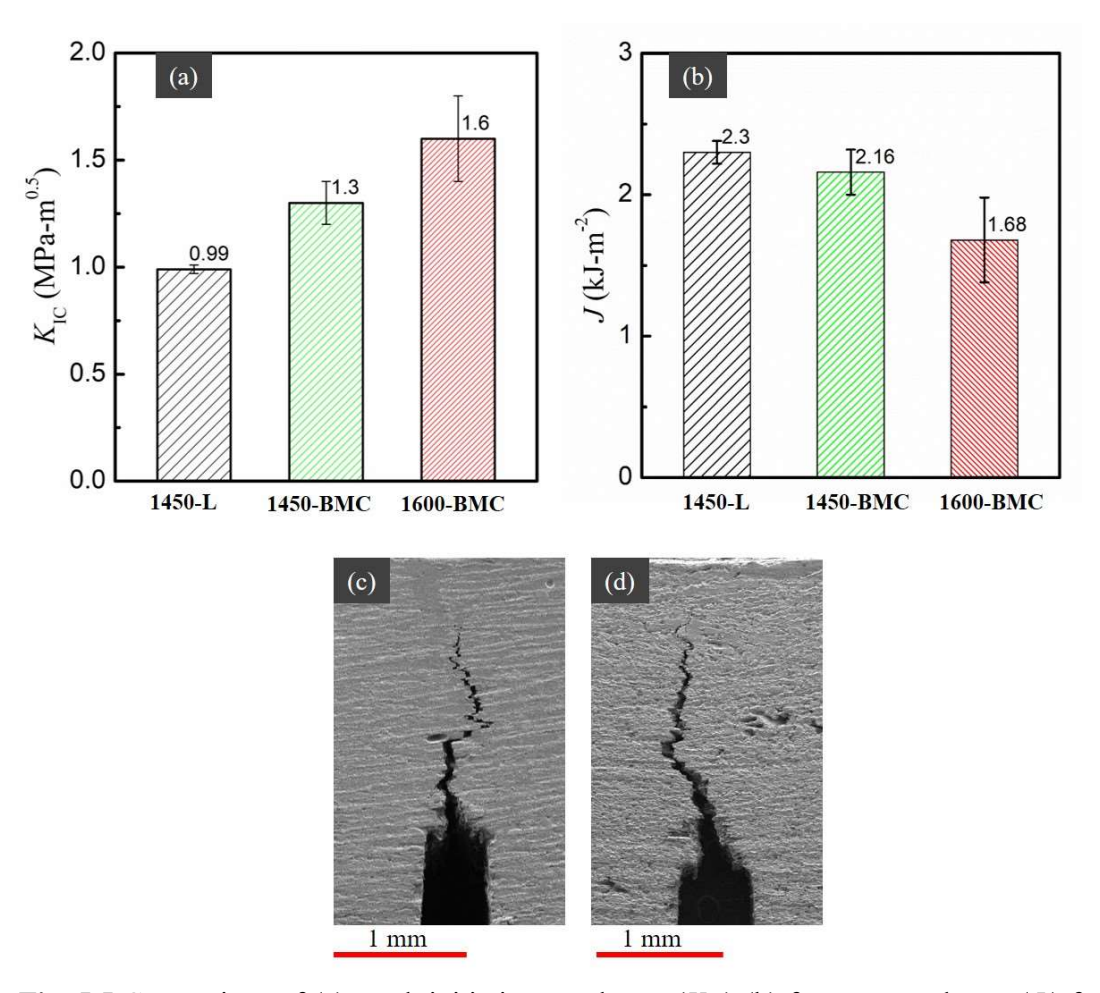


Fig. 5.5 Comparison of (a) crack initiation toughness ($K_{\rm IC}$) (b) fracture toughness ($J_{\rm c}$) for 1450-L, 1450-BMC, and 1600-BMC composites. SEM of Fractured SENB specimens showing crack path in (c) lamellar, and (d) brick-mortar composites.

For better insights and understanding of the experimental finding, continuum analysis is performed on the simplified 2D representative volume element (RVE) using shear lag model [42]. Based on the SEM micrograph shown in the Fig. 5.2 (a), the simplified 2D continuum unit cell of brick-mortar composite is shown in the Fig. 5.6 (a-b). In the model, t, and λ represent the thickness of the brick and polymer phase respectively. Several studies suggest that the effective strength and toughness of nacreous structures are linked to the unique stress transfer mechanism through tension –shear [20,25,37,43]. Among other parameters, the stress transfer mechanisms critically depend on the overlap length L_0 (see Fig. 5.6 (b)) [26,28]. Fig. 5.6 (c) schematically shows the overlap region in which stress, σ is applied at the bottom brick and the left end of the top brick has roller support. The left end of the bottom brick and right end of top brick are assumed to be traction free [37].

Applying force balance to the unit cell shown in Fig. 5.6 (c),

$$\tau_x = (t/2) \frac{d\sigma_1(x)}{dx} = -(t/2) \frac{d\sigma_2(x)}{dx}$$
 5.1

Where, τ_x represents the shear stress distribution in the polymer phase, and $\sigma_1(x)$, $\sigma_2(x)$ represent the axial stress in the bottom and top bricks respectively.

Assuming the deformation of bricks and matrix is small (elastic condition) such that $\tau_x = G\gamma(x)$, where, G is the shear modulus of the polymer material, and shear strain $\gamma(x)$ is defined by Eq. (5.2),

$$\gamma(x) = \frac{u_1(x) - u_2(x)}{\lambda}$$
 5.2

Here, $u_1(x)$ and $u_2(x)$ are the displacements in the bottom and top bricks respectively.

As the bricks are assumed to deform elastically, $\sigma_1(x) = E du_1/dx$, and $\sigma_2(x) = E du_2/dx$, then the derivative of the shear stress in the polymer results in Eq. (5.3).

$$\frac{\mathrm{d}\,\tau_x}{\mathrm{d}x} = \frac{G}{\lambda} \left(\frac{\mathrm{d}u_1}{\mathrm{d}x} - \frac{\mathrm{d}u_2}{\mathrm{d}x} \right) = \frac{G}{E\lambda} (\sigma_1(x) - \sigma_2(x))$$
5.3

Now, combining Eq. (5.1) and Eq. (5.3) results in governing differential Eq. (5.4 - 5.5).

$$\frac{\mathrm{d}^2 \sigma_1(x)}{\mathrm{d}x^2} = \frac{2G}{E\lambda t} (\sigma_1(x) - \sigma_2(x))$$
5.4

$$\frac{\mathrm{d}^2 \sigma_2(x)}{\mathrm{d}x^2} = \frac{2G}{E\lambda t} (\sigma_2(x) - \sigma_2(x))$$
 5.5

Solving Eq. (5.4) and Eq. (5.5) with the boundary conditions of the unit cell *i.e.* σ_1 (x = 0) = 0; σ_1 ($x = L_0$) = σ ; σ_2 (x = 0) = σ ; σ_2 ($x = L_0$) = 0 results in Eq. (5.6 – 5.7)

$$\sigma_1(x) = \frac{\sigma}{\sinh(\psi L_0/2)} \sinh(\psi x/2) \cosh(\psi (L_0 - x)/2)$$
5.6

$$\sigma_2(x) = \frac{\sigma}{\sinh(\psi L_0/2)} \cosh(\psi x/2) \sinh(\psi (L_0 - x)/2)$$
5.7

Where, $\psi = 2\sqrt{G/E\lambda t}$.

Now using the results of Eq. (5.6) or Eq. (5.7) into the Eq. (5.1), the variation in shear stress along the overlap length in the polymer is given by the Eq. (5.8).

$$\tau_{x} = \frac{\sigma t \psi}{4 \sinh(\psi L_{0}/2)} \cosh(\psi (x - \frac{L_{0}}{2}))$$
5.8

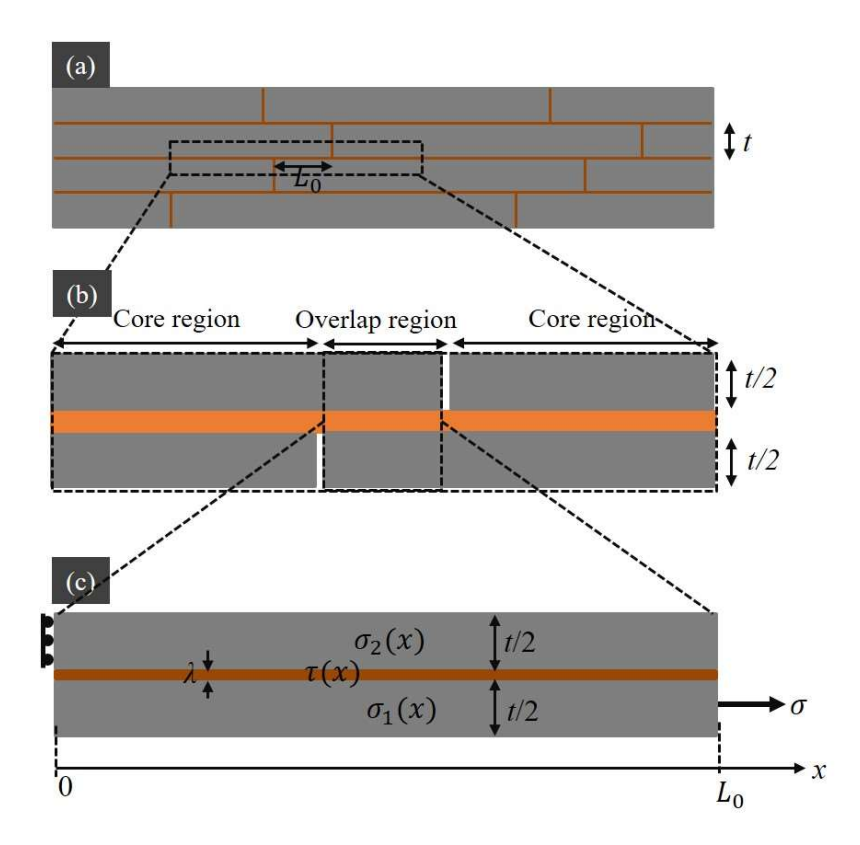


Fig. 5.6 (a) Schematic representing the structure of brick-mortar composites (b) 2D unit cell used for continuum analysis, and (c) two bricks connected with polymer phase with overlap length L_0 .

Based on the experimentally measured overlap length (L_0) in the B-M specimens, the distribution of normalised axial and shear stresses along the overlap length is shown in Fig. 5.7. Here, the overlap length in brick-mortar composites ranges from minimum of 20 ± 5 µm to maximum of 260 ± 94 µm with an average value of 130 ± 97 µm. The overlap length $L_0 = 2000$ µm corresponds to average overlap length in lamellar composites. The material parameters, modulus of brick E = 30 GPa [44], shear modulus of polymer G = 0.746 GPa [44] is fixed while using Eq. (5.6 - 5.8) at all overlap lengths. The geometrical parameters

i.e. average lamellae thickness, t and polymer thickness, λ are taken for the case of lamellar composite *i.e.* $t = 40 \mu m$ and $\lambda = 60 \mu m$ at all overlap length to maintain the consistency in comparative analysis.

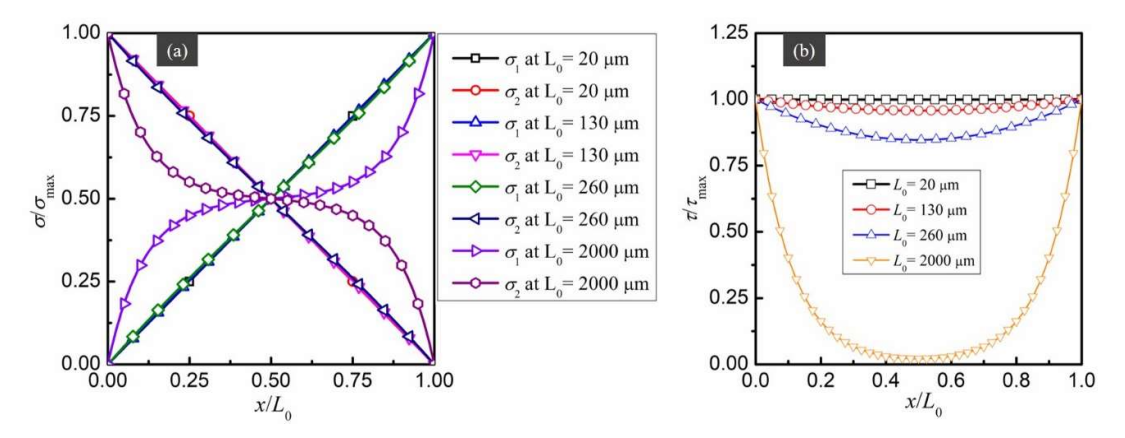


Fig. 5.7 Distribution of normalised (a) axial tensile stress (b) shear stress as a function of overlap length under linear elastic condition.

It is evident from Fig. 5.7 (a) that axial stresses vary linearly at smaller overlap lengths and becomes exponential with an average platue stress (σ / σ _{max} = 0.5) for most of the overlapped region at larger overlap length. Consequently, the composite with large overlap length (L_0 = 2000 µm) does not carry much shear load for most of the region except at the extremities of the overlap length. Hence, the shear load transfer mechanism will not be effective for larger overlap length and results to less efficient structure. Moreover, the distribution of shear stress gets more uniform at smaller overlap lengths.

For the given elastic properties of the brick and polymer, and known microstructural features, Wei et al. [37] proposed that the unit cell (in Fig. 5.6 (c)) maximizes its elastic strain energy density when overlap length becomes to L_0^* given by Eq. (5.9).

$$L_0^* = 2.318 \sqrt{\frac{E(t/2)\lambda}{G}}$$
 5.9

Eq. (5.9) suggests that for a given material combination of hard and soft phases, L_0^* directly proportional to the square root of the thickness of lamellae and polymer. Higher thickness of lamellae or polymer phase implies larger overlap length to maximize the strain energy density. Knowing the value of Young's modulus of the brick (E = 30 GPa), shear modulus of polymer (G = 0.746 GPa), and known microstructural features (t = 35 μ m for brickmortar, and 40 μ m for lamellar composites; $\lambda = 20$ μ m for brickmortar, and 60 μ m lamellar composites) from the experimental specimens, the computed value of L_0^* using Eq. (5.9)

for lamellar and brick-mortar composites is 509 μ m and 275 μ m respectively. However, the measured average overlap length in experimental samples is almost 4-times and 0.5-times of optimum computed overlap length (L_0^*) for lamellar and brick-mortar composites respectively. The average overlap length of brick-mortar composite samples is relatively close to the computed optimum overlap length based on elastic strain energy density, hence shows higher fracture initiation toughness than lamellar composites in Fig 5.5 (a).

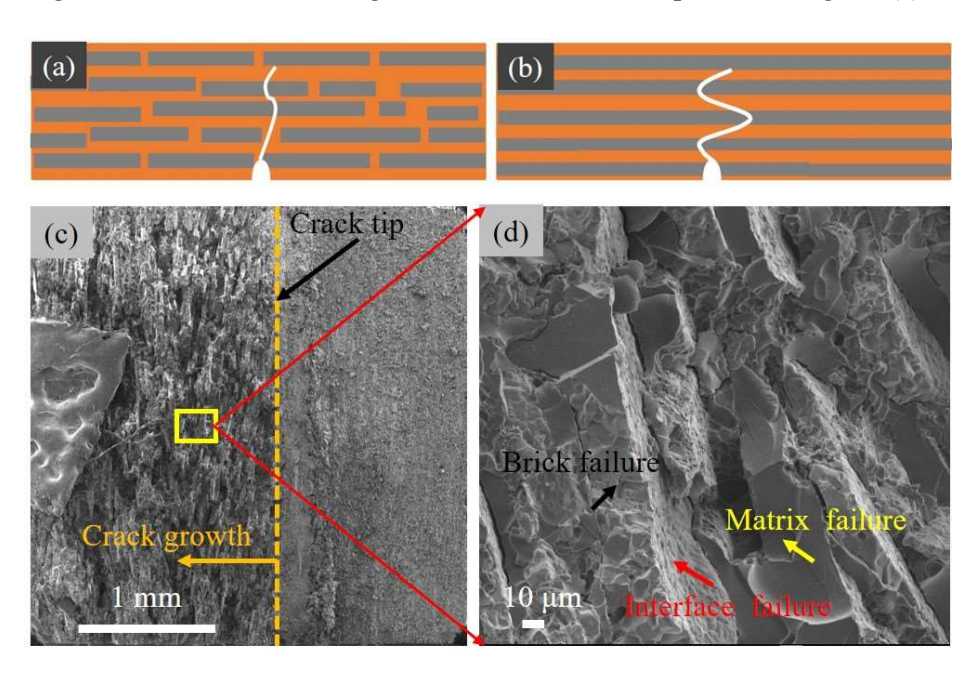


Fig. 5.8 Schematic of the crack path in (a) brick-mortar (b) lamellar composites (c - d) SEM micrograph showing fractured surface of brick-mortar composite.

The lower J_c for brick-mortar composites may be due to the lower crack tortuosity of the crack as shown in Fig. 5.5 (c-d). To explain this, two schematics representing brick-mortar and lamellar composites are shown in the Fig. 5.8 (a-b). Fig. 5.8 (a) represents the case when overlap length is small, where Fig. 5.8 (b) represents the lamellar composites with 100% overlap length. In case of brick-mortar composites, the distribution of bricks is more random, consequently the probability of the crack to encounter hard bricks and interfaces are comparatively less than in case of lamellar composites. In the case of lamellar composites when overlap length is 100%, the crack grows under the influence of maximum principal stress in hard phase, and maximum shear stress in the soft phase [45,46]. As a result, the crack path in brick-mortar composites is comparatively less tortuous than lamellar composites (see Fig. 5.5 (c - d)). Moreover, the crack grows in mixed mode condition (brick, polymer, and interface failure shown in Fig. 5.8 (c-d)) in both type of the

composites with relatively flat fractured surfaces (Fig. 5.8 (b)) in comparison to the fractured surface profile of the lamellar composites (see Fig. 4.9 (c - d) of the Chapter 4). As a result, J_c of brick-mortar composites is comparatively less in comparison to the lamellar composites.

Table 5.1 Comparison of mechanical properties of lamellar/brick-mortar composites with the data in other literatures.

Stru	acture/ceramic	Interfacial	Lamellae/brick	Flexural strength	Toughness
	content	chemistry	thickness (µm)	(MPa)	$(kJ-m^{-2})$
Lamellar alumina-		Grafted	8	180	~1.04
	A/72 vol%				
[8]	A//2 V01/0				
[0]		Grafted	6 - 8	10 - 80	-
Lamellar alumina-					
PMM	A/36 vol%				
[10]					
Lamellar alumina-		Non-grafted	20	90 ± 7	2.5
PMMA/36 vol%		~	•	440	
[14]		Grafted	20	112 ± 5	~ 5
[1.]		Grafted	5	210 12	0
Brick-mortar		Graned	3	210± 13	~ 8
alumina-PMMA/80					
vol% [14]					
- T-1	Lamellar	Non-grafted	40	25	2.3
This	~ 40 vol%				
study	Brick-mortar	Non-grafted	30	56	1.68
	~ 60 vol%				

Based on the preceding discussion, it is evident that the strength and toughness of the lamellar and brick-mortar composites largely depends on the thickness of individual phases, volume fraction of the hard phase, length of overlap length. While the strength and fracture initiation toughness are higher for brick-mortar composites, the critical fracture toughness is maximum for lamellar composites. Although, there is range of distribution of microstructural features and overlap length in experimentally prepared specimens, the shear-lag analysis provides necessary information about the optimum overlap length to maximize the elastic strain energy density. However, fabrication of optimized B-M structure with controlled distribution of bricks and polymer phase remains a challenge for

the future. Table 5.1 compares the mechanical properties of lamellar and brick-mortar alumina/epoxy composites in this study with the data available in the other literatures.

5.4 Conclusions

Mechanical measurements using flexure and fracture tests are performed to determine the strength and fracture toughness of the lamellar and brick-mortar alumina/epoxy composites. The experimental results show both high strength and high fracture initiation toughness of brick-mortar composites in comparison to the lamellar composites. Moreover, all types of specimens show rising J - Δa curve with maximum J_c recorded for lamellar composites. The higher J_c for lamellar composites is attributed to the higher crack tortuosity. Using shear lag analysis, it is shown that the fabricated lamellar/brick-mortar alumina/epoxy composites will have maximum resistance to fracture (corresponds to maximum elastic strain energy density) for an optimum overlap length. Among all types of fabricated composites, the strength of 1450-BMC is 80% higher than lamellar composites at the expense of 6% in J_c of lamellar composites. However, in the case of 1600-BMC, the strength is 124% higher than lamellar composites but at the expense of 27% in J_c of lamellar composites.

5.5 References

- [1] U.G.K. Wegst, H. Bai, E. Saiz, A.P. Tomsia, R.O. Ritchie, Bioinspired structural materials, Nat. Mater. 14 (2015) 23–36. https://doi.org/10.1038/nmat4089.
- [2] M.A. Meyers, P.Y. Chen, A.Y.M. Lin, Y. Seki, Biological materials: Structure and mechanical properties, Prog. Mater. Sci. 53 (2008) 1–206. https://doi.org/10.1016/j.pmatsci.2007.05.002.
- [3] A.R. Studart, Towards high-performance bioinspired composites, Adv. Mater. 24 (2012) 5024–5044. https://doi.org/10.1002/adma.201201471.
- [4] R.O. Ritchie, The conflicts between strength and toughness, Nat. Mater. 10 (2011) 817–822. https://doi.org/10.1038/nmat3115.
- [5] F. Barthelat, H.D. Espinosa, An experimental investigation of deformation and fracture of nacre-mother of pearl, Exp. Mech. 47 (2007) 311–324. https://doi.org/10.1007/s11340-007-9040-1.
- [6] H. Bai, F. Walsh, B. Gludovatz, B. Delattre, C. Huang, Y. Chen, A.P. Tomsia, R.O. Ritchie, Bioinspired Hydroxyapatite/Poly(methyl methacrylate) Composite with a Nacre-Mimetic Architecture by a Bidirectional Freezing Method, Adv. Mater. 28

- (2016) 50–56. https://doi.org/10.1002/ADMA.201504313.
- [7] S.M. Chen, H.L. Gao, X.H. Sun, Z.Y. Ma, T. Ma, J. Xia, Y.B. Zhu, R. Zhao, H. Bin Yao, H.A. Wu, S.H. Yu, Superior Biomimetic Nacreous Bulk Nanocomposites by a Multiscale Soft-Rigid Dual-Network Interfacial Design Strategy, Matter 1 (2019) 412–427. https://doi.org/10.1016/j.matt.2019.03.012.
- [8] H. Wan, N. Leung, S. Algharaibeh, T. Sui, Q. Liu, H.X. Peng, B. Su, Cost-effective fabrication of bio-inspired nacre-like composite materials with high strength and toughness, Compos. Part B Eng. 202 (2020). https://doi.org/10.1016/j.compositesb.2020.108414.
- [9] C. Huang, J. Peng, S. Wan, Y. Du, S. Dou, H.D. Wagner, A.P. Tomsia, L. Jiang, Q. Cheng, Ultra-Tough Inverse Artificial Nacre Based on Epoxy-Graphene by Freeze-Casting, Angew. Chemie Int. Ed. 58 (2019) 7636–7640. https://doi.org/10.1002/anie.201902410.
- [10] J. Liu, R. Bai, Z. Lei, C. Xu, Q. Ye, W. Martens, P.K. Yarlagadda, C. Yan, Experimental and numerical investigation of the toughening mechanisms in bioinspired composites prepared by freeze casting, Compos. Sci. Technol. 182 (2019) 107768. https://doi.org/10.1016/j.compscitech.2019.107768.
- [11] R.P. Wilkerson, B. Gludovatz, J. Watts, A.P. Tomsia, G.E. Hilmas, R.O. Ritchie, A study of size effects in bioinspired, "nacre-like", metal-compliant-phase (nickel-alumina) coextruded ceramics, Acta Mater. 148 (2018) 147–155. https://doi.org/10.1016/j.actamat.2018.01.046.
- [12] Y. Wang, Q. Liu, Z.F. Lan, B. Zhang, H.Q. Zhang, J.W. Liu, F. Ye, Strong and tough bioinspired nacre-like B4C/Al functionally graded materials with eliminated abrupt interfaces, Compos. Commun. 25 (2021) 100741. https://doi.org/10.1016/j.coco.2021.100741.
- [13] Z. Yin, F. Hannard, F. Barthelat, Impact-resistant nacre-like transparent materials, 1263 (2019) 1260–1263.
- [14] E. Munch, M.E. Launey, D.H. Alsem, E. Saiz, A.P. Tomsia, R.O. Ritchie, Tough, bio-inspired hybrid materials, Science (80-.). 322 (2008) 1516–1520. https://doi.org/10.1126/science.1164865.
- [15] I. Corni, T.J. Harvey, J.A. Wharton, K.R. Stokes, F.C. Walsh, R.J.K. Wood, A review of experimental techniques to produce a nacre-like structure, Bioinspiration and Biomimetics 7 (2012). https://doi.org/10.1088/1748-3182/7/3/031001.
- [16] H. Bai, Y. Chen, B. Delattre, A.P. Tomsia, R.O. Ritchie, Bioinspired large-scale

- aligned porous materials assembled with dual temperature gradients, Sci. Adv. 1 (2015) 1–9. https://doi.org/10.1126/sciadv.1500849.
- [17] S. Algharaibeh, A.J. Ireland, B. Su, Bi-directional freeze casting of porous alumina ceramics: A study of the effects of different processing parameters on microstructure, J. Eur. Ceram. Soc. 39 (2019) 514–521. https://doi.org/10.1016/j.jeurceramsoc.2018.09.030.
- [18] S.N. Tiwari, P.K. Agnihotri, Effect of freezing conditions on the microstructure and compressive response of alumina/epoxy nacre-type composites, Mater. Today Commun. 37 (2023) 107470. https://doi.org/10.1016/j.mtcomm.2023.107470.
- [19] G. Tan, J. Zhang, L. Zheng, D. Jiao, Z. Liu, Z. Zhang, R.O. Ritchie, Nature-Inspired Nacre-Like Composites Combining Human Tooth-Matching Elasticity and Hardness with Exceptional Damage Tolerance, Adv. Mater. 31 (2019) 1–9. https://doi.org/10.1002/adma.201904603.
- [20] H. Gao, B. Ji, I.L. Jäger, E. Arzt, P. Fratzl, Materials become insensitive to flaws at nanoscale: Lessons from nature, Proc. Natl. Acad. Sci. U. S. A. 100 (2003) 5597–5600. https://doi.org/10.1073/pnas.0631609100.
- [21] F. Barthelat, C.M. Li, C. Comi, H.D. Espinosa, Mechanical properties of nacre constituents and their impact on mechanical performance, J. Mater. Res. 21 (2006) 1977–1986. https://doi.org/10.1557/jmr.2006.0239.
- [22] F. Barthelat, R. Rabiei, Toughness amplification in natural composites, J. Mech. Phys. Solids 59 (2011) 829–840. https://doi.org/10.1016/j.jmps.2011.01.001.
- [23] F. Barthelat, D. Zhu, A novel biomimetic material duplicating the structure and mechanics of natural nacre, J. Mater. Res. 26 (2011) 1203–1215. https://doi.org/10.1557/jmr.2011.65.
- [24] Y. Yan, Z.L. Zhao, X.Q. Feng, H. Gao, Nacre's brick–mortar structure suppresses the adverse effect of microstructural randomness, J. Mech. Phys. Solids 159 (2022) 104769. https://doi.org/10.1016/j.jmps.2021.104769.
- [25] H. Yao, Z. Song, Z. Xu, H. Gao, Cracks fail to intensify stress in nacreous composites, Compos. Sci. Technol. 81 (2013) 24–29.
- [26] Y. Ni, Z. Song, H. Jiang, S.H. Yu, L. He, Optimization design of strong and tough nacreous nanocomposites through tuning characteristic lengths, J. Mech. Phys. Solids 81 (2015) 41–57. https://doi.org/10.1016/j.jmps.2015.04.013.
- [27] J.E. Rim, P. Zavattieri, A. Juster, H.D. Espinosa, Dimensional analysis and parametric studies for designing artificial nacre, J. Mech. Behav. Biomed. Mater. 4

- (2011) 190–211. https://doi.org/10.1016/j.jmbbm.2010.11.006.
- [28] F. Barthelat, Designing nacre-like materials for simultaneous stiffness, strength and toughness: Optimum materials, composition, microstructure and size, J. Mech. Phys. Solids 73 (2014) 22–37. https://doi.org/10.1016/j.jmps.2014.08.008.
- [29] J.D. Currey, Mechanical properties of mother of pearl in tension, Proc. R. Soc. London Biol. Sci. 196 (1977) 443–463. https://doi.org/10.1098/rspb.1977.0050.
- [30] S.P. Kotha, S. Kotha, N. Guzelsu, Shear-lag model to account for interaction effects between inclusions in composites reinforced with rectangular platelets, Compos. Sci. Technol. 60 (2000) 2147–2158. https://doi.org/10.1016/S0266-3538(00)00114-7.
- [31] S. Askarinejad, N. Rahbar, Mechanics of bioinspired lamellar structured ceramic/polymer composites: Experiments and models, Int. J. Plast. 107 (2018) 122–149. https://doi.org/10.1016/j.ijplas.2018.04.001.
- [32] M. Grossman, F. Bouville, K. Masania, A.R. Studart, Quantifying the role of mineral bridges on the fracture resistance of nacre-like composites, Proc. Natl. Acad. Sci. 115 (2018) 12698–12703.
- [33] F. Barthelat, M. Mirkhalaf, The quest for stiff, strong and tough hybrid materials:

 An exhaustive exploration, J. R. Soc. Interface 10 (2013).

 https://doi.org/10.1098/rsif.2013.0711.
- [34] H. Gao, Application of fracture mechanics concepts to hierarchical biomechanics of bone and bone-like materials, Int. J. Fract. 138 (2006) 101–137.
- [35] L.J. Bonderer, of Platelet Reinforced Polymer Films, Science (80-.). 205411 (2007) 1069–1073.
- [36] B. Chen, P.D. Wu, H. Gao, A characteristic length for stress transfer in the nanostructure of biological composites, Compos. Sci. Technol. 69 (2009) 1160– 1164. https://doi.org/10.1016/j.compscitech.2009.02.012.
- [37] X. Wei, M. Naraghi, H.D. Espinosa, Optimal length scales emerging from shear load transfer in natural materials: Application to carbon-based nanocomposite design, ACS Nano 6 (2012) 2333–2344. https://doi.org/10.1021/nn204506d.
- [38] S. Askarinejad, N. Rahbar, Toughening mechanisms in bioinspired multilayered materials, J. R. Soc. Interface 12 (2015). https://doi.org/10.1098/rsif.2014.0855.
- [39] M.E. Launey, E. Munch, D.H. Alsem, H.B. Barth, E. Saiz, A.P. Tomsia, R.O. Ritchie, Designing highly toughened hybrid composites through nature-inspired hierarchical complexity, Acta Mater. 57 (2009) 2919–2932.

- https://doi.org/10.1016/j.actamat.2009.03.003.
- [40] E1820–20b, Standard Test Method for Measurement of Fracture Toughness 1, Annu. B. ASTM Stand. i (2001) 1–56. www.astm.org,.
- [41] T. Magrini, A. Senol, R. Style, F. Bouville, A.R. Studart, Fracture of hierarchical multi-layered bioinspired composites, J. Mech. Phys. Solids 159 (2022).
- [42] H.L. Cox, The elasticity and strength of paper and other fibrous materials, Br. J. Appl. Phys. 3 (1952) 72–79. https://doi.org/10.1088/0508-3443/3/302.
- [43] M.R. Begley, N.R. Philips, B.G. Compton, D. V. Wilbrink, R.O. Ritchie, M. Utz, Micromechanical models to guide the development of synthetic "brick and mortar" composites, J. Mech. Phys. Solids 60 (2012) 1545–1560.
- [44] S.N. Tiwari, P.K. Agnihotri, Characterizing crack behaviour in nacre-like alumina/epoxy lamellar composites: Microstructure and crack tortuosity, Compos. Sci. Technol. 263 (2025) 111105. https://doi.org/10.1016/j.compscitech.2025.111105.
- [45] F. Libonati, A.E. Vellwock, F. Ielmini, D. Abliz, G. Ziegmann, L. Vergani, Bone-inspired enhanced fracture toughness of de novo fiber reinforced composites, Sci. Rep. 9 (2019) 1–12. https://doi.org/10.1038/s41598-019-39030-7.
- [46] A.E. Vellwock, L. Vergani, F. Libonati, A multiscale XFEM approach to investigate the fracture behavior of bio-inspired composite materials, Compos. Part B Eng. 141 (2018) 258–264. https://doi.org/10.1016/j.compositesb.2017.12.062.

6.1 Summary of the work

This thesis presents a detailed study on the fabrication and characterization of nacre-like lamellar/brick-mortar composites. Inspired by nacreous structure and its outstanding mechanical performance, this study employed bi-directional freeze casting as a key fabrication method to achieve lamellar and brick-mortar structure in alumina/epoxy composites. The developed artificial nacre-like lamellar/brick-mortar composites are characterized using multitude of experimental techniques, and numerical/analytical methods. The important findings of this thesis are described below.

- In the bi-directional freeze casting method, it is observed that both the lamellae thickness and interlamellar spacing increases with the increase in PDMS wedge angle (θ) . The increase in PDMS wedge angles induces more horizontal temperature gradients across the suspension but decreases the freezing velocity across the suspension. As a result, the evolved microstructure features are greatly affected. The additional horizontal temperature gradient helps to align the ice-crystals in the larger domain, the decreased freezing velocity increases the thickness of growing ice crystals. Consequently, both the lamellae thickness and interlamellar spacing increase with the increase in PDMS wedge angle. The highly aligned lamellar structures are obtained for PDMS wedge angle $\theta =$ 10°. The mechanical behavior of the lamellar alumina/epoxy composites accessed through compressive loading reveals their anisotropy in mechanical response as well as in deformation characteristics. The comparison of lamellae thickness and peak strength with respect to wedge angles reveals that for the given slurry composition of 20 vol% alumina concentration, 10° is an optimum wedge angle to achieve higher strength and energy absorbing capacity in bi-directionally frozen nacre-like alumina/epoxy composites.
- In view of developing tough material, it become essential to characterize the crack behavior in the developed anisotropic lamellar composites. This is accomplished using experimental testing, analytical calculation, and numerical simulation. The anisotropic behavior of the composites in fracture experiments is accounted by varying the lamellae thickness of ceramic phase and crack orientation angle with respect to the lamellae. It is found that the composites show rising J_R curves with maximum fracture toughness (J_{max})

for the composites with larger lamellae thickness and crack orientation angle. The presence of multiple toughening mechanisms such as crack deflection, shearing of epoxy, lamellae pull-out, and crack tortuosity supports the experimentally measured rising J_R curves. Moreover, the tortuous crack path indicates that crack grows in mixed mode condition. The analytical results of mode mixity (K_{II}^k/K_I^k) at crack initiation reveals that K_{II}^k/K_I^k increases with the increase in the thickness of alumina layer or crack orientation angle. To experimentally characterize the anisotropy in crack propagation, a non-dimensional parameter $\delta^* = \max\{|\delta^+|, |\delta^-|\}/\min\{|\delta^+|, |\delta^-|\}$ is proposed using crack mouth opening displacement (CMOD) measurements. The CMOD measurements based non-dimensional parameter δ^* shows similar variation and accurately captures the anisotropic crack propagation in lamellar composites. Moreover, the XFEM based simulation results closely capture the experimental F - v responses, and crack paths in the lamellar composites.

• The highly aligned lamellar alumina scaffolds obtained in bi-directional freeze casting $(\theta = 10^{\circ})$ are used as preform for the fabrication of alumina/epoxy composites with brick-mortar structure. The experimental results of flexure and fracture testing show that the strength and fracture initiation toughness of brick-mortar composites are higher than the lamellar alumina/epoxy composites. Moreover, both lamellar and brick-mortar composites show rising J_R curves with maximum J_c recorded for lamellar composites. The shear lag analysis using experimentally measured overlapped lengths reveals that lamellar and brick-mortar alumina/epoxy composites will have maximum resistance to fracture (corresponds to maximum elastic strain energy density) for an optimum overlap length.

In summary we can conclude that bi-directional freeze casting method is an efficient route to fabricate nacre-like composites with tailored microstructure and improved mechanical properties. The insights gained from this study offer significant potential for real world applications. The anisotropy observed in lamellar/brick-mortar composites opens avenues for graded materials with tailored properties in advanced engineering applications. The lamellar and brick-mortar composites can be utilized as protective structural components, biomedical implants, aerospace components, and impact resistant panels.

6.2 Future scopes

The developed ceramic scaffolds and composites materials in this work are similar to that of natural biomaterials i.e. nacre, and hence can provide advantage in the field of aerospace, biomedical implants, and defence engineering. However, following points may be considered in future studies:

- Effect of lamellar scaffold crushing pressure on the strength and fracture toughness of brick-mortar alumina/epoxy composites.
- To improve the structural performance by engineering the interface of ceramic and polymer in nacre-like brick-mortar composites.
- To develop a suitable numerical model to understand the crack behavior in brickmortar composites considering the statistical variation in the microstructural features.
- Scaling up of the process: It is basically major limitation of the freeze casting process due to difficulty in the control of temperature fields and gradients in the larger domain.